Probing Proton Drip-Line Nuclei in the A $\sim$ 110 and A $\sim$ 130 Mass Regions using Stable- and Radioactive-Ion Beams

Thesis submitted in accordance with the requirements of
the University of Liverpool for the degree of Doctor in Philosophy
by

Marina-Kalliopi Petri

Department of Physics

March 2008

Abstract

This thesis summarises the work carried out from two heavy-ion fusion-evaporation experiments that had the goal to perform γ-ray spectroscopy in very proton-rich nuclei in the A $\sim$ 130 and A $\sim$ 110 mass regions of the nuclear chart using radioactive- and stable-ion beams, respectively.

One of the first ever fusion-evaporation experiments using radioactive-ion beams was performed at GANIL in order to study proton-rich nuclei of the light rare-earth region. A radioactive ^{76}Kr beam, delivered by the SPIRAL facility, was used to bombard a thin ^{58}Ni target. The low production cross section of the exotic species of interest, in combination with the low intensity of the beam and its induced background, demanded the use of a highly efficient experimental setup. This consisted of the EXOGAM γ-ray spectrometer coupled for the first time with both the DIAMANT charged-particle array and the VAMOS spectrometer. High-spin states in the ^{130}Nd (22^+), ^{129}Pr ($27/2^-$), ^{127}Pr ($35/2^-$), ^{128}Nd (16^+), ^{131}Pm ($27/2^-$) and ^{126}Ce (6^+) nuclides have been observed. The experimental challenges are discussed and the experimental achievements of the in-beam spectroscopy of proton drip-line nuclei are presented.

A level scheme has been constructed for the proton-unbound, $T_z = 3/2$ nuclide $^{109}_{53}I_{56}$ following a recoil-decay-tagging experiment using the ^{58}Ni(^{54}Fe, p2nγ) reaction at a beam energy of 195 MeV. The experiment was performed using the highly efficient JUROGAM γ-ray spectrometer in conjunction with the RITU gas-filled recoil separator and the GREAT focal-plane spectrometer. Cranking calculations are used to interpret band structures built on $\pi g_{7/2}$ and $\pi h_{11/2}$ states in a weakly deformed, triaxial nucleus. In addition, a third band is proposed to be built on a $\pi g_{7/2}$ orbital coupled to an octupole-vibrational phonon of the ^{108}Te core.

To Stefanos,

for all his support and inspiration.

Στη Μαρία,

για τη γενναία μάχη που δίνει.

Contents

List of Figures

List of Tables

Acknowledgements

As this seemingly never-ending task comes to its most anticipated conclusion, I want to express my gratitude to the people that contributed to the completion of this thesis in various ways.

I would like to thank my supervisors Prof. Paul Nolan and Dr. Andy Boston for allowing me to undertake this research at the University of Liverpool. I am most grateful to both of them for encouraging me to attend conferences and schools and funding me to participate in various experiments. A special thanks goes to Prof. Paul Nolan for all his comments, stimulating discussions and suggestions on my work during our meetings.

I am deeply indebted to Dr. Eddie Paul, my every-day supervisor, for all his help, guidance, enthusiasm and enlightening discussions throughout all these years. I wish and hope that our collaboration will not end with the submission of this manuscript. I want to thank him for proof reading this thesis and apologise for all the language corrections he had to go through. I greatly appreciate all his efforts to introduce me to the culture of beer with, however, not so promising results. All the trips we have been together were great fun, especially the road trips.

I am grateful to the Engineering and Physical Sciences Research Council (EPSRC) for the receipt of a studentship and to all the staff of the Department of Physics for their help and support. I would like to thank Prof. Rolf-Dietmar Herzberg and Dr. Eddie Paul for their interesting and useful lectures on various topics of Nuclear Physics. All the postgraduate students and postdocs, past and present, deserve a big mention for not allowing any homesickness to find its way into my mind. A special thanks goes to Dr. John Cresswell, Mark Norman and Janet Sampson for the computer and technical support and Norma for always making my mood.

I would like to thank Dr. Christos Touramanis for his great help in work and non-work related matters and especially for keeping me sane during the last months of the PhD. All the Greek-politics discussions were always a very pleasant break from many miserable afternoons.

Finally, I want to thank my family for always being by my side and Stefanos for being in my life!

Chapter 1

Introduction

The atomic nucleus is a unique mesoscopic quantal system, where the interplay between the strong, the electromagnetic and the weak interaction defines its binding energy. It is described by nuclear models, as the underlying strong nuclear force is not well understood. Experimental nuclear structure studies probe the properties of the atomic nucleus and thus constitute a driving force as well as a testing ground for these models.

Cold nuclei at or near the valley of stability have been extensively studied both experimentally and theoretically and the existing nuclear models can successfully describe most of their properties. However, these models fail to explain or reproduce results from nuclei under extreme conditions of isospin, angular momentum, mass/charge and temperature. The experimental interest in studying nuclei under extreme conditions has driven modern spectroscopic studies towards exotic nuclei. Proton drip-line nuclei in particular provide a fertile testing ground for nuclear models as to extreme ratios of proton-neutron numbers and high values of angular momentum transferred to the system via the reaction mechanism, i.e. fusion-evaporation reactions. This thesis concentrates on the study of two different very proton-rich mass regions, the A $\sim$ 130 rare-earth region around the drip-line nucleus ^{130}Sm and the A $\sim$ 110 mass region and more specifically the ^{110}Xe and ^{109}I nuclides.

The A $\sim$ 130 rare-earth region is of great interest since very deformed prolate ground states have been predicted theoretically [1] with $\beta_2 \sim 0.4$; in Fig. 1.1 the chart of the nuclei is illustrated with the corresponding ground-state quadrupole deformations of the nuclides calculated by Möller and Nix [2]. This ground-state deformation of nuclei around ^{130}Sm reaches values as high as those corresponding to the superdeformed bands of the nearby cerium and neodymium isotopes at high spin. Studying thus these nuclei will allow some very interesting comparisons of their configurations to be made, i.e. are the same orbitals responsible for the large quadrupole deformation? This theoretically predicted large ground-state deformation can also be inferred from experimental deformation trends [3, 4]. These trends can be observed in Fig. 1.2, where the systematics of the $2^+ \rightarrow 0^+$ and $15/2^- \rightarrow 11/2^-$ transitions of the even- and odd-Z

nuclides are illustrated, respectively. The energy of the $2^+ \rightarrow 0^+$ transition of the yrast[1] rotational band of the even-even nuclei is inversely proportional to the nuclear moment of inertia and hence to the quadrupole deformation β_2, i.e. the lower the 2^+ state, the larger the quadrupole deformation. In the odd-Z nuclei the $15/2^- \rightarrow 11/2^-$ transition energy is used for mapping deformation trends, as the yrast rotational bands are built on a low-Ω $h_{11/2}$ particle weakly coupled to the core and this transition is analogous to the $2^+ \rightarrow 0^+$ energies of the even-even nuclei. In Fig. 1.2 it is evident that as the neutron mid-shell of N = 64 is approached, the ground-state deformation of these nuclei increases.

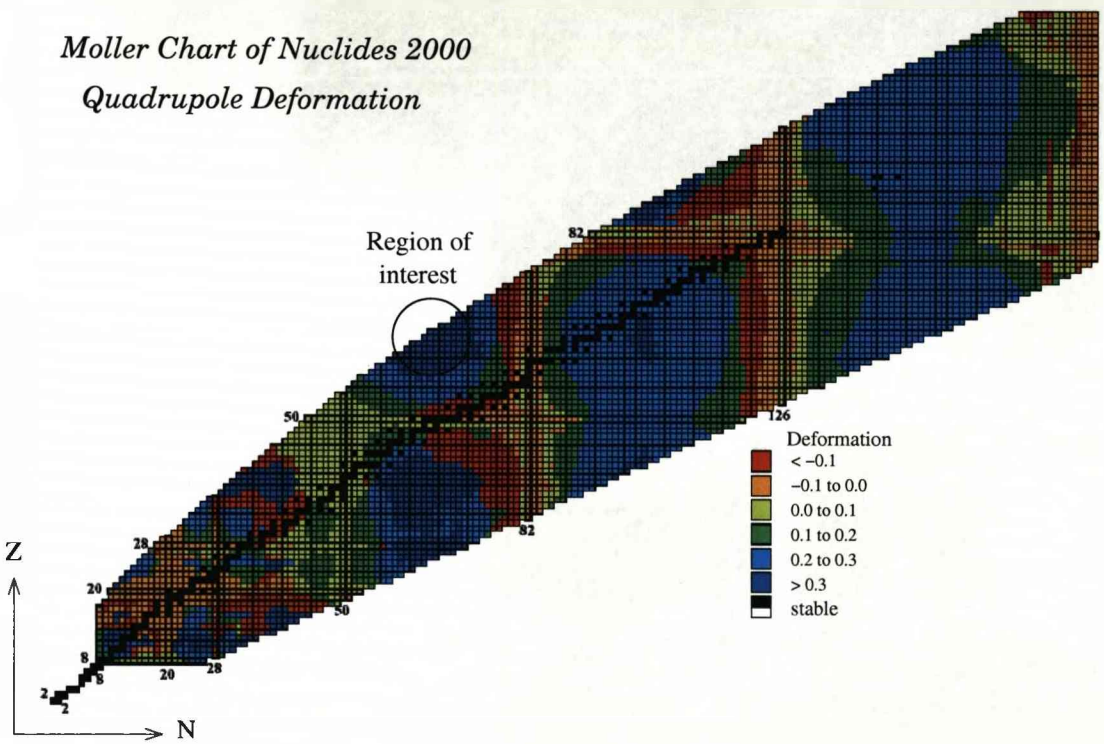

Figure 1.1: Möller and Nix deformation systematics. The highly deformed mass region of $\beta_2 > 0.3$ midway between the N = Z = 50 and N = Z = 82 double shell closures is evident.

The present experiment had the goal to probe the peak of this deformation by studying the yrast rotational bands of the lightest proton-bound samarium isotope ^{130}Sm, the first excited state of which has been documented in Ref. [5], and the completely unknown ^{131}Sm and ^{130}Pm isotopes. A radioactive-ion beam delivered by the SPIRAL facility at GANIL, France, was used, inducing many experimental challenges. In order to identify and perform γ-ray spectroscopy in the nuclei of interest a highly efficient experimental setup was used, consisting of the EXOGAM γ-ray spectrometer, the DIAMANT charged particle array and the VAMOS spectrometer. The advances of

[1] "Yrast" is the Swedish word for "dizziest". The yrast state refers to the lowest energy state for a certain spin.

the in-beam spectroscopy of proton drip-line nuclei are discussed and presented in this thesis.

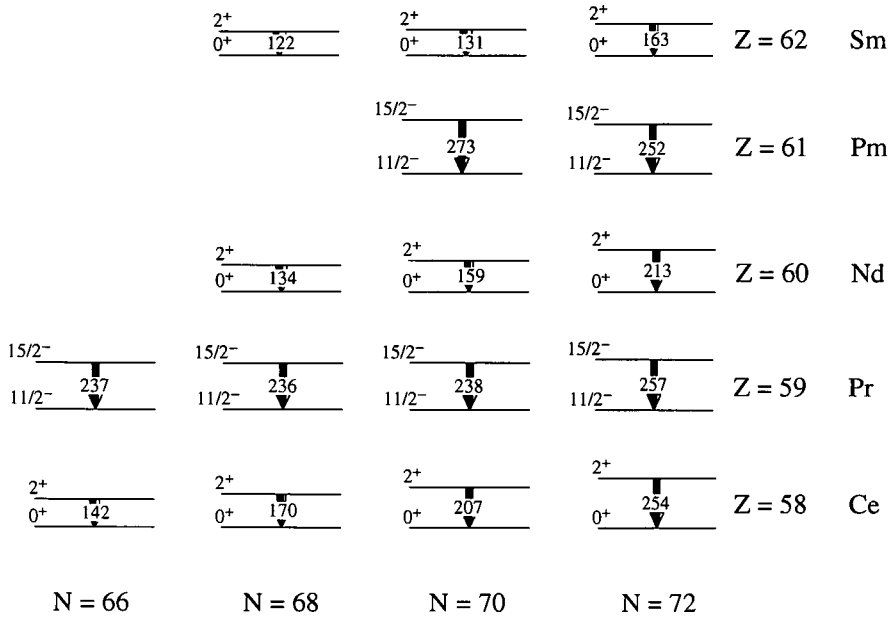

Figure 1.2: Systematics of the $2^+ \rightarrow 0^+$ and $15/2^- \rightarrow 11/2^-$ transitions of the even- and odd-Z nuclides, respectively, in the A $\sim$ 130 mass region. The data are taken from Ref. [6].

The A $\sim$ 110 region provides valuable information on single-particle energies and residual interactions with respect to the doubly magic ^{100}Sn "core". The ^{100}Sn nuclide is the heaviest N = Z nucleus believed to be bound. Its spectroscopic study would provide a stringent test of the nuclear Shell Model. Unfortunately, the level structure of this nucleus is not accessible with the technology available today. Nevertheless, important information can be obtained by studying excited states of nuclei in its vicinity. Moreover, in the A $\sim$ 110 region the emergence of collectivity, in the form of vibrational or rotational excitations, in the Te and Xe isotopes is of special interest. The present experiment performed a recoil-decay-tagging investigation of the level structure of the ^{110}Xe [7] nuclide via the ^{58}Ni(^{54}Fe, 2n) reaction. Another exit channel (p2n) of this reaction leads to the proton emitter ^{109}I. In this thesis results on the study of the latter nucleus are presented.

The proton-unbound ^{109}I nuclide, lying beyond the proton drip line, can yield γ-ray spectroscopic information, as its known ground-state proton decay can be used as a tag. Moreover, the level structure of ^{109}I could shed light to the question as to from which orbital the proton is emitted, i.e. which orbital forms the ground state of ^{109}I. The ^{109}I nuclide has been studied before twice, by E. S. Paul *et al.* [8] and by C.-H. Yu *et*

al. [9], yielding completely different level schemes, illustrated in Fig. 1.3. The present experiment exploited the powerful recoil-decay-tagging technique as implemented in the Accelerator Laboratory of the University of Jyväskylä (JYFL), Finland, where the JUROGAM γ-ray spectrometer is coupled with the RITU gas-filled recoil separator and the GREAT focal plane. This work, with much greater statistics, has allowed a resolution of this conflict and a new level scheme has been built for the proton-unbound ^{109}I nuclide.

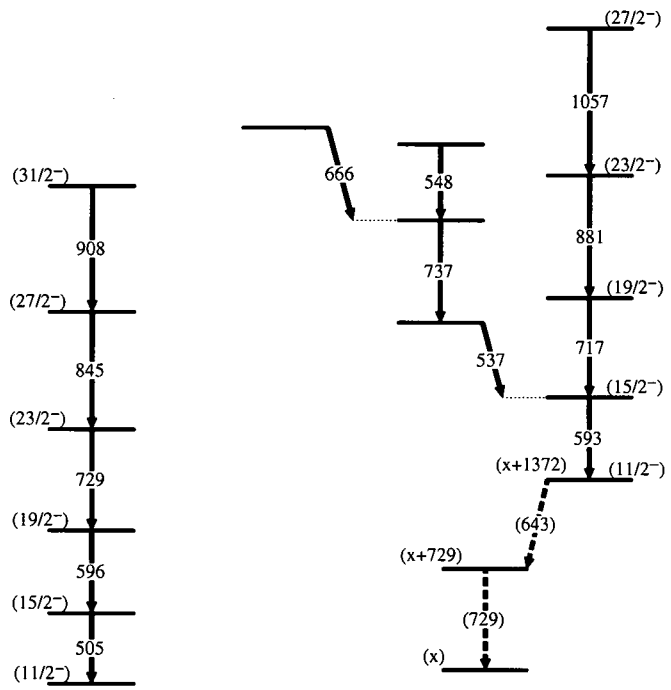

Figure 1.3: The previously proposed level schemes for the proton-unbound ^{109}I nuclide.

In order to accommodate both aforementioned experiments, this thesis has been divided into four main chapters (Chapters 2, 3, 4 and 5), excluding the current and the last one. In Chapter 2 an introduction to the nuclear models appropriate for this work is presented. In Chapter 3 the experimental techniques and apparatus used in both experiments are described. The following two chapters document the experimental details, the results and the conclusions of the two experiments separately; in Chapter 4 the radioactive-ion beam experiment is discussed with its implications on the in-beam spectroscopy of proton drip-line nuclei using EXOGAM and radioactive-ion beams, while in Chapter 5 the recoil-decay-tagging experiment and its results are discussed. Finally, in Chapter 6 general conclusions from both experiments are documented and suggestions for future work are proposed.

Chapter 2

Theory

The nuclear many-body problem still remains an open question, while the nucleus presents ever more interesting features. The nuclear models that have been developed so far are only partly successful, since they are addressed to a specific mass region, or to specific properties of the nucleus etc.

The Liquid Drop Model and the Shell Model are the first nuclear models that were used in order to interpret various properties of atomic nuclei. Each of these models was successful in explaining different aspects of the nucleus, being thus complementary to each other in the interpretation, but at the same time completely different in their underlying structure. The Liquid Drop Model described bulk properties of the nucleus, explaining mostly collective modes of excitation, in contrast with the Shell Model that gave a reasonable explanation to the nuclear shell structure as independent movement of particles in an average field.

One of the most intriguing phenomena in nuclear physics is the interplay between single-particle and collective degrees of freedom; single-particle motion represents an out-of-phase motion and gives rise to shell effects, single-nucleon states etc., while collective motion represents an in-phase motion of the nucleons, giving rise to rotations, vibrations, nuclear deformation etc. The challenge nowadays is how to combine and explain these two completely different aspects of nuclear behaviour.

In this chapter a brief description of the nuclear models that are used for this work is given and various relevant phenomena are mentioned, such as nuclear deformation and nuclear rotation.

2.1 Liquid Drop Model

The Liquid Drop Model (LDM), first developed by Bohr and Wheeler in 1939 [10] to treat the fission process, comprises a phenomenological approach to the atomic nucleus, considering it as a liquid drop. This idea originated from observations of low compressibility of the nucleus, its well-defined surface and the saturation properties of the nuclear interaction [11], resulting in a nearly constant nucleonic density in the

interior and a surface radius approximately equal to $1.2A^{1/3}$ fm. Nowadays, it is well proven that the nucleus "looks" nothing like a liquid drop. But since this model provides a simple way of explaining collective phenomena, as well as its successful interpretation of bulk properties of the nucleus, it is worth giving a brief overview.

The binding energy (BE) within this model is given as a function of N and Z according to the equation

$$BE(N,Z) = \alpha_{vol}A - \alpha_{sur}A^{2/3} - \alpha_{Coul}\frac{Z^2}{A^{1/3}} - \alpha_{sym}\frac{(N-Z)^2}{A}. \quad (2.1)$$

The terms of Eq. 2.1 are related to the volume of the drop, the surface corrections to the attractive interaction, the Coulomb repulsion and the symmetry energy, respectively. In Fig. 2.1 a comparison of the experimental binding energies and the theoretically calculated ones from the LDM are plotted against proton and neutron numbers. Although there is a good agreement between the experimental and theoretical values of the binding energy, it is evident that the nuclei present shell effects that cannot be explained within the LDM.

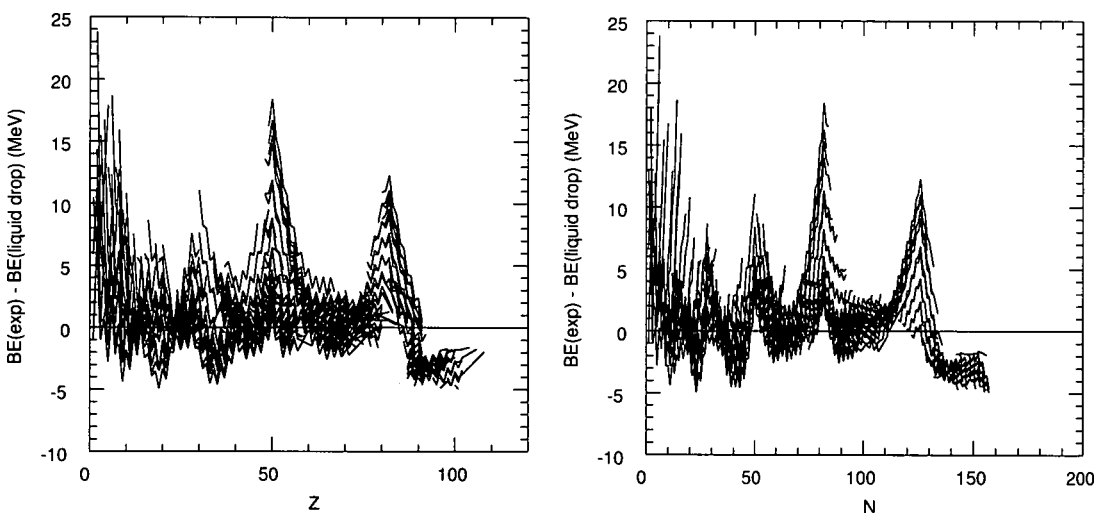

Figure 2.1: Experimental and liquid-drop binding energy difference as a function of proton Z and neutron N numbers [12]. The pronounced peaks correspond to the more bound "magic" nuclei at Z = 28, 50, 82 and N = 28, 50, 82, 126. The small oscillations are due to pairing effects.

2.2 Shell Model

The Shell Model or Independent Particle Model is based on the idea that the nucleons in a nucleus are considered to be independent particles moving in an average "mean-field" potential. The suggestion of almost unperturbed single-particle orbits is based on the fact that collisions of nucleons (fermions) within a nucleus are inhibited due to

Pauli blocking. The Shell Model has been very successful in describing many nuclear properties and mostly for reproducing the magic numbers 2, 8, 20, 28, 50, 82 and 126.

Within the nuclear shell model the many-body Schrödinger equation has the simple form

$$H\Psi = \left\{ \sum_{i=1}^{A} \left[-\frac{\hbar^2}{2m}\nabla^2 + V(i) \right] + \sum_{ij} U(ij) \right\} \Psi = E\Psi, \tag{2.2}$$

where U is the two-body residual interaction. The question is about the shape of the average nuclear potential V that will be used. There are many potentials that have been developed in order to describe as successful as possible nuclear properties. The most well-known are the infinite square-well potential

$$V(r) = \begin{cases} -V_0, & r \leq R_0 \\ +\infty, & r > R_0 \end{cases}, \tag{2.3}$$

the harmonic oscillator

$$V(r) = -V_0 \left[1 - \left(\frac{r}{R_0} \right)^2 \right] = \frac{m}{2}\omega^2 \left(r^2 - R_0^2 \right), \tag{2.4}$$

the Woods-Saxon potential

$$V(r) = \frac{-V_0}{1 + \exp\left[\frac{r - R_0}{\alpha} \right]}, \tag{2.5}$$

and the Yukawa potential

$$V(r) = -V_0 \frac{\exp\left(\frac{-r}{\alpha} \right)}{r}. \tag{2.6}$$

In these potentials V_0 represents the well depth, R_0 the nuclear radius, α the surface diffuseness and ω the oscillation frequency.

The Woods-Saxon potential is considered to be the most "realistic" potential, while the square-well and the harmonic oscillator are not physical potentials. However, the latter two can be solved analytically and are used for qualitative considerations and calculations, while the Woods-Saxon potential can only be solved numerically. In the harmonic oscillator potential an ℓ^2 term can be added in order to flatten its bottom and produce a more "Woods-Saxon like" potential, leading to the modified harmonic oscillator (MHO). All the above mentioned potentials "provoke" spherical symmetry.

2.2.1 Spin-Orbit Coupling

The spin-orbit term was introduced in the Shell Model by M. G. Mayer [13] and O. Haxel *et al.* [14] in 1949, and it was only then that the experimental magic numbers could be reproduced, as illustrated in Fig. 2.2. The spin-orbit term takes into account whether

the orbital angular momentum ℓ and the intrinsic spin s of the particle are parallel or antiparallel. The consequence of such an assumption is the splitting of levels energywise according to the $j = \ell + s$ value of $j = \ell + \frac{1}{2}$ and $j = \ell - \frac{1}{2}$ to lower and higher energies, respectively.

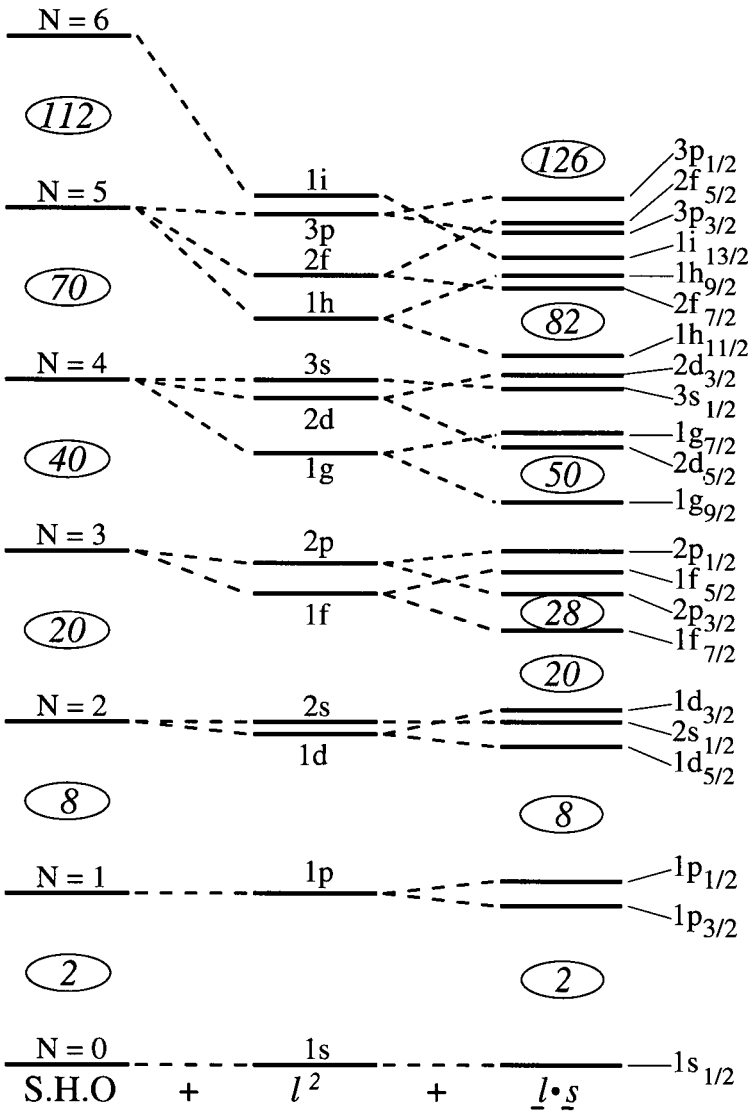

Figure 2.2: Evolution of the nuclear level ordering with respect to the nuclear potential, starting from the spherical harmonic oscillator (S.H.O) and moving towards the modified harmonic oscillator (S.H.O + ℓ^2) and the addition of the spin-orbit coupling term (S.H.O + ℓ^2 + $\underline{\ell} \cdot \underline{s}$).

2.3 Nuclear Deformation

The concept of nuclear deformation was first introduced when a great number of experimental properties could not be explained assuming a spherical single-particle potential. A deformed nucleus, which is associated with a deformed mean-field potential, can provide an explanation for the existence of rotational bands, large quadrupole moments and transition probabilities deduced in various nuclei, fission isomers etc.

2.3.1 Nuclear Shapes

Describing the nucleus as a "drop" of nuclear matter, one possible shape parametrisation involves the expression of the nuclear radius as a sum over spherical harmonics,

$$R(\theta,\phi) = C(\alpha_{\lambda\mu})R_o\left[1+\sum_{\lambda=0}^{\infty}\sum_{\mu=-\lambda}^{\lambda}\alpha_{\lambda\mu}Y_{\lambda\mu}(\theta,\phi)\right]. \tag{2.7}$$

In Eq. 2.7 R_o is the radius of a sphere, $\alpha_{\lambda\mu}$ are coefficients that represent distortions from the equilibrium spherical shape and $C(\alpha_{\lambda\mu})$ is a factor that compensates for the incompressibility of nuclear matter, i.e. volume conservation under distortions. The first two terms of the multipole expansion of Eq. 2.7 are ignored, since they do not contribute to any shape oscillations; $\lambda = 0$ represents compression or dilatation and $\lambda = 1$ involves the displacement of the "drop" as a whole. Eq. 2.7 can therefore be rewritten as

$$R(\theta,\phi) = C(\alpha_{\lambda\mu})R_o\left[1+\sum_{\lambda=2}^{\infty}\sum_{\mu=-\lambda}^{\lambda}\alpha_{\lambda\mu}Y_{\lambda\mu}(\theta,\phi)\right]. \tag{2.8}$$

The term with $\lambda = 2$ gives rise to quadrupole deformation, the $\lambda = 3$ term describes octupole shapes, the $\lambda = 4$ hexadecapole shapes etc., as illustrated in Fig. 2.3. Assuming rotational symmetry around the deformation axis, chosen as the z-axis, Eq. 2.8 can be simplified, since the terms with $\mu \neq 0$ vanish, as follows

$$R(\theta,\phi) = C(\alpha_{\lambda 0})R_o\left[1+\sum_{\lambda}\alpha_{\lambda 0}Y_{\lambda 0}(\theta,\phi)\right] = CR_o\left[1+\sum_{\lambda}\beta_{\lambda}Y_{\lambda 0}(\theta,\phi)\right]. \tag{2.9}$$

The spherical harmonics for $\mu = 0$ are proportional to the Legendre Polynomials [15] and can be written as

$$Y_{\lambda 0}(\theta,\phi) = \sqrt{\frac{2\lambda+1}{4\pi}}P_{\lambda}(\cos\theta). \tag{2.10}$$

The shape of an axially symmetric deformed nucleus is then described by the simplified equation

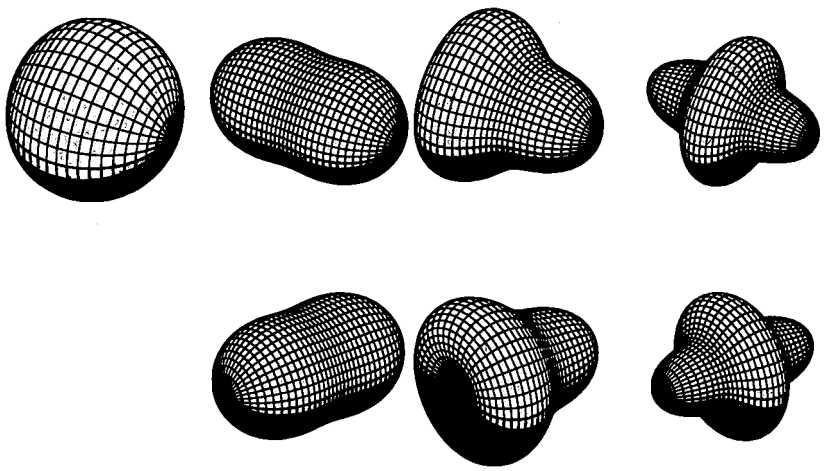

Figure 2.3: Nuclear shapes with no deformation, with quadrupole ($\lambda = 2$) deformation, octupole ($\lambda = 3$) and hexadecapole ($\lambda = 4$) deformation in each column, respectively.

$$R(\theta) = CR_o \left[1 + \sqrt{\frac{2\lambda + 1}{4\pi}} \sum_{\lambda} \beta_\lambda P_\lambda(\cos\theta) \right]. \tag{2.11}$$

2.3.2 Quadrupole Deformation

In the case of quadrupole deformation ($\lambda = 2$, ellipsoidal shape), the radius R is described by five coefficients $\alpha_{\lambda\mu}$ (α_{20}, $\alpha_{2\pm2}$, $\alpha_{2\pm1}$), which can be reduced to three (two independent) considering rotation[1], which will coincide the intrinsic frame with axes (1, 2, 3) with the principal axes of the system (x, y, z). The terms α_{21} and α_{2-1} vanish ($\alpha_{2\pm1} = 0$) and the system is described by the three Euler[2] angles and the two remaining terms α_{20}, $\alpha_{22} = \alpha_{2-2}$ [11]. In this respect, α_{20} and $\alpha_{2\pm2}$ can be expressed by the polar coordinates (β_2, γ) as

$$\begin{aligned} \alpha_{20} &= \beta_2 \cos\gamma, \\ \alpha_{2\pm2} &= \frac{1}{\sqrt{2}} \beta_2 \sin\gamma, \end{aligned} \tag{2.12}$$

where β_2 and γ measure the total deformation and the lengths along the principal axes, respectively, according to the following equations

$$\beta_2^2 = \sum_{\mu} |\alpha_{2\mu}|^2 = \alpha_{20}^2 + 2\alpha_{22}^2, \tag{2.13}$$

[1]There are still five parameters: three Euler angles (these are just transformations from lab to intrinsic frames) and α_{20}, α_{22}.

[2]Euler's rotation theorem: Any rotation may be described using three angles.

$$\delta R_x = R_o\sqrt{\frac{5}{4\pi}}\beta_2 \cos\left(\gamma - \frac{2\pi}{3}\right),$$
$$\delta R_y = R_o\sqrt{\frac{5}{4\pi}}\beta_2 \cos\left(\gamma + \frac{2\pi}{3}\right), \tag{2.14}$$
$$\delta R_z = R_o\sqrt{\frac{5}{4\pi}}\beta_2 \cos\left(\gamma\right).$$

The Lund convention [16], as illustrated in Fig. 2.4, describes quadrupole nuclear shapes in the (β_2, γ) plane. To describe all possible shapes relative to the rotation axis a range of $-120° \leq \gamma \leq +60°$ is required. Axially symmetric shapes occur when γ is a multiple of 60°, e.g. for $\gamma = 0°, -120°$ prolate shapes are described, while for $\gamma = \pm 60°$ oblate shapes are described, as illustrated in Fig. 2.4. The most collective shape is met for $\gamma = -30°$, where the collective moment of inertia is maximum. The collective regime extends for values $-60° \leq \gamma \leq 0°$. All the possible shapes are illustrated in Fig. 2.5.

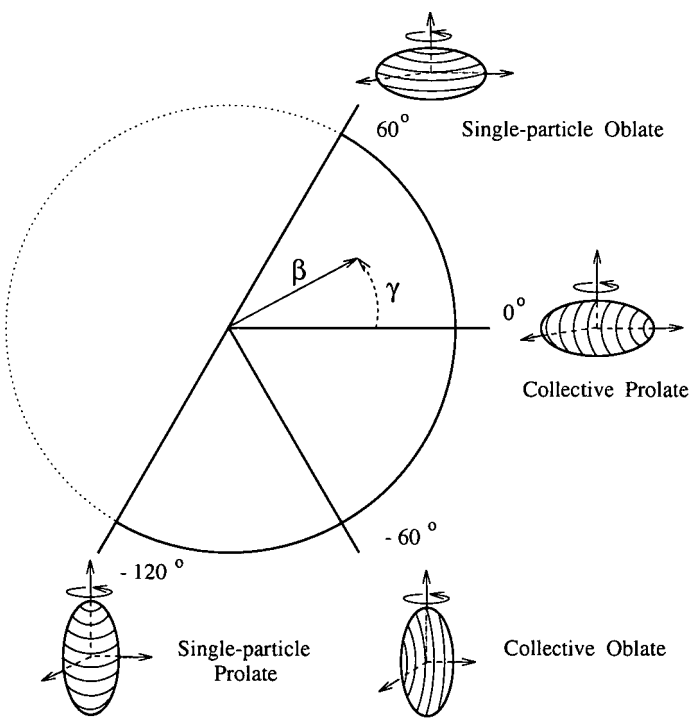

Figure 2.4: The Lund convention of nuclear shapes and rotations.

2.4 Nilsson Potential

Assuming an ellipsoidally deformed nucleus, i.e. an ellipsoidal average potential, Sven Gösta Nilsson [17] introduced the anisotropic harmonic oscillator Hamiltonian (H_o), describing decoupled oscillations parallel and perpendicular to the deformation axis (z), plus two extra terms in order to reproduce single-particle levels in nuclei with

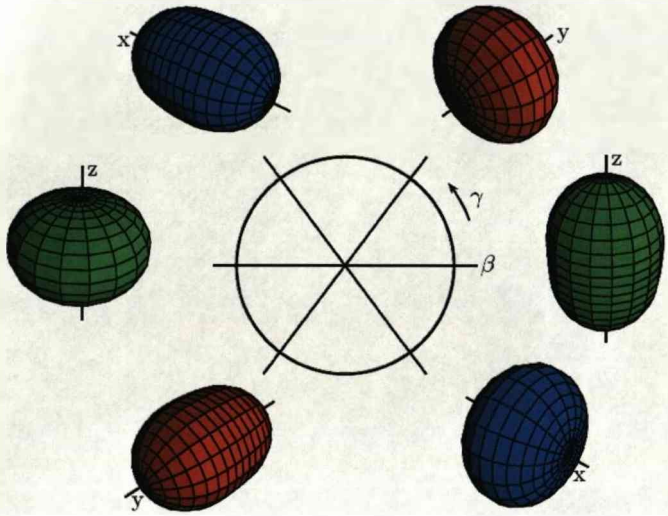

Figure 2.5: For γ values of $0°$ and $\pm 120°$ prolate (axial) shapes are described, while for γ values of $\pm 60°$ and $-180°$ oblate (axial) shapes are described. For all other values of γ the nucleus presents a triaxial shape (axes lengths: $x \neq y \neq z$).

pronounced deformed shapes on the basis of independent particle motion in an average field. The form of the Hamiltonian he initially used for this purpose is the following

$$H = H_o + C\boldsymbol{\ell} \cdot \boldsymbol{s} + D\boldsymbol{\ell}^2, \tag{2.15}$$

where

$$H_o = -\frac{\hbar^2}{2m}\nabla^2 + \frac{m}{2}\omega_\perp^2 \left(x^2 + y^2\right) + \frac{m}{2}\omega_z^2 z^2. \tag{2.16}$$

The coefficient (C) in the spin-orbit term of Eq. 2.15 defines the strength of the spin-orbit force, while the last term provides the modification needed for a more realistic or "Woods-Saxon" like potential. The frequency $\omega_\perp$ $(\omega_\perp^2 = \omega_x^2 = \omega_y^2)$ comes from the axially symmetric shape assumption with the z-axis as the symmetry axis. The deformation depends on the difference between the two oscillator frequencies $\omega_\perp$ and ω_z and an elongation parameter ε is introduced via the equations

$$\omega_\perp = \omega_o(\varepsilon)\left(1 + \frac{1}{3}\varepsilon\right), \tag{2.17}$$

$$\omega_z = \omega_o(\varepsilon)\left(1 - \frac{2}{3}\varepsilon\right). \tag{2.18}$$

From the definition of ε prolate shapes are described for positive values $(\varepsilon > 0)$ and oblate shapes for negative values $(\varepsilon < 0)$, while the volume conservation condition is fulfilled for

$$\omega_x\omega_y\omega_z = \text{constant} = \mathring{\omega}_o^3 = (\omega_o(\varepsilon = 0))^3. \tag{2.19}$$

The harmonic oscillator quantum ω_o is determined from Ref. [18] as

$$\hbar\omega_o = 41\mathrm{A}^{-1/3}\left[1 \pm \frac{1}{3}\frac{\mathrm{N}-\mathrm{Z}}{\mathrm{A}}\right]\mathrm{MeV}, \tag{2.20}$$

where the minus sign is used for protons and the plus sign for neutrons. The third term of Eq. 2.15 was later changed since it was noticed that for large N quantum numbers[3] the shift in the levels was too strong. Eq. 2.15 then takes the form

$$H = H_o + C\boldsymbol{\ell}\cdot\boldsymbol{s} + D(\boldsymbol{\ell}^2 - \langle\boldsymbol{\ell}^2\rangle_N). \tag{2.21}$$

The analytical solutions of Eq. 2.16 can be found in many textbooks, such as [11, 19, 20] etc. For the needs of this text only the results of these solutions will be mentioned. The eigenstates of H_o in the cylindrical basis can be characterised by the "Nilsson quantum numbers" or asymptotic quantum numbers

$$\Omega^\pi[Nn_z m_\ell],$$

where $\Omega = m_\ell \pm \frac{1}{2}$ is the z-component of the total angular momentum, $\pi = (-1)^\ell$ is the parity of the state and m_ℓ the projection of the orbital angular momentum onto the symmetry axis z. Another notation in this model uses the letters Λ and Σ for the projections of ℓ and s, respectively, as illustrated in Fig. 2.6. In the case of multiparticle configurations, an additional quantum number K is defined as

$$K = \sum_i \Omega_i. \tag{2.22}$$

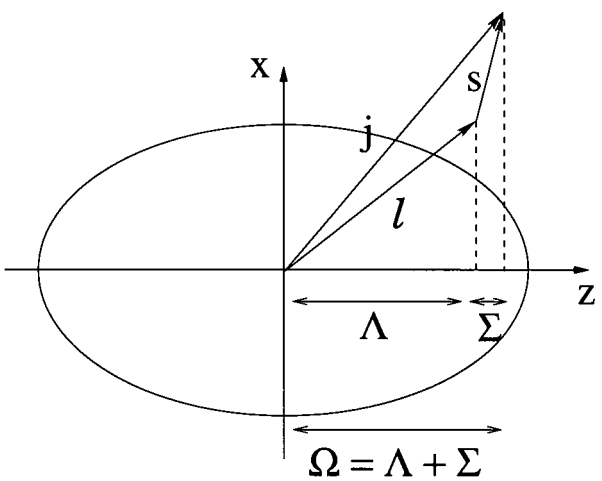

Figure 2.6: Quantum numbers defining nuclear angular momenta and their projections on the symmetry axis.

[3] $N = n_z + n_\perp$ the number of quanta in the oscillator.

The constants C and D of Eq. 2.21 may also be expressed as

$$C = -2\hbar\mathring{\omega}_o\kappa, \tag{2.23}$$

$$D = -\hbar\mathring{\omega}_o\kappa\mu. \tag{2.24}$$

In order to obtain a satisfactory reproduction of the nuclear levels, the values of μ and κ are obtained by fitting experimental data [21]. Their values vary according to each shell. A Coulomb term is also incorporated in these values and for zero deformation the already known nuclear levels must be reproduced.

The single-particle levels that emerge using the formalism described in this section can be seen in Figs. 2.7 and 2.8, where the Nilsson levels for protons and neutrons, respectively, as a function of the quadrupole deformation ε_2 are illustrated for nucleon numbers between the 50 and 82 shell closures. One can comment on the following characteristics of these diagrams:

- Each spherical shell-model state level splits into $(2j + 1)/2$ levels for non-zero deformation.
- Each level has a twofold degeneracy ($\pm\Omega$) due to the time-reversal symmetry, as illustrated in Fig. 2.9.
- The "Nilsson quantum numbers" are not conserved for small values of deformation, but are still used to classify the levels.
- For fixed values of Ω there is an opposite shift of the level energy depending on the sign of the deformation parameter ε. For small values of Ω the level is shifted downwards for prolate deformation, $\varepsilon > 0$, and upwards for oblate deformation, $\varepsilon < 0$; low-Ω states favour prolate shapes, while high-Ω states favour oblate shapes, as explained in Fig. 2.9.
- As the deformation parameter changes towards greater absolute values, there is an increasing mixing in the single-particle states, especially for high-j orbitals, where the splitting in levels is even bigger.

Presently, there are several models based on different potentials that can be used to calculate single-particle energies as a function of deformation. Although the potential used is not always the anisotropic harmonic oscillator, the resulting diagrams are generically called "Nilsson diagrams".

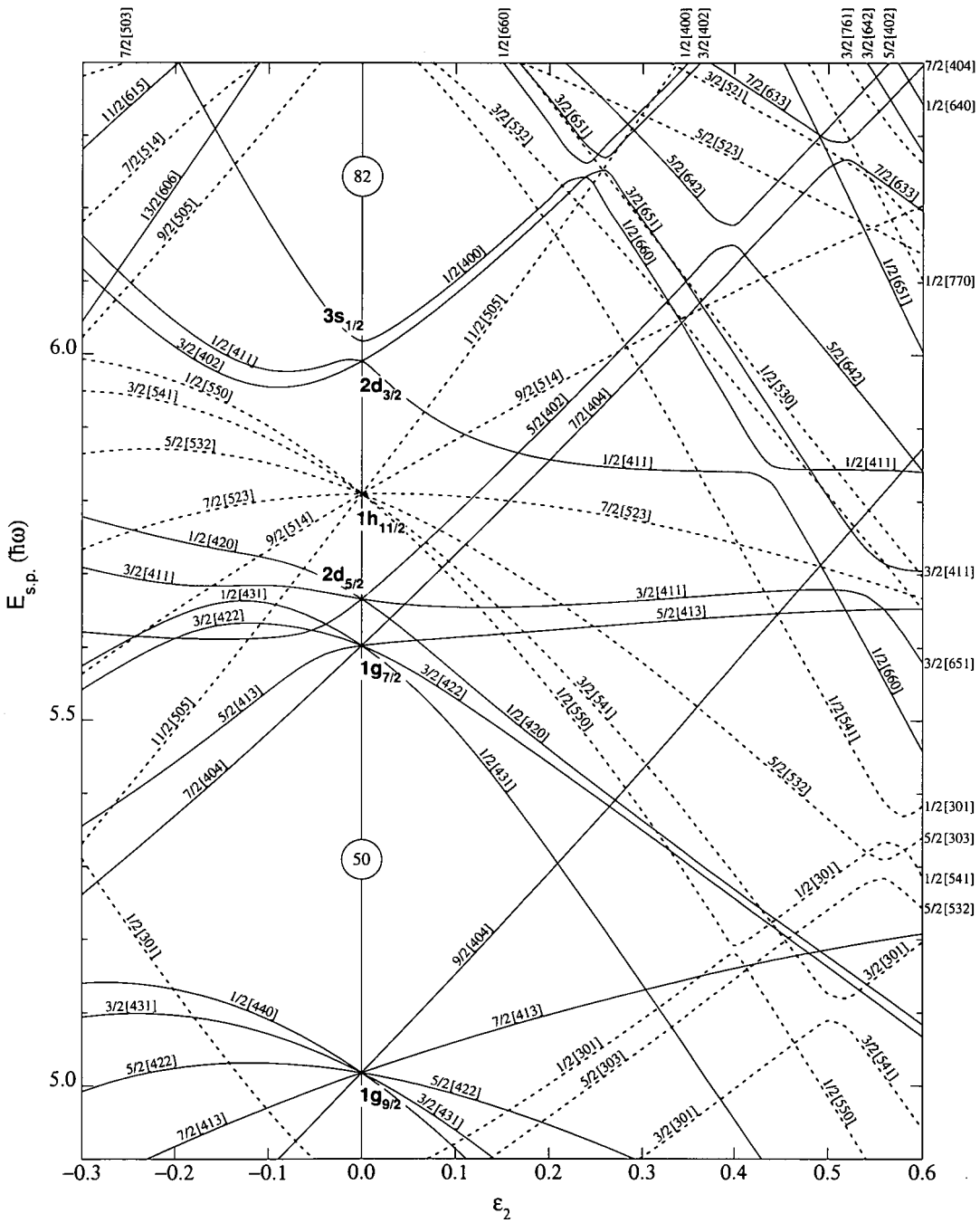

Figure 2.7: Single-particle energies (in units of oscillator energy $\hbar\omega_0$) as a function of deformation ε_2 using the Nilsson potential for proton number $50 < Z < 82$. The solid and dashed lines distinguish positive and negative parity levels respectively. For each level the "Nilsson" quantum numbers $\Omega[Nn_z m_\ell]$ are indicated.

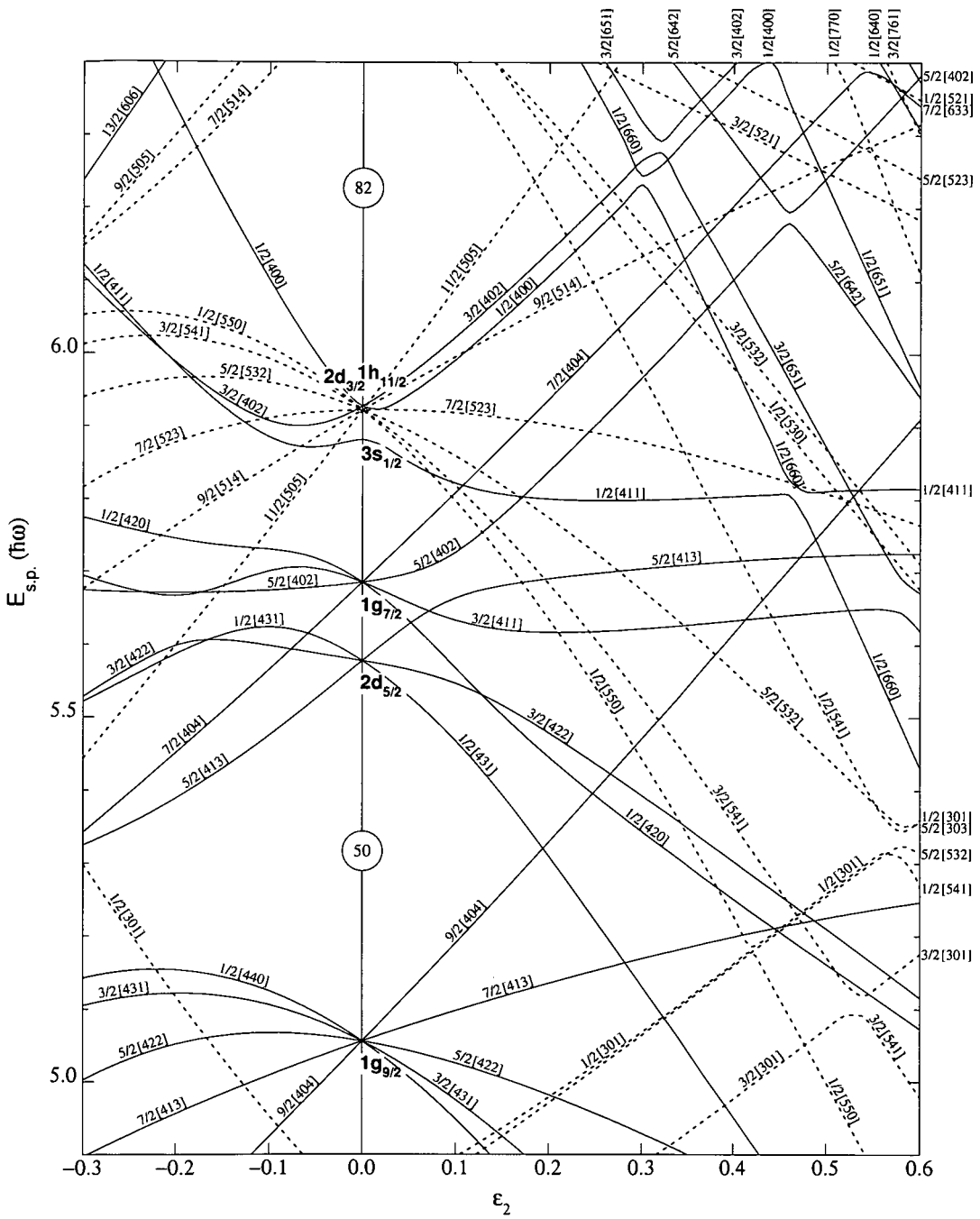

Figure 2.8: Single-particle energies (in units of oscillator energy $\hbar\omega_0$) as a function of deformation ε_2 using the Nilsson potential for neutron number $50 < N < 82$. The solid and dashed lines distinguish positive and negative parity levels respectively. For each level the "Nilsson" quantum numbers $\Omega[Nn_z m_\ell]$ are indicated.

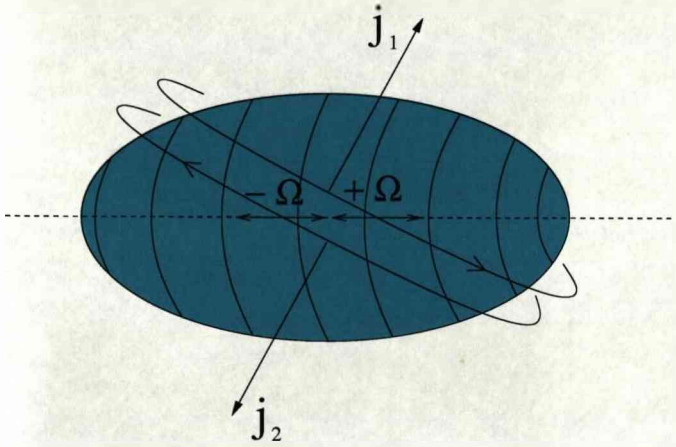

Figure 2.9: Pairing is a phenomenon evident in many experimental findings. This attractive force acts on nucleons in the same j orbital and pairs them such that $J = j_1 + j_2 = 0$. These pairs can be described as nucleons in time-reversed orbitals (velocities of opposite sign), as the idea of nucleons being in exactly the same state is excluded by the Pauli principle. For low Ω values, there is a large overlap between the prolate core and the single-particle orbit, which is energetically favoured.

2.5 Nuclear Rotation

As stated in the introduction of this chapter, collective excitations are characterised by the coherent (in-phase) motion of the majority of the nucleons within a nucleus. As such, these excitations can be understood and explained easily if treated macroscopically. The great stability of the magic nuclei has been associated with their spherical shape. However, as one moves away from these closed shells, the nucleus prefers energetically shapes that deviate significantly from that of a sphere, leading to nuclear deformation. This deformation in the nuclear shape induces rotational degrees of freedom, since an orientation in space is defined.

Assuming a deformed nucleus in a three-dimensional space, its orientation can be defined using the Euler angles, $\omega = \theta, \phi, \chi$, while its state of motion can be defined using three quantum numbers [20]. These three quantum numbers are I (the total angular momentum), M (the eigenvalue of the projection of I in a space-fixed coordinate system, i.e. laboratory system) and K (the eigenvalue of the projection of I in a body-fixed coordinate system, i.e. intrinsic system) and can be seen in Fig. 2.10. The wave function of the rotating system can then be expressed as

$$\psi_{IKM} = |IKM\rangle = \sqrt{\frac{2I+1}{8\pi^2}} \mathcal{D}^I_{MK}(\theta, \phi, \chi), \tag{2.25}$$

where $\mathcal{D}^I_{MK}$ are the rotation matrices.

For an axially symmetric deformed nucleus with the z-axis as the symmetry axis, collective rotation can only be defined around an axis different than the symmetry axis

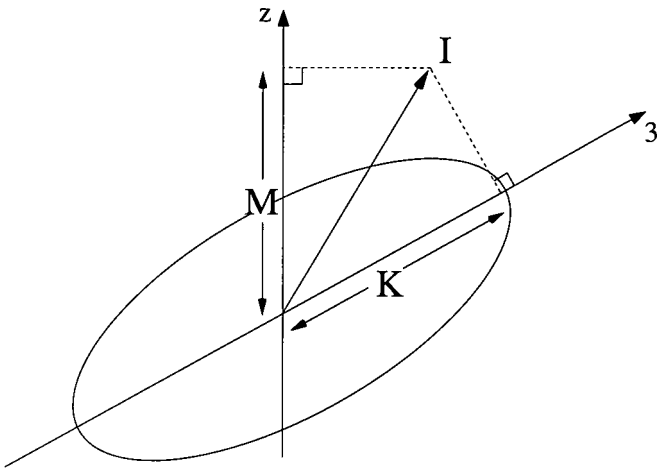

Figure 2.10: The z-axis corresponds to a space-fixed coordinate system, i.e. the laboratory system, while the 3-axis belongs to the intrinsic coordinate system.

and thus perpendicular to it, conventionally the x-axis. This condition is introduced since an orientation cannot be defined quantum mechanically for rotation of the intrinsic system around the symmetry axis, i.e. the system is indistinguishable from the original.

In the case of pure collective rotation the Hamiltonian H_{rot} of the system is

$$H_{rot} = \frac{\hbar^2 \boldsymbol{R}^2}{2\mathcal{J}}, \tag{2.26}$$

where $\boldsymbol{R} = \boldsymbol{I}$ is the total angular momentum of the system originating only from the collective rotation (Fig. 2.11(a)) and $\mathcal{J}$ is the moment of inertia of the system[4]. The energy in the case of pure collective rotation is associated with the total angular momentum as

$$E_I = \frac{\hbar^2}{2\mathcal{J}} I(I+1), \tag{2.27}$$

while the rotational frequency ω between two successive levels $(I+1 \rightarrow I-1)$ in the rotational band of an even-even nucleus can be approximated by the following equation

$$\hbar\omega = \frac{dE}{dI_x} \approx \frac{1}{2}[E_{I+1} - E_{I-1}] = \frac{E_\gamma}{2}. \tag{2.28}$$

In Eq. 2.28 I_x is the projection of I onto the rotation axis and is equal to

$$I_x = \sqrt{I(I+1) - K^2}, \tag{2.29}$$

where K is defined in Eq. 2.22. The value of $\mathcal{J}$ for a rotating nucleus is found between the calculated moment of inertia for a rigid body and that of an incompressible non-viscous fluid, implying that the rotational behaviour lies in between these two limits.

[4]Static moment of inertia $\mathcal{J}^{(0)}$.

In the case where single-particle degrees of freedom contribute to the total angular momentum I by a factor of $J = \sum j$, $\boldsymbol{I} = \boldsymbol{R} + \boldsymbol{J}$ of Fig. 2.11(b), the Hamiltonian of the system can be decomposed in two parts, the collective part and the intrinsic part,

$$H = H_{rot} + H_{int}, \tag{2.30}$$

and the wave function is given as

$$\Psi = \phi_{rot}\phi_{int}. \tag{2.31}$$

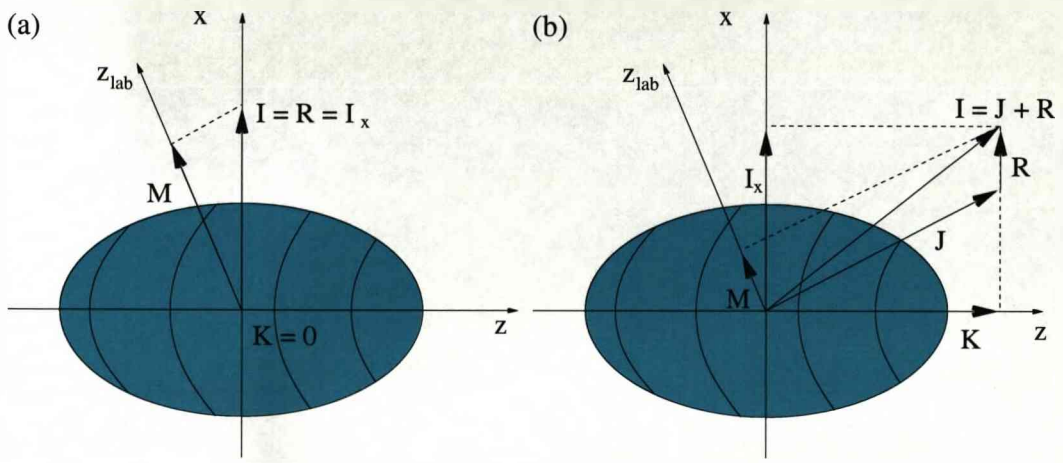

Figure 2.11: Angular momentum coupling. (a) There is no contribution from intrinsic angular momentum J and thus the total angular momentum I comes only from the collective rotation R, $I = R$. An example is the ground state rotational band of an even-even nucleus, where all nucleons are paired resulting to $J = 0$. (b) Contribution to the total spin I from single-particle angular momentum $J = \sum j$.

2.6 Cranked Shell Model

The cranked shell model (CSM) was first introduced in a semiclassical way by D. R. Inglis [22] and provides a microscopic description of nuclear rotation, combining thus both collective and single-particle degrees of freedom. This is achieved by treating collective rotations as rotation of the deformed single-particle potential.

The semiclassical description of the CSM is based on the classical assumption that if one imposes a rotation around an axis (x) perpendicular to the symmetry axis (z) with constant rotational frequency ω, the nucleons can then be treated as independent particles in an average potential that rotates with the rotating frame.

For rotation around the x-axis (ω parallel to the x-axis) the many-body Hamiltonian of the cranking model is given by

$$H_\omega = H - \hbar\omega I_x = \sum_{i=1}^{A} h_\omega^{(i)} = \sum_{i=1}^{A} (h^{(i)} - \hbar\omega j_x^{(i)}), \tag{2.32}$$

where H is the intrinsic single-particle Hamiltonian, I_x is the total angular momentum operator projected on the x-axis and $\hbar\omega I_x$ a factor equivalent to the classical Coriolis and centrifugal forces induced by the rotating frame of reference.

If one wants to include pairing correlations in the cranking model, the Hamiltonian of Eq. 2.32 becomes

$$H_\omega = H - \hbar\omega I_x - \Delta(P^\dagger + P) - \lambda\hat{N}, \tag{2.33}$$

where the operators $P^\dagger$ and P create and destroy the pair field, Δ is the pair gap parameter and the chemical potential λ acting on the particle number operator $\hat{N}$ constrains the number of particles [23].

2.6.1 Signature and Parity

The parity π is a good quantum number for reflection symmetric systems (invariance with respect to space inversion $\mathcal{P}$). The cranking Hamiltonian is also invariant with respect to a rotation of 180° around the x-axis $\mathcal{R}_x = e^{-i\pi I_x}$ [23] (or any axis perpendicular to the symmetry axis),

$$\mathcal{R}_x \psi_i = e^{-i\pi I_x} \psi_i. \tag{2.34}$$

The eigenvalues of $\mathcal{R}_x$ are $r = e^{-i\pi\alpha}$, where r is called the signature quantum number and α the signature exponent quantum number. However, the name signature is most commonly used for the additive quantity α. The single-particle states can then be classified according to their parity π and signature α quantum numbers. The possible values for α are $\alpha_i = \pm\frac{1}{2}$ ($r_i = \mp i$), while the total signature of a system is defined as [24]

$$\alpha_{tot} = \sum_{i\ occ} \alpha_i \ \mathrm{mod} 2, \tag{2.35}$$

$$r_{tot} = \prod_{i\ occ} r_i, \tag{2.36}$$

and its parity given by

$$\pi_{tot} = \prod_{i\ occ} \pi_i. \tag{2.37}$$

α_{tot}	r_{tot}	I
0	+1	0,2,4,...
1	−1	1,3,5,...
$+\frac{1}{2}$	$-i$	$\frac{1}{2}, \frac{5}{2}, \frac{9}{2}$,...
$-\frac{1}{2}$	$+i$	$\frac{3}{2}, \frac{7}{2}, \frac{11}{2}$,...

Table 2.1: Relation between the allowed values of the total angular momentum I and the total signature quantum number [25].

2.6.2 CSM Calculations

In Fig. 2.12 CSM calculations for ^{109}I have been performed with deformation parameters $\beta_2 = 0.143$, $\beta_4 = 0.040$ and $\gamma = 10°$, and the quasiproton and quasineutron Routhians (e') as a function of rotational frequency are shown. The single-particle Routhian e' is the expectation value of the cranking single-particle Hamiltonian $h_\omega^{(i)}$ of Eq. 2.32, $e' = \langle h_\omega^{(i)} \rangle$. The following points are emphasised:

- At $\omega = 0$ the observed levels correspond to the "Nilsson" levels for the given deformation parameters, as seen in Fig. 2.13. However, for low-Ω orbitals or for triaxial shapes an appreciable admixture of the "Nilsson" basis states can occur, as in the case of ^{109}I, see Table 2.2.

- Each level has a twofold degeneracy (time-reversed orbits, $\pm\Omega$). For increasing frequency ω the Coriolis force breaks this symmetry and the levels split into two. These two levels have different "signatures".

- Levels with small Ω- and large j-values show a strong signature splitting as a function of rotational frequency.

- Levels with higher j-values come down stronger with increasing ω.

The theoretical "alignment" of a single-quasiparticle, i.e. the angular momentum component of the quasiparticle along the rotation axis, can be calculated from the slope of its trajectory by the following equation

$$i_\nu = -\frac{\partial e'_\nu(\omega)}{\partial \omega}, \tag{2.38}$$

while for multi-quasiparticle states the theoretical alignment of the configuration is defined as

$$i = \sum_\nu i_\nu, \tag{2.39}$$

where ν denotes the single-quasiparticle configuration.

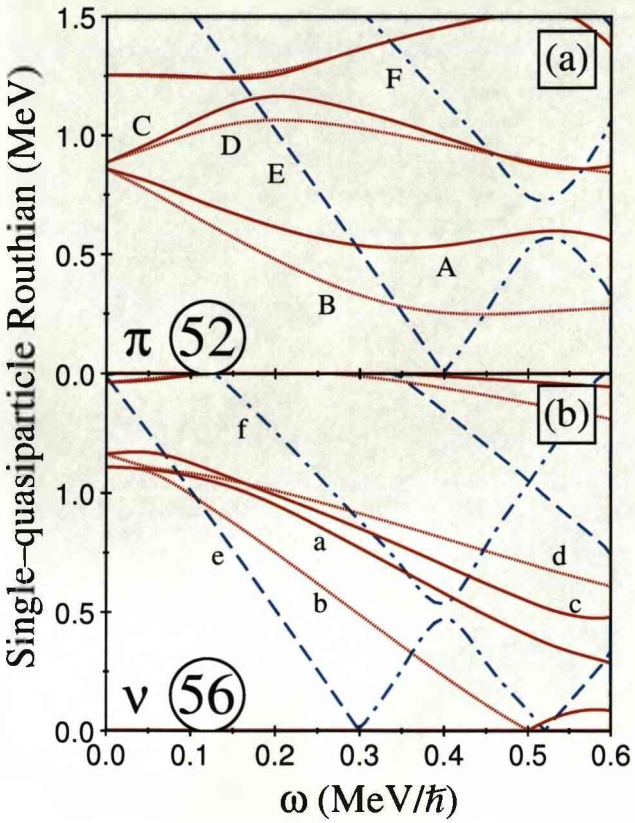

Figure 2.12: Single-quasiparticle positive-parity (red) and negative-parity (blue) proton (a) and neutron (b) levels calculated with a cranked Woods-Saxon potential with deformation parameters $\beta_2 = 0.143$, $\beta_4 = 0.040$, $\gamma = 10°$, and pairing parameters $\Delta_\pi = 0.68$ MeV, $\Delta_\nu = 1.10$ MeV.

Experimental Alignments and Routhians

In order to compare the theoretical calculations with the experimental findings, the experimental alignment (i_x) and Routhian (e') are calculated with the following equations

$$i_x(I) = I_x(I) - I_{x,ref}(I), \tag{2.40}$$

$$e'(I) = E^{\omega}_{expt}(I) - E^{\omega}_{ref}(I), \tag{2.41}$$

where the reference quantity removes contributions from the core, leaving the single-particle contributions to the energy and alignment. The reference quantities $I_{x,ref}(I)$ and $E^{\omega}_{ref}(I)$ are obtained using a reference configuration with a variable moment of inertia $\mathcal{J}^{(1)}_{ref}$ defined as

$$\mathcal{J}^{(1)}_{ref} = \mathcal{J}_0 + \mathcal{J}_1\omega^2, \tag{2.42}$$

Table 2.2: Labelling of single-quasiparticle orbitals of Fig. 2.12. The amplitude of the mixing states at zero frequency is shown. In order to define the Shell Model state the following definitions are stated: $\ell = n_z + m_\ell$, $j = \ell + m_s$ and $\Omega = m_l + m_s$.

Label	(Parity, Signature)	"Nilsson" state	Admixture	Shell Model state
A, B	(+, ±1/2)	[4, 3, 1]1/2	34%	$g_{7/2}$
		[4, 2, 0]1/2	30%	$d_{5/2}$
		[4, 2, 2]3/2	7%	$g_{7/2}$
C, D	(+, ±1/2)	[4, 4, 0]1/2	42%	$g_{9/2}$
		[4, 3, 1]1/2	15%	$g_{7/2}$
		[4, 1, 1]1/2	14%	$d_{3/2}$
E, F	(−, ∓1/2)	[5, 3, 0]1/2	26%	$f_{7/2}$
		[5, 4, 1]1/2	21%	$h_{9/2}$
		[5, 5, 0]1/2	17%	$h_{11/2}$
a, b	(+, ±1/2)			
c, d	(+, ±1/2)			
e, f	(−, ∓1/2)			

where $\mathcal{J}_0$ and $\mathcal{J}_1$ are the Harris parameters [26]. The reference quantities $I_{x,ref}(I)$ and $E^{\omega}_{ref}(I)$ are expressed as

$$I_{x,ref}(I) = \omega \left[\mathcal{J}_0 + \mathcal{J}_1 \omega^2\right] + i_x, \tag{2.43}$$

$$E^{\omega}_{ref}(I) = -\frac{1}{2}\omega^2 \mathcal{J}_0 - \frac{1}{4}\omega^4 \mathcal{J}_1 + \frac{1}{8}\frac{\hbar^2}{\mathcal{J}_0}, \tag{2.44}$$

where $i_x = 0$ for the ground-state band of an even-even nucleus.

2.7 Total Routhian Surfaces (TRS)

The TRS cranking calculations provide a detailed description of the nuclear shape for various quasi-particle configurations and rotational frequencies and are used to interpret nuclear structure features. The TRS formalism calculates the total routhian, i.e. energy in the rotating frame of a nucleus (N, Z) with a given quasi-particle configuration ν, using a universal Woods-Saxon single-particle potential [27], according to the following equation

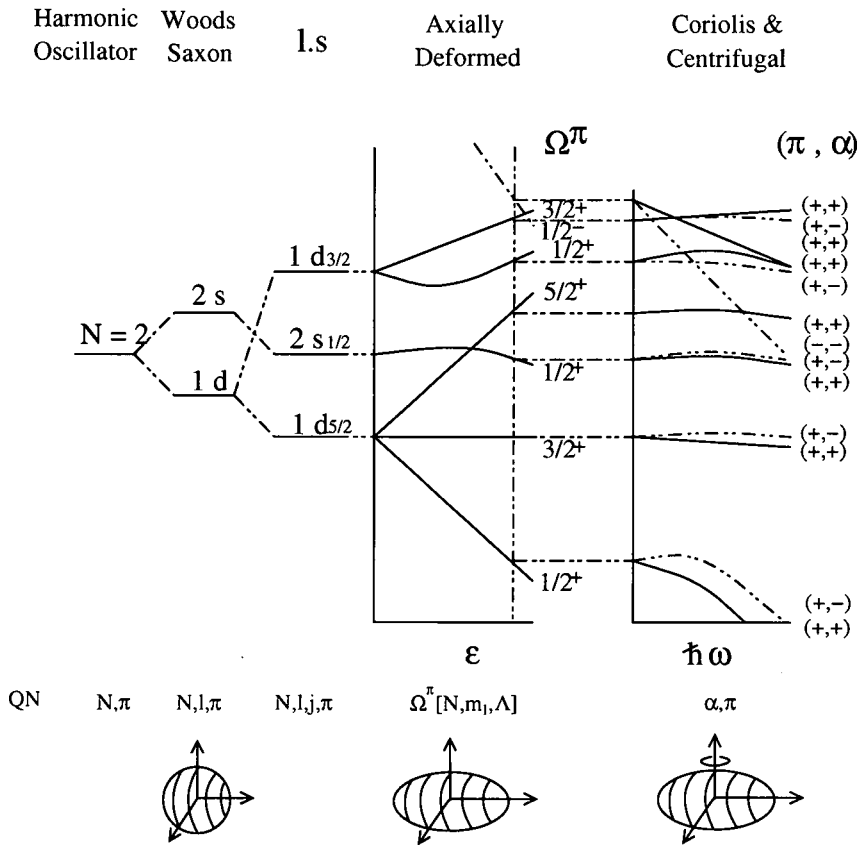

Figure 2.13: Breaking of symmetries and evolution of structure when deformation and/or rotation is applied on a nuclear system. The single-particle levels are calculated using the shell model for spherical nuclei, the Nilsson model when deformation arises and the CSM when rotation is applied.

$$E^{\omega}(\hat{\beta},\mathrm{N},\mathrm{Z},\nu) = E^{\omega=0}_{Str}(\hat{\beta},\mathrm{N},\mathrm{Z},\nu) + \left(\langle\Psi^{\omega}|H^{\omega}|\Psi^{\omega}\rangle_{\hat{\beta},\mathrm{N},\mathrm{Z},\nu} - \langle\Psi^{\omega}|H^{\omega}|\Psi^{\omega}\rangle^{\omega=0}_{\hat{\beta},\mathrm{N},\mathrm{Z},\nu}\right). \tag{2.45}$$

In Eq. 2.45 $\hat{\beta}$ denotes the deformation parameters β_2, β_4 and γ. $E^{\omega=0}_{Str}$ represents the Strutinsky energy at $\hbar\omega = 0$ MeV, i.e. the energy calculated from the Liquid Drop Model and corrected for shell effects using the Strutinsky method [28, 29]. The second term of Eq. 2.45 represents the cranking energy, i.e. the energy gained due to the collective rotation and single-particle alignment. The nuclear properties are deduced by minimising this energy with respect to the deformation parameters β_2 and γ. In Fig. 2.14 the results from TRS calculations performed for ^{109}I are presented.

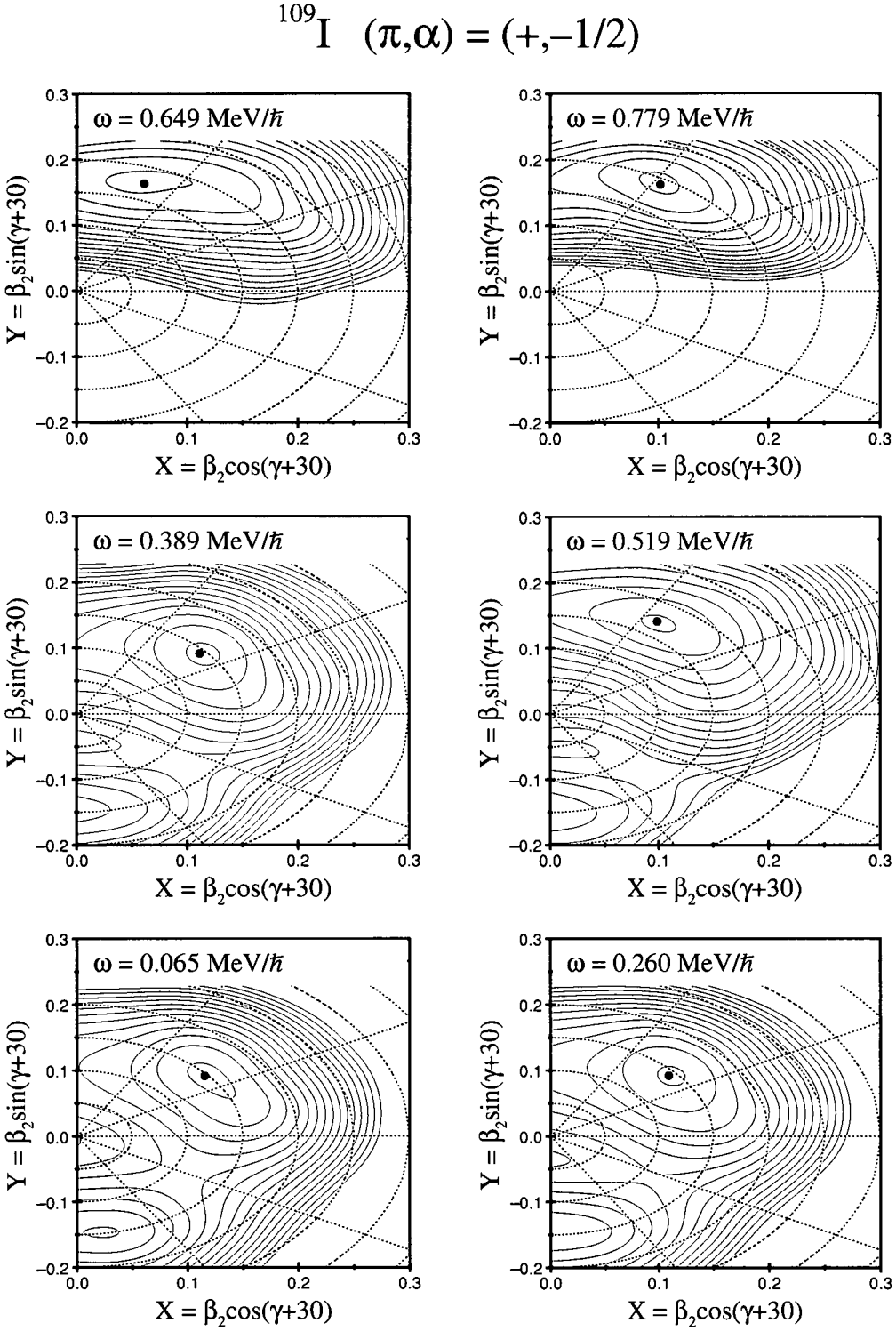

Figure 2.14: ^{109}I TRS calculations for six rotational frequencies. The chosen configuration involves the odd proton in the B orbital $(+,-1/2)$. The energy contours are separated by 250 keV.

Chapter 3

Experimental Techniques and Apparatus

Probing nuclear properties is mainly achieved indirectly by the interaction (nuclear or electromagnetic) of two nuclei. This imposes technical challenges, that always limit our understanding of nuclear physics. Over the last $\sim$ 100 years that nuclear physics has existed, since the discovery of radioactivity by Becquerel in 1896 and the first nuclear reaction experiment in 1932, the technological progress achieved up to now is outstanding. State-of-the-art detection systems, accelerators and powerful analytical techniques have given a big boost in the exploration of the still "unknown" territory of nuclear physics.

In this chapter a brief overview of the experimental apparatus and techniques used today in nuclear physics will be stated, focusing on the instruments used for this thesis.

3.1 Particle Accelerators

An accelerator provides the sufficient kinetic energy that a particle needs in order to interact with a nucleus. As stated in its name, it accelerates charged particles up to a desired energy and directs them onto a target for a nuclear reaction to occur. Accelerators can be categorised in five different general groups [30]: electrostatic accelerators, cyclotrons, synchrotrons, linear accelerators and colliding-beam accelerators. For the needs of this thesis only cyclotrons will be briefly described in the following section.

3.1.1 Cyclotron Accelerators

Cyclotron accelerators can be further categorised in the magnetic resonance accelerator (cyclotron), the sector-focusing or AVF (azimuthally varying field) or isochronous cyclotron and the synchrocyclotron.

In a cyclotron the ions of charge q execute semicircular orbits of radius r in the "D" electrodes ("dees"), due to the centripetal Lorentz force F induced by the magnetic field B

$$F = qvB = \frac{mv^2}{r}, \tag{3.1}$$

while they are accelerated in between the two "dees" by an increased electric field if the frequency of the alternating voltage is

$$\nu = \frac{qB}{2\pi m}. \tag{3.2}$$

The maximum kinetic energy T of the particles when they exit the cyclotron depends on the radius of the cyclotron and the magnitude of the magnetic field that is applied and is defined as

$$T = \frac{1}{2}mv_{max}^2 = \frac{q^2B^2R^2}{2m}. \tag{3.3}$$

With increasing velocity into the relativistic region, the mass of the particles increases and the resonant condition of Eq. 3.2 is no longer fulfilled. One way to compensate for this effect is by increasing the magnetic field in the regions where the particles become relativistic, i.e. at the larger radii. This increase in the field, however, applies defocusing effects in the beam. The way to correct for these is by the azimuthal variations of the magnetic field, illustrated in Fig. 3.1.

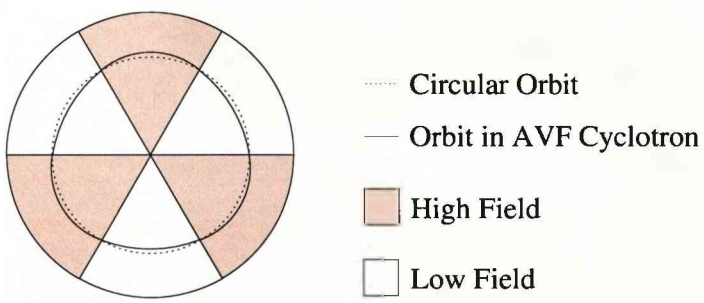

Figure 3.1: The magnetic field in an AVF cyclotron is separated into sectors of low (focusing) and high (defocusing) field. The stable orbit is not circular with the particles performing radial oscillations around a circle.

The maximum energy of a beam of mass A and charge state n ($Q = ne$) that can be delivered from a cyclotron is given by the factor K,

$$K = \frac{T\mathrm{A}}{n^2}. \tag{3.4}$$

A specific design of the AVF cyclotron, where the magnetic field is provided by a number of magnetic sectors, leads to the separated sector cyclotron or ring cyclotron.

These cyclotrons provide better vertical orbit stability. There is a number of separated cavities, where an RF generator increases the energy of the particles. The work in this thesis was carried out using AVF cyclotrons.

3.2 Radioactive-Ion Beams

Over the last years great effort has been focused on the production of radioactive-ion beams (RIBs), which open a new perspective in the study of the nucleus. The GANIL (Grand Accélérateur National d'Ions Lourds) facility [31] at Caen, France, has an active role in the development of such beams with the current SPIRAL I and the upcoming SPIRAL II facilities.

3.2.1 The SPIRAL Facility

The SPIRAL (Système de Production d'Ions Radioactifs et d'Accélération en Ligne) facility [32, 33], shown in Fig. 3.2, employs the ISOL (Isotope Separator On Line) technique for the production of RIBs. The first RIB that was delivered by the SPIRAL facility for experimental use dates back to 2001.

The primary beam, produced by an ECR (Electron Cyclotron Resonance) ion source and accelerated by one of the two compact cyclotrons C01 or C02 ($K = 28$ MeV) of GANIL, is further accelerated by the two separated sector cyclotrons $K = 380$ MeV CSS1 and CSS2 (Cyclotrons à Secteurs Séparés) at high energy; in Fig. 3.3 a diagram of the GANIL cyclotrons is shown. The intense beam is then fragmented onto a production target. The radioactive atoms are transfered to an ECR type system where the ionisation of the atoms takes place. The extracted low-energy RIB is then injected into the $K = 265$ MeV CIME (Cyclotron pour Ions de Moyenne Énergie) cyclotron [34] and post accelerated up to energies of 25 MeV/u. The extracted RIB is then delivered to the α spectrometer, where the nuclei of interest are selected according to their magnetic rigidity. The pure RIB is finally directed to the experimental areas of the GANIL facility, shown in Fig. 3.3.

3.3 Heavy-Ion Fusion-Evaporation Reactions

Heavy-ion (A $\geq$ 40 [37]) fusion-evaporation reactions are widely used as a spectroscopic tool for nuclear structure studies. The unique aspects of this reaction mechanism involves the high angular momentum (up to about 80 $\hbar$) that can be imparted to the compound nucleus and its high excitation energy (up to several hundred MeV). The "hot" compound system gives the opportunity to study near-yrast nuclear states and nuclear matter in conditions unaccessible by any other reaction mechanism. Also, by fusion-evaporation reactions one can produce very proton-rich nuclei.

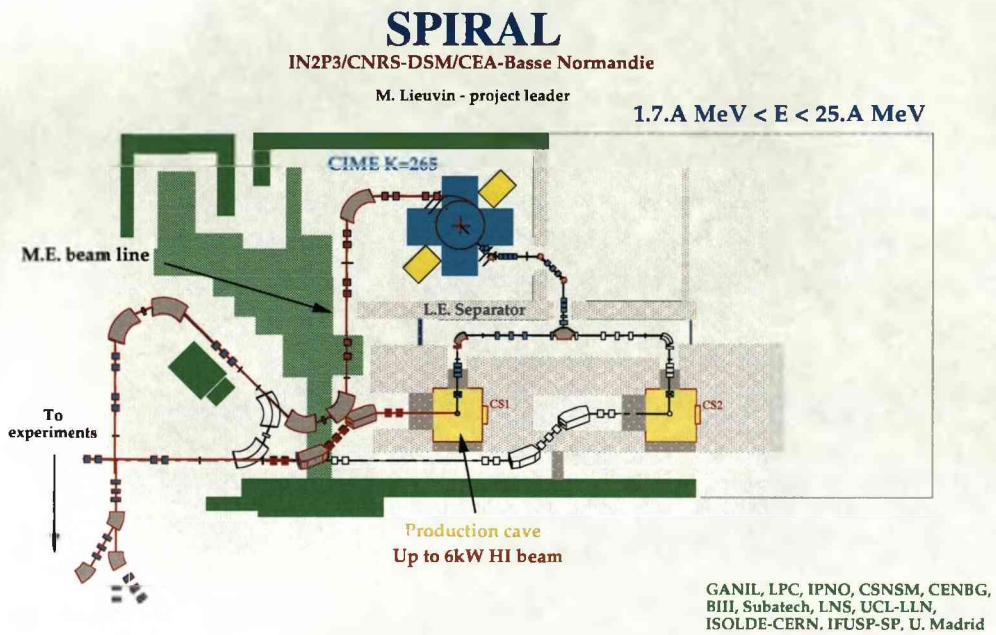

Figure 3.2: The SPIRAL facility. The picture is taken from Ref. [35].

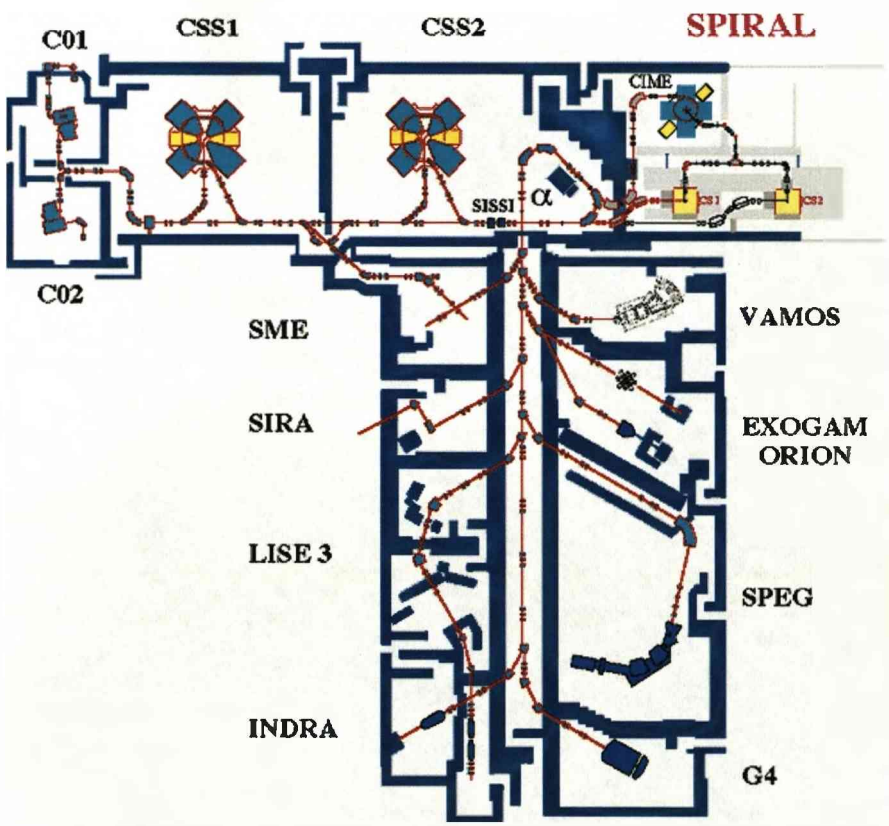

Figure 3.3: The experimental halls at GANIL. The picture is taken from Ref. [36].

The reaction mechanism that predominates when two ions interact depends on the energy of the projectile. At low energies, where the Coulomb barrier cannot be penetrated, Coulomb effects dominate, i.e. Coulomb excitation, Rutherford scattering. If the projectile has sufficient energy to overcome the Coulomb barrier and the associated wavelength is comparable to the nuclear dimensions, nuclear interactions occur. The different types of interaction that can occur depend on the impact parameter, b, of the two ions and are shown qualitatively in Fig. 3.4; the dotted line defines the distance above which the nuclear interactions are negligible.

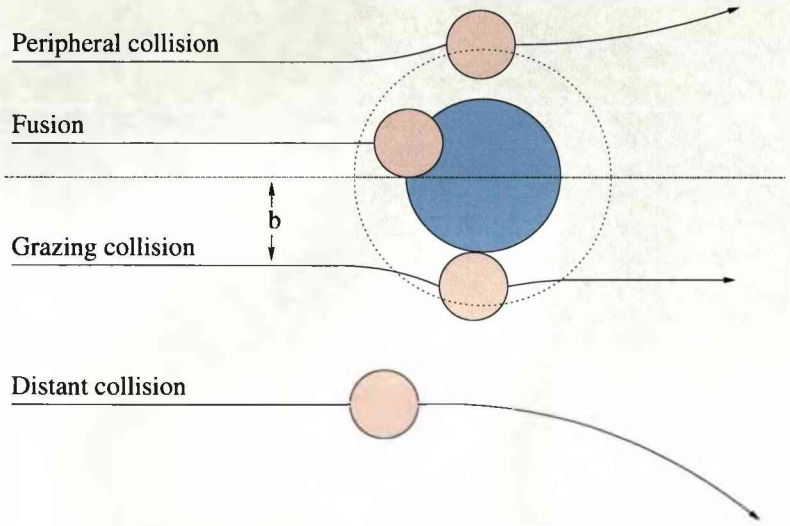

Figure 3.4: Various types of nuclear reactions, i.e. peripheral collisions (elastic scattering, direct reactions), grazing collisions (incomplete fusion, deep inelastic collisions) and distant collisions (elastic (Rutherford) scattering, Coulomb excitations).

3.3.1 Formation and Decay of the Compound System

In heavy-ion fusion reactions the compound system lies far from a statistical equilibrium. Its excitation energy is roughly constant, while the angular momentum of the system presents a broad distribution. If the system "survives" fission or other competing effects, it evaporates particles, mainly neutrons, protons, alphas, and emits γ rays in the process of thermalisation. If one assumes for simplicity only neutron evaporation from the highly unstable compound system, the de-excitation of this system proceeds as follows:

1. Evaporation of neutrons takes place in order to "cool" the highly excited compound system. Each neutron carries away energy equal to the neutron separation energy ($\sim$ 8 MeV) plus the kinetic energy of the neutron itself. However, the angular momentum reduces only by one or two units. The system will continue to evaporate several neutrons until it reaches an energy that is roughly equal or less

than the neutron separation energy. At this point the system cannot de-excite any more via neutron emission. This process takes the compound system in an approximately downward path in the E_x versus I plane of Fig. 3.5.

2. Since neutron emission is strongly inhibited, γ-ray emission takes over. The de-excitation of the system proceeds initially as a "statistical cascade" of dipole γ rays and eventually follows the yrast line to the ground state (predominately via quadrupole electromagnetic transitions). The line in the E_x versus I plane of Fig. 3.5, below which the γ-ray emission dominates, defines the entry line.

Some characteristics of the decay of the compound system are stated below.

- The number of evaporated nucleons decreases with increasing angular momentum, since the capability to remove angular momentum varies according to the decay mode. In Ref. [37] the ratio of the angular momentum in units of $\hbar$ carried away by the emitted radiation to the associate change in excitation energy is presented; typical values of 0.1 to 0.2 MeV^{-1} for nucleon emission (n or p), 0.25 to 0.4 MeV^{-1} for α emission and larger than 1 MeV^{-1} for fission and γ emission are stated.

- The lifetime of the compound system is short, typically of the order of 10^{-20} s.

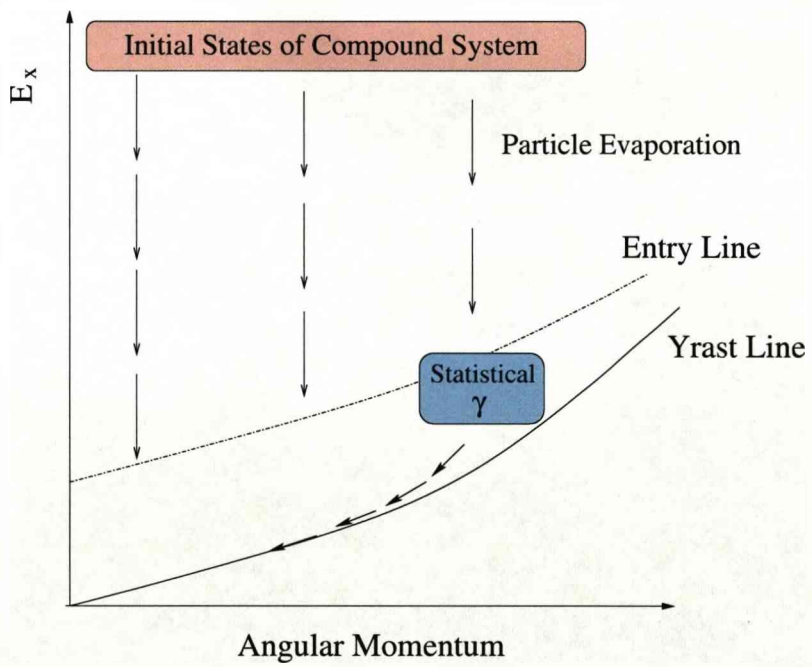

Figure 3.5: De-excitation of the compound system in the excitation energy (E_x) versus the angular momentum (I) plane.

3.4 Scintillation Detectors

Scintillation detectors constitute one of the oldest and most important radiation detectors. Their detection principle is based on the collection of visible light emitted by certain materials when interacting with an ionising radiation. The scintillation light is then converted into an electrical pulse using appropriate light sensors, such as photomultiplier tubes and photodiodes, and information on the energy and the type of the radiation can be extracted. Depending on their material, the scintillation detectors are distinguished as either organic, i.e. organic-based liquids and plastics, or inorganic, i.e. alkali halide crystals, gaseous scintillators and glasses.

3.4.1 Inorganic Scintillators

Inorganic scintillators are doped with small amounts of an impurity in order to perform more efficiently. This activator (impurity) creates energy levels in certain sites of the lattice of the scintillator that lie between the valence and the conduction bands, as illustrated in Fig. 3.6. When an ionising radiation interacts with the scintillation material, its atoms get excited. Their de-excitation through the activator's states results in the emission of fluorescence light. The presence of the activator serves another important role, as the different de-excitation energy than that of the crystal lattice results in a transparency to the scintillation light. However, not all inorganic scintillators include activators.

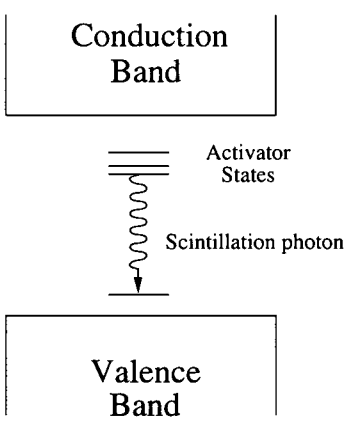

Figure 3.6: Energy band structure of an activated inorganic scintillator.

3.4.2 Caesium Iodide

Caesium Iodide doped with Thallium (CsI(Tl)) is a widely used inorganic scintillator for the detection of charged particles and γ rays. Its unique feature is the different time response (decay time) that it presents depending on the radiation type it interacted with, giving thus the opportunity to distinguish between different particles by applying pulse shape discrimination techniques.

The decay of the photons during the scintillation process is described by the following equation

$$N = A \exp\left(\frac{-t}{\tau_f}\right) + B \exp\left(\frac{-t}{\tau_s}\right), \tag{3.5}$$

where τ_f and τ_s are the decay constants of fast and slow pulses, respectively, which correspond to the de-excitation of different states of the scintillator. In most scintillators the fast component is dominant. In CsI(Tl), however, these two components play both an important role in the decay time of the emitted light pulse and their relative intensity depends on the energy loss (dE/dx) of the interacting radiation. Thus pulse shape discrimination techniques can be used to distinguish between different types of particles. Characteristic decay times for α particles and protons in CsI(Tl) are 0.425 μs and 0.519 μs, respectively [38].

3.4.3 Bismuth Germanate

Bismuth Germanate $Bi_4Ge_3O_{12}$ (BGO) constitutes a widely used inorganic scintillator in γ-ray spectroscopy. This scintillation material is characterised by its high density and large atomic number of the Bismuth component, which leads to the high absorption efficiency of γ rays (high efficiency for the photoelectric conversion of γ rays). Its energy resolution, however, is bad. Thus BGO is used mostly as the Compton-suppression shield of the Ge detectors described in Section 3.8.

This non-alkali material is a "pure" inorganic scintillator, because it does not require an impurity to promote the scintillation process. The luminescence in this case is associated with an optical transition of the Bi^{3+} ion that is a major constituent of the crystal [39].

3.5 Semiconductor Detectors

The most commonly used semiconductor detectors are built from silicon and germanium. A crystalline material that presents a band gap between the valence and the conduction band of the order of $\approx$ 1 eV is considered as a semiconductor. This band gap can be overcome by electrons via thermal excitation and electron-hole pairs can be created in the conduction and valence band, respectively. In the ideal case of a pure semiconductor the electrons and holes that are created are exactly the same in number. Semiconductor materials, however, always include an impurity in small concentrations, which, depending on its characteristics, can distinguish the material in n-type or p-type semiconductors, resulting in an excess of electrons or holes, respectively.

The n-type semiconductors include donor impurities, which contribute electrons in the conduction band, thermally excited from the donor levels, without corresponding

holes in the valence band. Similarly, the p-type semiconductors' acceptor impurities contribute holes to the valence band.

The detection principle of semiconductors is based on the creation of electron-hole pairs along the path of the ionising radiation they interacted with. The number of electron-hole pairs is relative to the energy of the radiation and their collection is achieved by applying an electric field. The n- and p-type semiconductors, however, cannot be used as they are for this purpose, since they present a finite conductivity, leading to the so called leakage current, which induces a great amount of noise. In order to compensate for this leakage current, a semiconductor junction must be created. There are several different configurations for this junction. The most commonly used junction, i.e. the pn-junction, will be briefly described. The pn-junction is created by bringing into contact an n-type and a p-type semiconductor material. In this way an electric field is built across the junction (the p-region becomes negative and the n-region positive) and a depletion zone is created, where there are no charge carriers. If radiation passes through this region, electron-hole pairs will be created and swept out by the electric field. In order to increase this region and for more efficient charge collection, a reversed bias is applied to the pn-junction (Fig. 3.7).

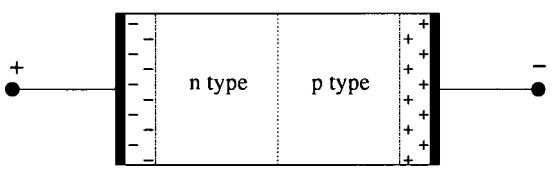

Figure 3.7: A pn-junction in reverse bias.

3.5.1 High Purity Germanium Detectors

The High Purity Germanium (HPGe) detector is used in γ-ray spectroscopic investigations. Highly penetrating γ rays induce the need for bigger depletion zones in Ge detectors, i.e. larger active area for radiation detection, which can be achieved with a Ge detector that has been highly purified [39]. The HPGe constitutes such a detector, with an impurity concentration of less than 10^{10} atoms/cm^3.

The band gap in Ge is of the order of ≈ 0.7 eV. In order to minimise the thermally induced leakage current, HPGe detectors are cooled to 77 K with the use of liquid nitrogen, which is kept in thermal contact with the material. The low ionisation energy of HPGe detectors of the order of ≈ 3 eV results in the collection of a large number of electron-hole pairs for a given γ-ray interaction. This contributes to an excellent energy resolution and relatively large signal-to-noise ratio.

3.5.2 Silicon Detectors

Silicon detectors are used for charged-particle detection. Their big advantage is that they can operate at room temperature. These detectors provide good energy resolution, excellent timing characteristics and exceptional stability. Since the mid-1980's segmented silicon detectors have been in use; the most commonly used geometry is a series of constant pitch, parallel strips with the generic title of silicon strip detectors. The double sided silicon strip detectors (DSSDs), with discrete detector elements on both sides of the detector wafer, provide great position resolution and are widely used in modern nuclear physics experiments.

3.6 Gas Detectors

Gas detectors were the first devices ever to be developed for radiation detection [38]. Their operation principle is based on the collection of the ionisation electrons and ions, as opposed to the electron-hole pairs created in solid-medium detectors, that are created when an ionising particle interacts with the gas in the detector.

There are many types of gas detector that have been used in the past for radiation detection, and are still in use, depending on the experimental needs and the technological progress that has been achieved so far. The ionisation chamber, the proportional counter and the Geiger-Müller counter were mostly used in the past, while the multiwire proportional counter, the drift chamber and many more are mostly used in the present-day experiments.

3.6.1 Multiwire Proportional Counter

The Multiwire Proportional Counter (MWPC) consists of a plane of anode wires centred between two cathode planes. Each anode wire acts like a proportional counter, with its characteristic being the proportionality of the number of electron-ion pairs in the avalanche with the primary electrons created by the incident radiation. Also, position information can be extracted.

3.7 Spectrometers - Separators

3.7.1 Recoil Mass Spectrometers

Recoil mass spectrometers are versatile devices and are widely used in nuclear physics investigations. Their configuration varies according to the experimental goals they serve. Their general description involves a series of optical elements, that provide selectivity and focusing, and a focal plane, where the identification of the recoils takes place. Recoil mass spectrometers can be used as stand-alone devices or can be combined

with various detection systems. In the latter case, they provide a very powerful tool for high selectivity.

3.7.2 Gas-Filled Recoil Separators

In heavy-ion fusion-evaporation reactions the fusion residues can be separated from the primary beam using a combination of electric and/or magnetic elements. A more efficient way of separating particles with a wide range of energies and charge states is the use of a dipole magnet filled with low pressure gas. When the ions travel through the gas-filled element, they change their charge state on average 100-1000 times per 1 m of travel in atomic collisions. Their trajectory within the dipole magnet will be determined by their average charge state $\overline{q}$. This average charge state is independent of the initial charge state and roughly proportionate to their velocity. It also depends on the ion's Z number and the atomic number and density of the gas in which the latter moves [40].

Let's assume that an ion of mass A, charge q and velocity v moves inside a homogeneous dipole-magnet field with flux density B in a radius of curvature ρ. The magnetic rigidity of this ion will be

$$B\rho = \frac{mv}{e\overline{q}}, \tag{3.6}$$

where mv is the momentum of the reaction product, $\overline{q}$ the average charge state and e the absolute value of the charge of the electron. N. Bohr in Ref. [41] predicted that all the electrons with orbital velocity smaller than v of the moving ion will be stripped, leading to an approximate average charge state of the ion $\overline{q}$, calculated by the Thomas-Fermi model of the atom, defined as

$$\overline{q} = \frac{v}{v_o}\mathrm{Z}^{1/3}, \tag{3.7}$$

for a velocity range $1 < v/v_o < \mathrm{Z}^{2/3}$, where $v_o = 2.19 \times 10^6$ m/s is the Bohr velocity. From Eqs. 3.6 and 3.7 the magnetic rigidity of the ion for non-relativistic mass is

$$B\rho = \frac{mv_o}{e\mathrm{Z}^{1/3}} = 0.0227\frac{\mathrm{A}}{\mathrm{Z}^{1/3}} \ \ Tm. \tag{3.8}$$

Eq. 3.8 provides a rough estimate of the separation properties of a gas-filled recoil separator. For symmetric reactions the magnetic rigidities of the evaporation residues, scattered target particles and the unreacted beam atoms give a ratio of 1:0.6:0.6, respectively. For asymmetric reactions the separation between the evaporation residues and the scattered target particles will be harder, but the unreacted beam atoms are much better separated than in symmetric reactions.

3.8 Compton Suppression

The high price of germanium detectors allows only a small size of crystal to be used experimentally. This results in many γ rays not being fully absorbed within the volume of the crystal contributing to the so-called Compton continuum, since this background is created from Compton scattered γ rays that have escaped the crystal. In order to compensate for this effect a BGO shield has been employed, i.e. BGO surrounding the Ge crystal. The scattered γ rays that escape the Ge crystal are detected in the BGO and these events are then rejected. The result is a higher peak-to-total ratio in the γ-ray spectrum, which is vital when the channel of interest is very weak or when the energy of interest overlaps energywise with a very high Compton continuum from other strong channels. The BGO shield is also called a Compton-suppression shield or escape-suppression shield.

3.9 Doppler Effects

In in-beam experiments the detection of γ rays suffers from two Doppler effects. One is the Doppler shift and the other is the Doppler broadening of the γ rays. The Doppler shift involves the difference in the measured γ-ray energy (E_{lab}) from its true energy (E_γ) according to the following equation

$$E_\gamma = E_{lab}\gamma(1 - \beta\cos\theta) = E_{lab}\frac{(1 - \beta\cos\theta)}{\sqrt{1-\beta^2}}, \tag{3.9}$$

where $\beta = v/c$ is the recoil velocity and θ is the detector angle with respect to the velocity vector of the recoils. The Doppler shift effect occurs due to the moving recoils, that lead to changes in the wavelength of the electromagnetic radiation. For small values of β, non-relativistic velocity ($\gamma \approx 1$), Eq. 3.9 can be simplified to

$$E_\gamma = E_{lab}(1 - \beta\cos\theta). \tag{3.10}$$

In order to compensate for the Doppler shift, the β value of the recoils must be calculated and Eq. 3.9 must be applied to the measured γ-ray energies.

In experimental situations where the angle of the outgoing recoil with respect to the beam axis (ϕ), as illustrated in Fig. 3.8, is not identified, the angle θ in Eq. 3.9 can be substituted by ω, given that the reaction kinematics focus the recoiling nuclei in a small forward cone, inducing only a minor error in the Doppler shift correction (small ϕ).

The Doppler broadening effect decreases the energy resolution of the detector and is due to its opening angle, inducing an uncertainty in the measured energy of

$$\Delta E_\gamma = E_{lab}\beta\sin\theta\Delta\theta, \tag{3.11}$$

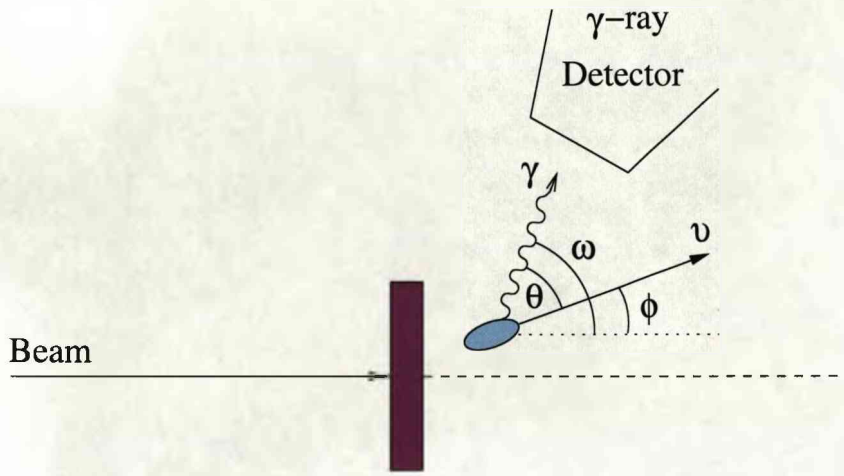

Figure 3.8: Emitted γ ray to an angle θ with respect to the velocity vector of the recoiling nucleus. The recoil is moving at an angle ϕ with respect to the beam axis.

where $\Delta\theta$ is the opening angle of the detector. The Doppler broadening is maximum for $\theta = 90°$ and also dominates for bigger γ-ray energies. The only way to compensate for this effect is by increasing the granularity of the detector, decreasing thus its opening angle.

3.10 The EXOGAM Array

The EXOGAM (EXOtic GAMma-ray) spectrometer is a European collaboration for the development of a high photopeak-efficiency and energy-resolution γ-ray spectrometer. It consists of segmented HPGe Clover detectors and is used for nuclear structure studies using RIBs at GANIL.

3.10.1 The Clover Detector

Composite HPGe detectors have been developed to overcome the challenges imposed by the Doppler broadening effects. These detectors consist of several HPGe crystals housed in the same cryostat, such that the photopeak efficiency will increase while the Doppler broadening effects will be compensated by the granularity of the detector.

The Clover detector, first developed for the EUROGAM phase II array [42], constitutes such a composite HPGe detector of four co-axial n-type Ge crystals packed together in the same cryostat and is shown in Fig. 3.9. The advantage of a big crystal without reducing the position resolution of the detector is thus obtained. Its name comes from its structure which is similar to a four leaf clover.

Technological advances have allowed the electrical segmentation of each HPGe crystal of the Clover detector (segmented Clover detector) leading to even better position resolution. This is achieved by segmenting the outer p-type contact of each HPGe crystal longitudinally to split it into four [44], giving separate readouts. The total number

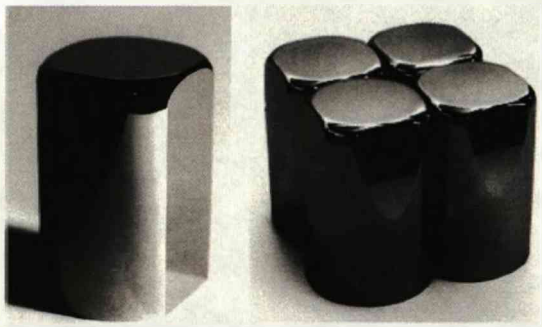

Figure 3.9: (Left) HPGe crystal from the EUROGAM Clover detector. (Right) Four HPGe crystals arranged in the Clover configuration. The picture is taken from Ref. [43].

of signals from a segmented Clover detector are 20, 4×4 for the four segments of each crystal plus four for the centre contact of each crystal.

3.10.2 The EXOGAM Clover Detector

The EXOGAM [45, 46] Clover detector consists of four segmented HPGe crystals separated by less than 0.5 mm; an EXOGAM Clover detector is illustrated in Fig. 3.10. Each crystal is processed from an initial 60 mm in diameter by 90 mm long crystal and tapered for 30 mm at the front with an angle of 22.5°; more details on the EXOGAM Clover design can be found in Ref. [47]. The centre contact signal is of high energy-resolution, while the outer contact signals are poorer in resolution. The EXOGAM Clover crystals have been manufactured by two different companies, ORTEC and CANBERRA EURISYS.

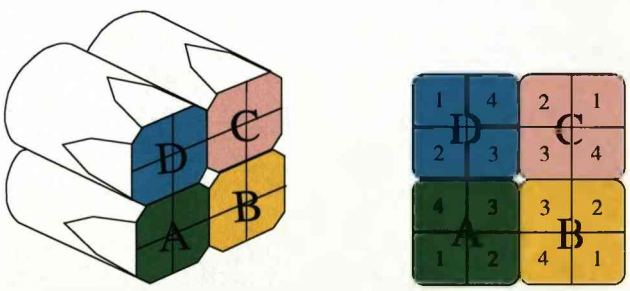

Figure 3.10: The EXOGAM Clover detector consists of four segmented HPGe crystals.

The EXOGAM Clover detector is surrounded by an escape-suppression shield comprised of individual building blocks of bismuth germanate (BGO) and CsI(Na)[1] scintillation detectors, i.e. the rear side shield (BGO), the side shield (BGO) and the back catcher (CsI(Na)), as illustrated in Fig. 3.11. The back catcher material was chosen instead of BGO for its lower cost. The energy of the γ rays that scatter in forward

[1]The choice of CsI(Na) as opposed to CsI(Tl) is related to the higher detection efficiency that CsI presents if it is doped with Na.

directions is large, as they deposit minimum energy in the HPGe detector, and thus larger thickness of suppression shield is needed for their detection. Although CsI(Na) has a lower stopping power than that of BGO, there is sufficient space at the back of the Clover for the use of this scintillator in a bigger size. The idea of several distinct elements comprising the suppression shield provides freedom for different configurations in EXOGAM. The suppression shield is operated in quadrants, i.e. the γ events that are vetoed should involve signals from a HPGe crystal and its adjacent shield element.

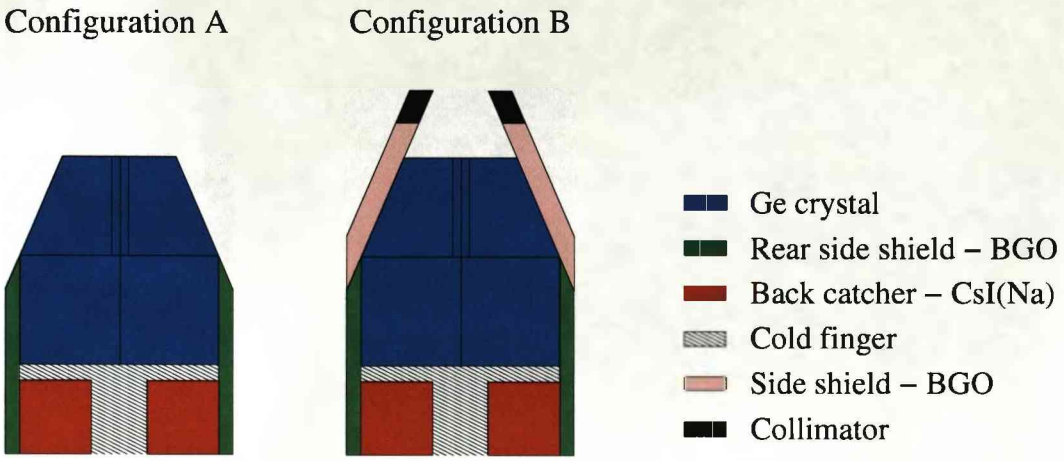

Figure 3.11: The two different suppression-shield configurations. The back catcher consists of CsI(Na) since its volume is big enough to provide sufficient suppression with lower cost comparing to BGO.

3.10.3 EXOGAM Configurations

The EXOGAM array consists of up to 16 segmented Clover detectors. The modularity of the suppression shield results in different configurations of the array,

1. configuration A, where the Clover detectors can essentially touch at the front, comprising thus a close-packed geometry and

2. configuration B, where the detectors are further away from the target to allow the inclusion of the side-suppression shield.

Table 3.1 summarises the characteristics of these configurations.

The "complete" geometry of the array consists of 16 Clover detectors positioned at 135° (four detectors), 90° (eight detectors) and 45° (four detectors) with respect to the beam direction. The "cube" geometry, consisting of four detectors, provides the minimum distance between the target and the detector face at $\sim$ 50 mm for configuration A.

Table 3.1: EXOGAM configurations for different geometries.

Geometry	Suppression-Shield Configuration	Distance to Target (mm)
Cube	A	50.3
Cube	B	68.3
Complete (16 detectors)	A	114.1
Complete (16 detectors)	B	147.4

3.10.4 EXOGAM Electronics

The EXOGAM electronics use the VXI (VME eXtension for Instrumentation) bus standard. Its modules consist of the following cards,

- ECC: for the centre contact information from the HPGe crystal,
- GOCCE: for the segment information,
- ESS: for the escape-suppression shield,
- Master Trigger: defines the condition to record an event,
- Resource Manager: to centralise the information from several cards,
- CENTRUM: allows the coupling of EXOGAM with additional detectors.

The data acquisition software used for EXOGAM is MIDAS [48].

3.11 The DIAMANT Charged-Particle Array

The DIAMANT array, as implemented for this work, is illustrated in Fig. 3.12 and constitutes a light charged-particle (proton, α, etc.) detector array of CsI(Tl) scintillators, that is coupled to the EXOGAM spectrometer and is used for channel selection by identifying emitted charged-particles from the fusion-evaporation exit channels. It consists of 48 CsI(Tl) 3 mm thick scintillator detectors coupled optically to PIN photodiodes by plexiglas light guides, covering an almost 2π solid angle, from 8° to 90° with respect to the beam axis. The selected forward-focused geometry is due to the high absorption efficiency of low energy (< 400 keV) γ rays that CsI presents, so that the DIAMANT elements will not cover the EXOGAM Clover detectors, situated at backward angles.

For each element of DIAMANT, three types of signals are derived: the energy of the particle, its type (particle identification: PID) and a time-reference signal related to

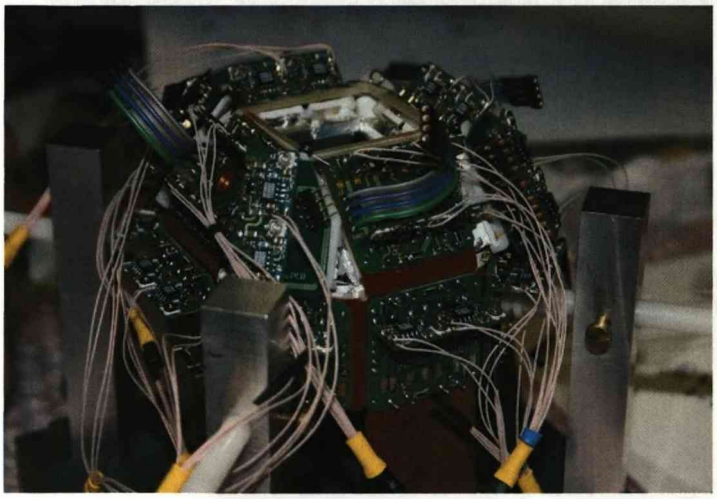

Figure 3.12: The DIAMANT charged-particle array.

the time instance of the particle-γ coincidence. In order to acquire this information, the signal from the charge-sensitive preamplifier is processed with its amplitude giving the energy of the particle, its rise time the particle identification and the time of arrival the time reference signal [49]. The particle identification plot obtained by DIAMANT can be seen in Fig. 3.13. The particle identification is obtained by pulse shape discrimination techniques applied on the time response of the scintillator as mentioned in Section 3.4.2.

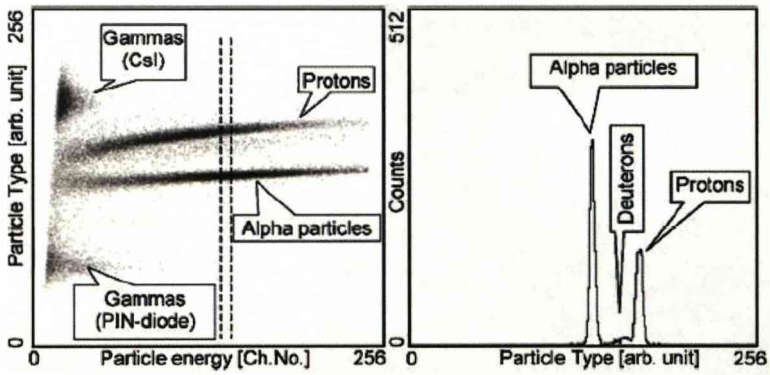

Figure 3.13: Left: Scatter plot of *Particle-Type* vs. *Energy spectrum* with intensities indicated by a grey-scale. Right: *Particle-Type* spectrum for the narrow *Energy* slice corresponding to channels 150-160 showing alpha, deuteron and proton peaks. The spectra are taken from Ref. [49].

The VXI standard was used for DIAMANT. DIAMANT is not integrated in the Master Trigger of the acquisition system, but acts as a "slave" to EXOGAM, i.e. its signals are written in the event only if the Master Trigger is satisfied.

3.12 The VAMOS Spectrometer

The low intensity of RIBs provided by the SPIRAL facility at GANIL and the study of nearly or completely unknown nuclei over a wide range of masses and energies need a highly efficient detection system. The VAriable MOde Spectrometer (VAMOS) [50] is of high acceptance and designed to identify reaction products induced by SPIRAL beams.

The VAMOS spectrometer is illustrated in Fig. 3.14. It consists of two magnetic quadrupoles (the first quadrupole focuses the beam in the y-direction, i.e. perpendicular to the plane of dispersion, whereas the second quadrupole focuses it in the x-direction, i.e. in the dispersion plane), one Wien filter (velocity filter that deflects the ions horizontally, providing the A/Q dispersion), one magnetic dipole (variable deflection angle from 0° to 60°) and the focal plane, consisting of two secondary-emission-electrons detectors ($x - y$ and time measurement, SED detection system), an ionisation chamber (E, ΔE measurement) and a plastic scintillator. The focal plane of VAMOS can consist of two different combinations of elements depending on the type of the beam. For fast and light ions two drift chambers are used followed by an ionisation chamber and a plastic scintillator. For slow and heavy nuclei the drift chambers are replaced by two detectors of the secondary emission electrons (SED detection system).

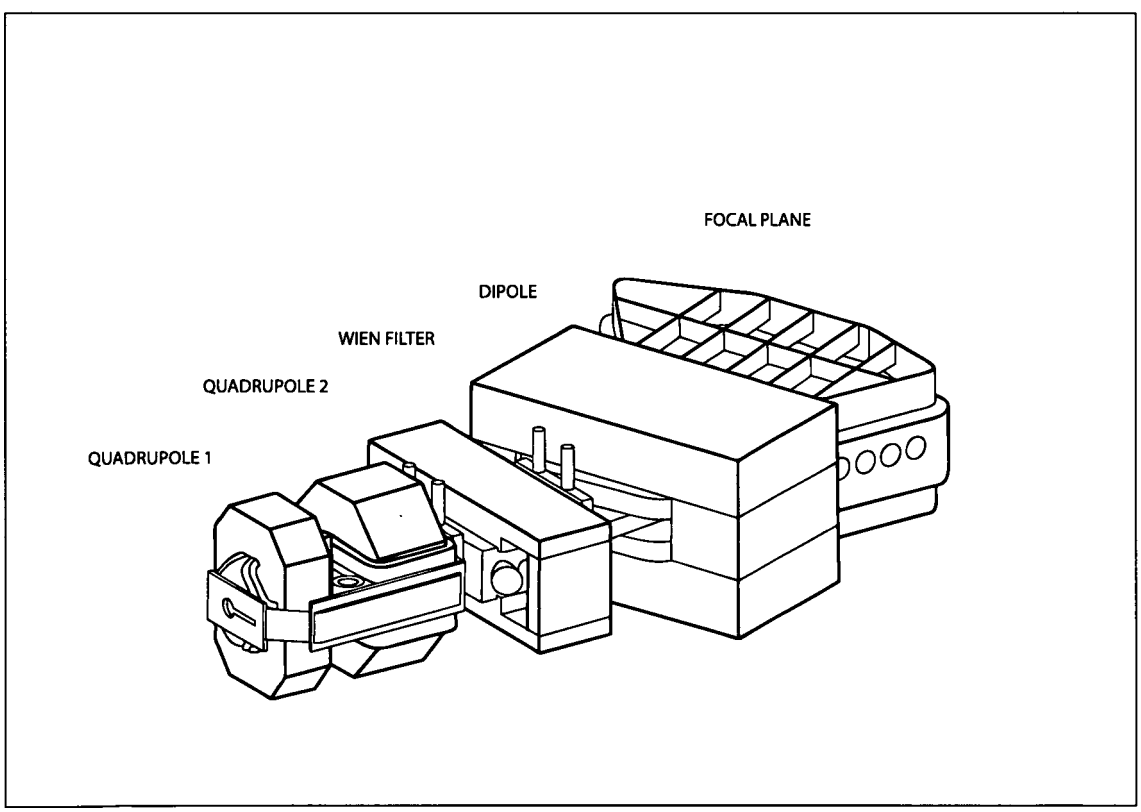

Figure 3.14: The VAMOS spectrometer.

3.13 The JUROGAM γ-ray Spectrometer

The JUROGAM array comprises a powerful γ-ray detector which consists of 43 (9 GASP-type detectors [51] and 34 EUROGAM Phase-I type (Fig. 3.15) [52]) Compton-suppressed HPGe detectors. The 43 Ge crystals of JUROGAM are placed into six different angles with respect to the beam axis according to Table 3.2. Heavy-metal collimators are used at the front of each detector in order to prevent false signalling of scattered events from γ rays that come directly from the target position.

Table 3.2: Detector number according to rings of JUROGAM.

Ring	Ge	θ
1	1-5	157.60°
2	6-15	133.57°
3	16-25	107.94°
4	26-30	94.16°
5	31-35	85.84°
6	36-45	72.05°

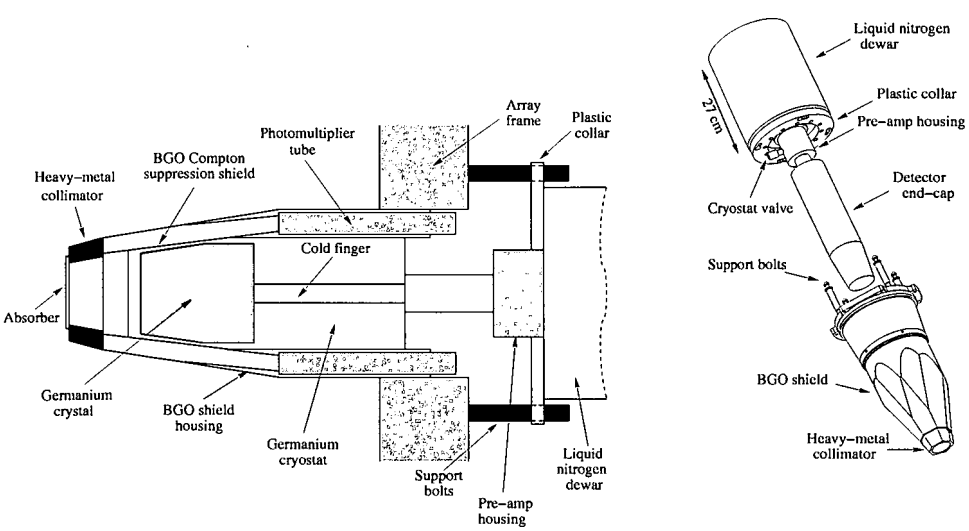

Figure 3.15: Technical drawing of a EUROGAM Phase-I detector module [53]. The picture is taken from Ref. [54].

3.14 The RITU Gas-Filled In-Flight Recoil Separator

The RITU (Recoil Ion Transportation Unit) [55, 56] gas-filled recoil separator has a magnetic configuration of QDQQ, where Q stands for magnetic quadrupole and D for magnetic dipole, and is shown in Fig. 3.16. The first and third quadrupoles provide vertical focusing while the second focuses the particles horizontally. Normally, the basic configuration of a separator is DQQ, the dispersive element in other words is immediately downstream from the target in order to reduce the beam-like particles from the background in the focal plane. But in RITU, in order to increase the angular acceptance of the dipole, there is a vertically focusing quadrupole just before the dipole. The parameter values of RITU are presented in Ref. [57].

The He gas pressure was set to 0.6 mbar for this experiment, as this pressure value gave an optimum distribution of the reaction products at the focal plane of RITU. The separation time was of the order of 500 ns. Although in principle the original state of the ions entering the dipole magnet does not affect their separation through RITU, it is observed that a charge reset foil before the dipole provides the needed equilibrium charge state for more efficient separation.

Use of Reset Charge State Carbon Foil

The de-excitation of a nuclear state can be performed via two different mechanisms, a γ-ray emission or an internal electron conversion. In the latter case an inner-shell electron is emitted leaving a vacancy, which will be filled by an outer electron leading to the emission of an X ray or an Auger electron. This process changes significantly the mean charge state of the recoiling residues from a fusion reaction [58]. In order to produce an equilibrium charge state distribution for the residues, a thin carbon reset foil is placed directly after the target. This way the transmission through RITU is optimum.

3.15 The GREAT Spectrometer

The GREAT (Gamma Recoil Electron Alpha Tagging) spectrometer comprises a state-of-the-art implantation detection system and is presently used as the focal-plane detector of the RITU gas-filled recoil separator. GREAT is designed to detect protons, α and β particles, conversion electrons, X rays and γ rays and it can be used for decay studies (stand-alone mode) or as a tagging device in order to perform γ-ray spectroscopy at the target position of RITU.

The GREAT spectrometer consists of the following detection systems [59], illustrated in Fig. 3.17:

1. A MWPC (Multi Wire Proportional Counter), which gives timing, position and energy loss information of the ions passing through it.

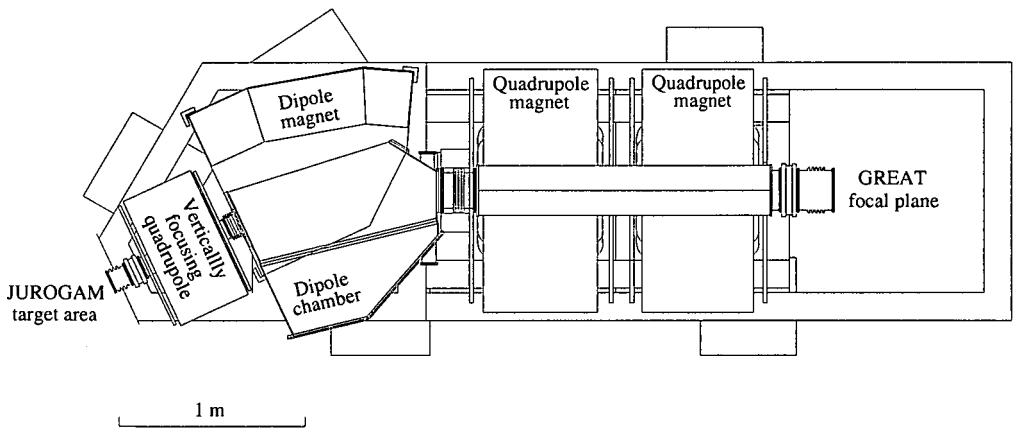

Figure 3.16: The RITU gas-filled recoil separator. The picture is taken from Ref. [54].

2. A DSSD (Double Sided Si Strip Detector), where all the ions that manage to "survive" through RITU are implanted.

3. An array of 28 silicon PIN diodes, which is mounted in a box arrangement around the perimeter of the DSSDs. The PINs allow the detection of conversion electrons and escaped protons or α particles from the implantation detector.

4. A planar double-sided Ge strip detector, which is mounted directly behind the DSSDs. This detector has been designed for GREAT in order to measure X rays and low-energy γ rays.

5. A Clover Ge detector, which is designed to measure higher energy γ rays.

In the present experiment the GREAT spectrometer is used to give a valid tag for the identification of the nucleus of interest. For this reason only the DSSD and the MWPC are used in great extent. Thus, there is a more detailed description for the implantation and gas detector in the following sections.

3.15.1 The Double Sided Silicon Strip Detector of GREAT

The DSSD measures the energy of the implanted recoils and of their subsequent decays. It consists of two adjacent DSSDs. Each DSSD has an active area of 60 mm $\times$ 40 mm and a strip pitch of 1 mm in both directions, giving a total of 2400 pixels for each DSSD and 4800 pixels for the whole implantation detector. The thickness of the DSSD is 300 μm. The recoil-collection efficiency of the DSSD is $\approx$ 85% [59].

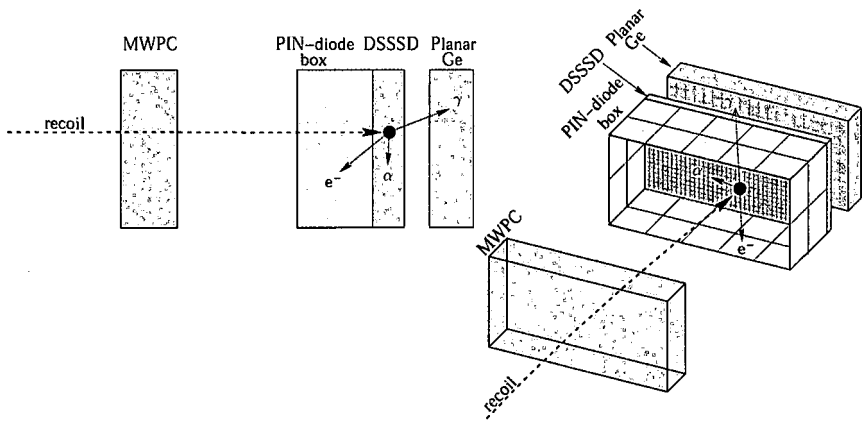

Figure 3.17: Schematic drawing of the GREAT focal plane and its detection mechanism. The picture is taken from Ref. [54]. The Clover Ge detector (not visible here) is positioned either on top or behind the planar Ge detector.

In experiments with near Coulomb barrier beam energies, the recoils from fusion-evaporation exit channels are fully absorbed in the silicon detectors within a few μm (1-10 μm depending on the characteristics of the specific experiment) [60]. However, thin degraders (e.g. mylar foils) can be used in front of the DSSD in order to reduce the energy of the implanted recoils as well as the energy of the scattered beam.

In this experiment the populated nuclei lie close to the drip line. These nuclei decay via β emission to more stable isotopes. Beta particles with an end-point energy of a few MeV deposit part of their energy in the silicon detector. This deposition depends on the direction of the particle and the multiplicity of the scattering within the detector. A β particle which impinges on the 300 μm silicon detector in the forward direction and which has an end-point energy of a few MeV deposits an energy of the order of $\sim$ 100 keV, while those with complex trajectories in the DSSD (due to multiple scattering) result in a tail at higher energies [60]. The lower part of the energy deposition is usually cut by the threshold imposed on the silicon detectors for energies smaller than typically 50 keV.

3.15.2 The Multi Wire Proportional Counter of GREAT

The multiwire proportional counter (MWPC) is positioned at the entrance of GREAT and has an aperture of 131 mm $\times$ 50 mm. Two mylar foils are placed at the entrance and exit windows, in order to separate the isobutane of the gas chamber from the He gas of RITU and the vacuum of GREAT, respectively. The MWPC consists of four cathode planes and an anode wire plane and has two functions. One is to signal a recoil implantation or a decay in the DSSD via the coincidence or anti-coincidence mode, respectively. Moreover, it is possible to distinguish between a recoil event or a primary beam ion on a E-ΔE basis in conjunction with the energy information from

the implantation detector.

3.16 The Total Data Readout Acquisition System

The Total Data Readout (TDR) acquisition system [61] has been developed for the GREAT spectrometer in order to compensate for the dead time losses induced by an RDT experiment. So far, in-beam experiments that implement a tagging technique used a common hardware trigger and all the detectors' signals were recorded using delayed coincidences. This technique induces dead time losses, as the system remains "frozen" until the time gate for the event has been met. The TDR is a triggerless system where all channels run independently, thus reducing the dead time into the individual signal processing dead time, which is of the order of 10 μs.

In Fig. 3.18 a schematic diagram of the TDR system is illustrated. All the signals from the NIM/CAMAC front-end electronic units are fed into the VXI Analog-to-Digital Converter (ADC) cards, where the time-stamping takes place from a global 100 MHz clock to an accuracy of 10 ns. To ensure the synchronisation, every 655 μs the metronome sends a sync pulse to the data. Via SHARC links the data streams are sent to the two collators where they are put in time order. The two time-ordered data streams are then fed into the merger where the output is one time-ordered stream of data. This time-ordered data stream is fed into the event builder via Gbit ethernet, where temporal and spatial information are applied in order to "decide" which data are stored. A typical software trigger in the event builder for an RDT experiment involves the data signalled by any focal-plane detector plus data from the target position detector for 5 μs delayed time from any MWPC or DSSD signal.

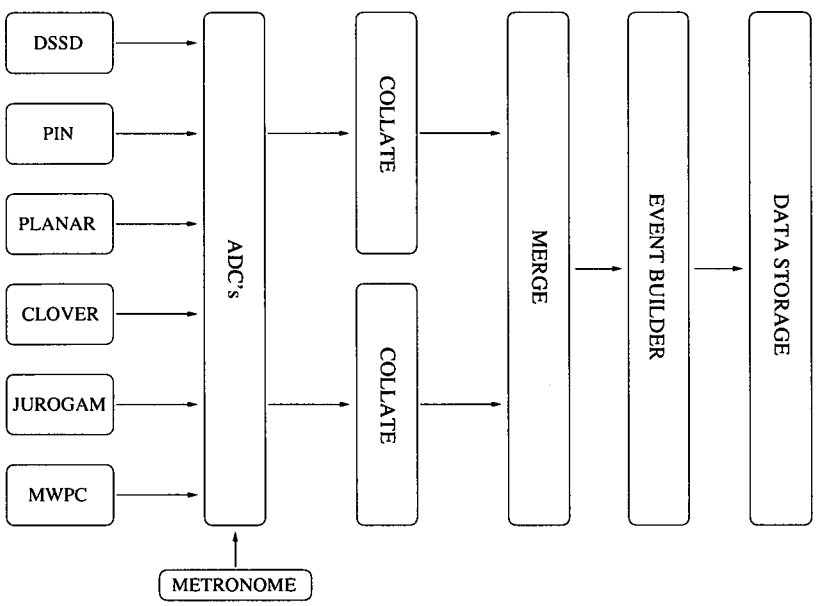

Figure 3.18: The TDR acquisition system.

3.17 The GRAIN Analysis Package

The data stored through the TDR system consist of time-ordered data streams that need a software trigger in order to construct an event. This software trigger is provided via the GRAIN analysis package [62]. In the present experiment the software trigger is the OR(DSSD) gate with a trigger delay of 1 μs and a trigger width of 2 μs. This analysis program is based on JAVA and provides, apart from the event parser, a really useful and powerful sort engine.

Chapter 4

Probing the Maximally Deformed Light Rare-Earth Region around the Drip-Line Nucleus ^{130}Sm

Proton drip-line nuclei provide an important basis for the understanding of fundamental nuclear interactions and the determination of the limits of nuclear stability. In particular, proton-rich rare-earth nuclei of the A $\sim$ 130 region, as shown in Fig. 4.1, are of particular interest since highly deformed prolate ground states are expected. Indeed these nuclei, with neutron numbers lying midway between the N = 50 and N = 82 shell closures and proton numbers far away from the Z = 50 shell closure, are predicted to show maximal ground-state quadrupole deformations of $\beta_2 \sim 0.4$ [1]. This value of β_2 corresponds to a prolate nuclear shape with a 3:2 axis ratio and is comparable to that deduced for superdeformed bands observed in cerium isotopes at high spin, allowing some very interesting comparisons to be made.

Mapping and understanding major regions of deformation away from closed-shells is an important aspect of nuclear structure physics. Experiments have succeeded in studying the nuclei approaching, but not yet reaching, the peak of this deformation. The use of RIBs opens up this exotic region of nuclei and allows the probing of nuclei around the peak of this systematic feature.

The present experiment aimed to study the predicted lightest proton-bound samarium isotope ^{130}Sm, the first excited state of which has been documented in Ref. [5], and the completely unknown ^{131}Sm and ^{130}Pm isotopes via the fusion-evaporation reaction $^{58}_{28}$Ni + $^{76}_{36}$Kr and the exit channels 2p2nγ, 2pnγ and 3pnγ, respectively. From theoretical calculations a large ground-state deformation has been predicted for ^{130}Sm with values of $\beta_2 \sim 0.40$ and $\gamma \sim 0°$. Experimentally the deformation trend of the even-even samarium isotopes can be observed by examining the energy of the first 2^+ state; the lower the 2^+ energy, the larger is the β_2 value. Moreover, the ratio of the 4^+ and 2^+ energy levels, $E(4^+)/E(2^+)$, of an even-even nucleus can yield the type of its collective excitation; if $E(4^+)/E(2^+) = 2$ then the nucleus is a perfect vibrator, while

if $E(4^+)/E(2^+) = 3.33$ the nucleus is a perfect rotor. In Fig. 4.2 the energy systematics [6] of the lightest samarium isotopes are presented, where it is evident that the ground-state deformation is increasing for decreasing neutron number. Furthermore, their $E(4^+)/E(2^+)$ ratios show that these isotopes move towards the perfect rotor limit as neutrons are removed.

The present experiment, being the first of its kind, faced many technical problems, i.e. the VAMOS spectrometer failed during the second half of the experiment due to a vacuum problem. This in combination with the low production cross sections of the exit channels of interest and the high radioactive background from the ^{76}Kr beam precluded the identification of any transitions depopulating the nuclei of interest (^{130,131}Sm and ^{130}Pm). However, the present experiment was pioneering in probing proton drip-line nuclei with RIBs using a state-of-the-art experimental setup. Thus, the experimental challenges and achievements of the in-beam spectroscopy of proton drip-line nuclei are presented in this chapter.

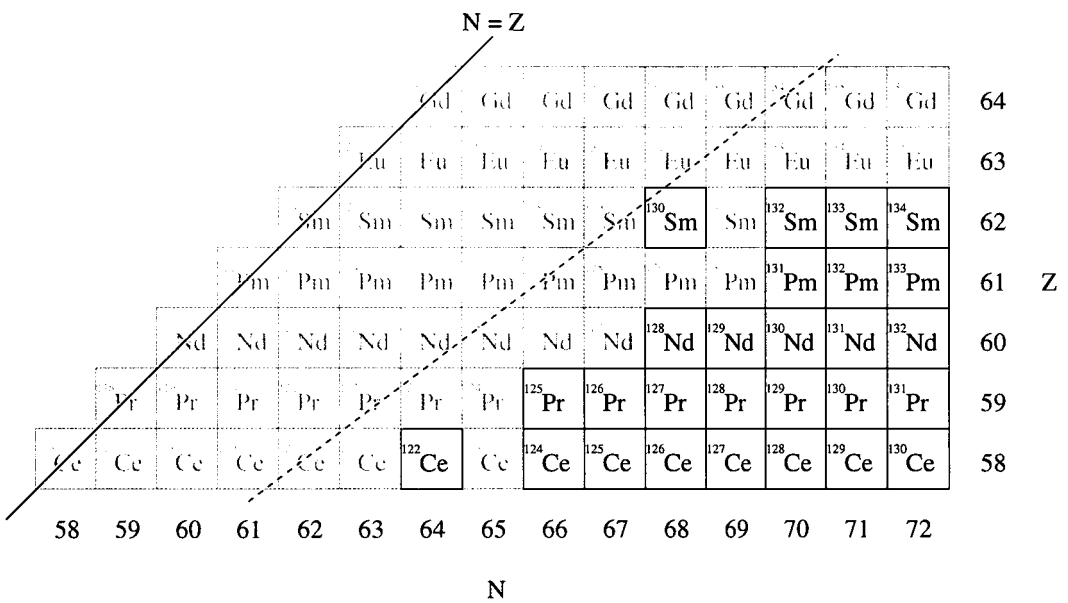

Figure 4.1: A $\sim$ 130 mass region. The highlighted-black isotopes correspond to nuclei with known excited states. The dashed line represents the approximate proton drip line as calculated from microscopic Hartree-Fock-Bogoliubov calculations [63], while the N = Z line is also shown.

4.1 In-Beam Studies using RIBs

The discovery of new exciting phenomena as well as the exploration of unknown territories on the Segré chart of the nuclei have led to the investment of money, effort and time for the development of RIBs. However, the use of RIBs induces several experimental challenges, demanding the development of new spectrometers and the coupling

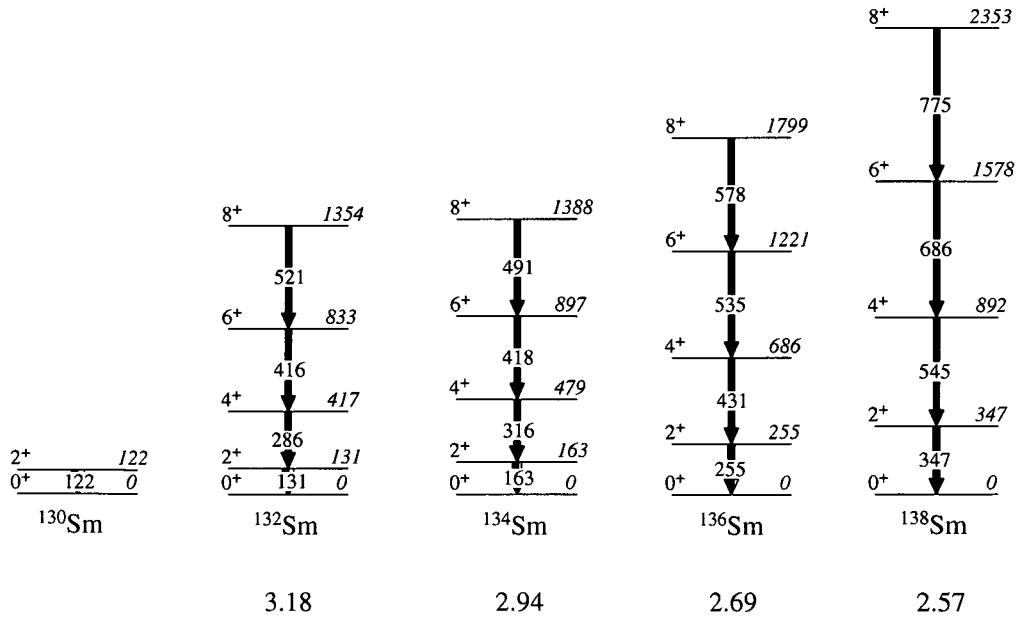

Figure 4.2: Excitation-energy systematics of the ground-state rotational bands of the even-even samarium isotopes with $130 \leq A \leq 138$. The numbers below each band show the $E(4^+)/E(2^+)$ ratios.

of many complex detection systems. This is due to the low intensity of the RIBs, which requires highly efficient spectrometers for the observation of the nuclei of interest, produced with low cross sections. Moreover, the highly induced background due to the radioactive decay of the beam necessitates the use of a highly selective detection system, which can be achieved by the coupling of many detectors. Finally, the γ-ray spectrometers should present high granularity in order to compensate for the increased Doppler-broadening effects when using inverse kinematics and close-packed geometries for greater photopeak efficiency.

4.2 Experimental Details

The experiment was carried out at GANIL, France, where the SPIRAL facility delivered a ^{76}Kr RIB at an energy of 4.34 MeV/u and with an average intensity of 5×10^5 particles per second. The RIB impinged on a target consisting of 1.1 mg/cm^2 of ^{58}Ni on a thin carbon foil. The irradiation time was around seven days. The detection system consisted of the EXOGAM γ-ray spectrometer coupled together with the DIAMANT charged-particle array and the VAMOS recoil spectrometer.

In the present experiment EXOGAM consisted of 11 HPGe Clover detectors, with seven located at 90° and four at 135° with respect to the beam axis, as shown in Fig. 4.3. The detectors were positioned at $\sim$ 114 mm from the target position (suppression-shield configuration A: the rear side shield (BGO), the back catcher (CsI(Na)) and no side

shield suppression is used [64]), where they can essentially touch at the front in order to comprise a close-packed geometry and thus increase the photopeak efficiency of the array.

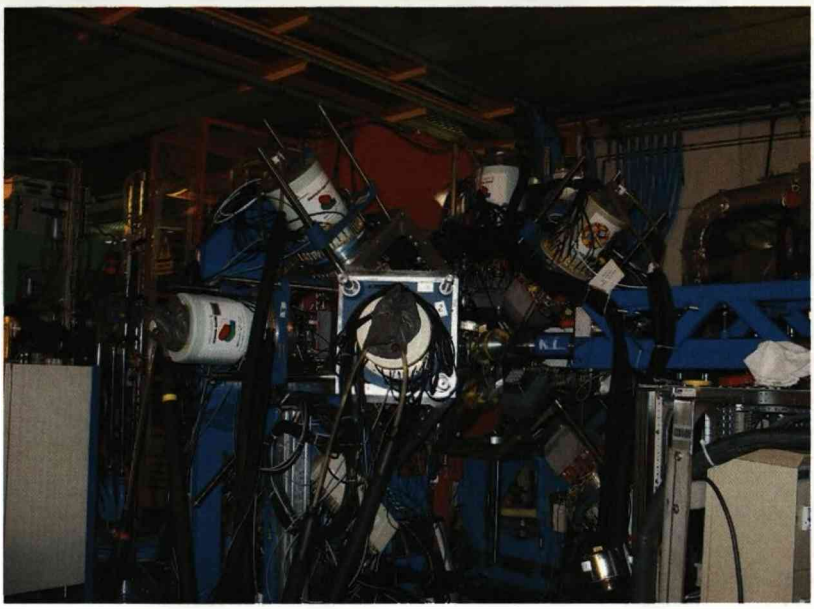

Figure 4.3: The EXOGAM array as implemented in the present experiment.

The DIAMANT array, comprising of 48 CsI(Tl) scintillators, provided channel selection by identifying light charged particles emitted from the compound system (^{134}Gd*), as described in Section 3.11. DIAMANT was mounted inside the target chamber with an almost 2π close-packed geometry covering forward angles with respect to the beam axis, from 8° to 90°.

The VAriable MOde Spectrometer (VAMOS) [50] is designed to identify reaction products induced by SPIRAL beams, since nearly or completely unknown nuclei are populated. Unfortunately, several technical problems during the experiment, as mentioned in the introduction of this chapter, precluded its use in the data analysis.

4.2.1 The ^{76}Kr Beam

The radioactive $^{76}_{36}Kr^{11+}$ beam was produced via the fragmentation of a 68.5 MeV/u beam of $^{78}_{36}$Kr of 5×10^{11} particles per second intensity onto the production target. The CIME cyclotron and the α spectrometer of the SPIRAL facility delivered the $^{76}_{36}Kr^{11+}$ beam at an energy of 330 MeV (4.34 MeV/u) and with an average intensity of 5×10^5 particles per second. The ^{76}Kr beam decays via electron capture (EC) and β^+ emission to ^{76}Br and finally to the stable ^{76}Se nuclide [65],

$$^{76}\text{Kr}\ (t_{1/2}=14.8\ \text{h}) \xrightarrow{\beta^+,\text{EC}} {}^{76}\text{Br}\ (t_{1/2}=16.2\ \text{h}) \xrightarrow{\beta^+,\text{EC}} {}^{76}\text{Se (stable)}.$$

4.3 Results

The trigger condition used in the present experiment required an EXOGAM $\gamma-\gamma$ event or an EXOGAM − VAMOS event. DIAMANT constituted a subset of EXOGAM and its signals, if any, were stored whenever this trigger was satisfied. The data collected were merged using the GANIL CENTRUM[1] electronic module [66], providing time-stamped events before being written to tape for further off-line analysis. A total of approximately 10^9 such events were recorded. Their corresponding singles γ-ray spectrum is shown in Fig. 4.4(a). This spectrum is dominated by the radioactivity of the ^{76}Kr beam. The strongest peaks are the 511 keV annihilation peak and the 559 keV and 657 keV γ rays from the $2_1^+ \rightarrow 0^+$ and $2_2^+ \rightarrow 2_1^+$ transitions in ^{76}Se, respectively.

The fusion-evaporation reaction produced recoiling residues ($v = 0.047c$), which resulted in a Doppler shift and broadening of the detected γ rays. In order to correct for this, the angle of the HPGe crystal/segment with respect to the beam direction is required. In Fig. 4.5 the sideview of an EXOGAM Clover detector is illustrated. Although its position with respect to the beam axis is at 90°, the crystals/segments have a slightly different angle. For the Doppler correction one needs to define this angle, which depends on the interaction depth of the γ rays in the crystals/segments.

The low-energy γ rays of interest ($E_\gamma < 800$ keV) interact with the material of the HPGe crystal within its first few centimetres. In Ref. [44] measurements on a prototype segmented Clover detector for the definition of this interaction depth are presented. Its optimum value for γ rays of energy up to $\sim$ 600 keV has been deduced at $\sim$ 30 mm. In the present experiment slight changes to the interaction depth around this value did not significantly alter the resolution of the γ-ray peaks. Thus the crystal/segment angles that were derived using the EXOGAM design of Fig. 4.5 have been deduced assuming an interaction depth of 30 mm and are summarised in Table 4.1.

The γ-ray singles spectrum that is Doppler corrected according to the four HPGe crystals of each Clover is shown in Fig. 4.4(b). The background radioactivity peaks from the decay of the ^{76}Kr beam are split into four, since they are emitted from non-moving beam-like particles built up in material at and around the target position. In contrast, γ rays that are emitted from the moving fusion-evaporation products should now be aligned.

[1] Clock Event Number Transmitter Receiver Universal Module

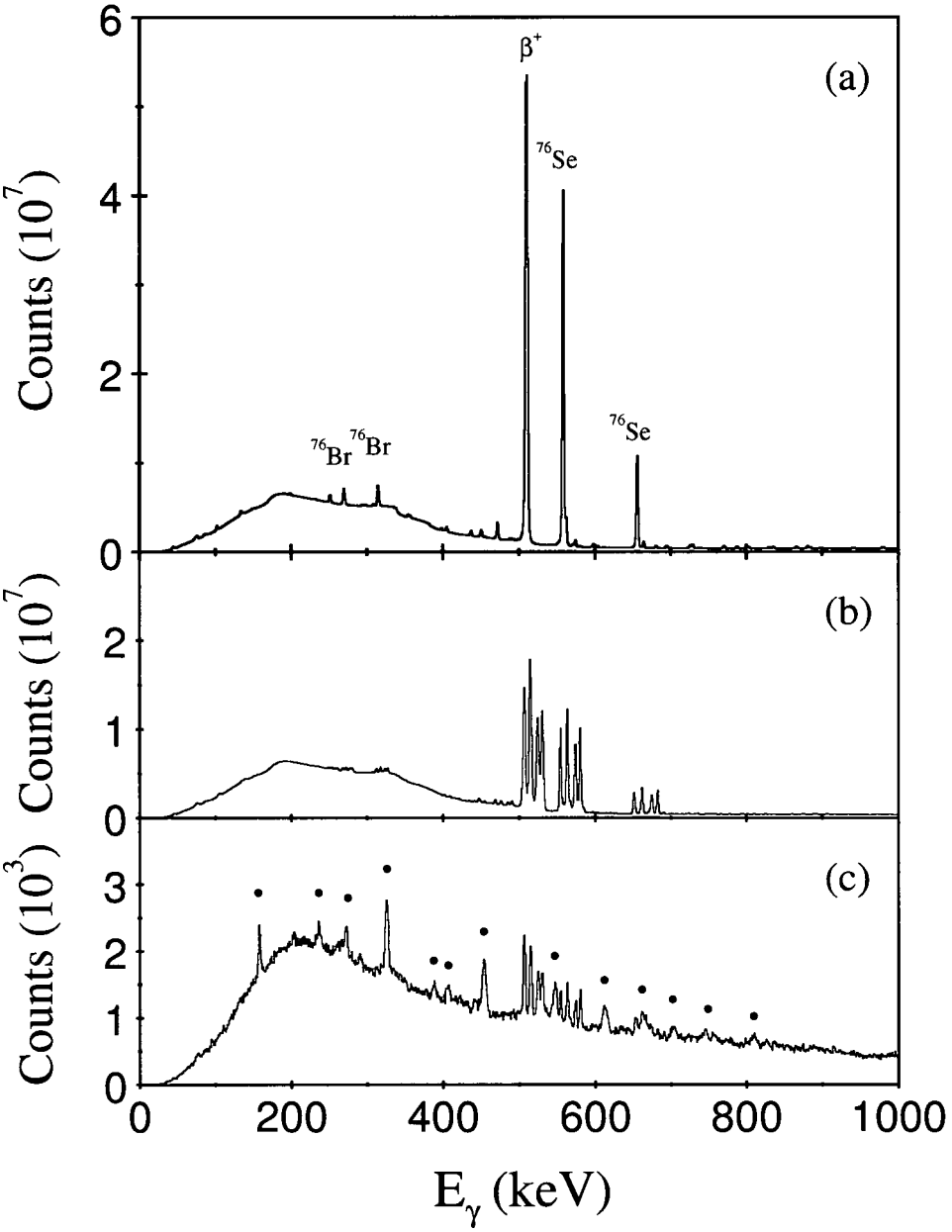

Figure 4.4: (a) Total γ-ray spectrum (1 keV/channel). The labelled peaks correspond to the 511 keV annihilation peak, as well as to transitions depopulating excited states in ^{76}Br and ^{76}Se. (b) Total Doppler-corrected γ-ray spectrum (1 keV/channel). The background radioactivity peaks split into four, according to the four angles of the HPGe crystals with respect to which the γ rays are Doppler corrected. (c) Doppler-corrected γ-ray spectrum (1 keV/channel) in coincidence with at least one charged particle identified by DIAMANT. These events constitute only $\sim$ 0.04% of the total number of events recorded during the experiment. Gamma rays from fusion products are now evident, labelled by solid circles.

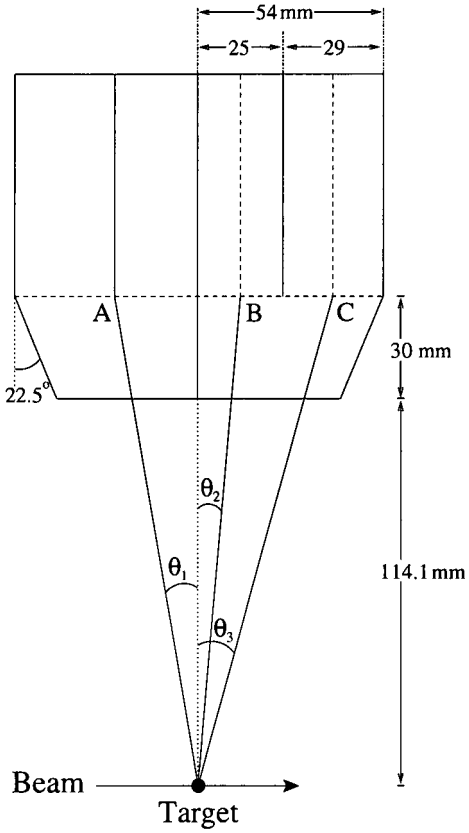

Figure 4.5: Sideview of an EXOGAM Clover detector positioned at 90° with respect to the beam axis and centred at 114 mm from the target position. For an interaction depth of 30 mm at point A, the deviation from 90° of the crystal angle is $\theta_1 = 9.8°$. For an interaction depth of 30 mm at points B and C, the deviation from 90° of the segment angles is $\theta_2 = 5.0°$ and $\theta_3 = 15.3°$, respectively. Assuming that the recoiling nuclei travel along the beam direction, the crystal angle that should be used for the Doppler correction is $90° + \theta_1$, while the segment angle is $90° - \theta_{2,3}$.

Table 4.1: Defined angles for the EXOGAM crystals and segments considering an interaction depth of 30 mm. For this calculation the EXOGAM design illustrated in Fig. 4.5 is used, where the θ_1, θ_2 and θ_3 angles are introduced.

Clover angle	Crystal angle	Segment angle
90°	$90° - \theta_1 = 80.2°$	$90° - \theta_2 = 85.0°$
		$90° - \theta_3 = 74.7°$
	$90° + \theta_1 = 99.8°$	$90° + \theta_2 = 95.0°$
		$90° + \theta_3 = 105.3°$
135°	$135° - \theta_1 = 125.2°$	$135° - \theta_2 = 130.0°$
		$135° - \theta_3 = 119.7°$
	$135° + \theta_1 = 144.8°$	$135° + \theta_2 = 140.0°$
		$135° + \theta_3 = 150.3°$

4.3.1 DIAMANT Gates

DIAMANT provided the charged-particle identification of the evaporation channels. As mentioned in Section 3.11, for each element of DIAMANT three types of signal are derived: the energy of the particle, its type (particle identification: PID) and a time-reference signal related to the time instance of the particle-γ coincidence [49]. The two-dimensional plot of the energy versus the particle identification signal (PID matrix), shown in Fig. 4.6(b), provides characteristic distinct patterns for each type of charged particle and the γ rays detected by the CsI and the PIN diodes. An energy calibration thus was not necessary. Before applying the two-dimensional gates on the detected protons and alphas, in order to suppress uncorrelated background events in DIAMANT, i.e. events that trigger DIAMANT but do not correspond to a prompt γ-particle coincidence, the timing information is extracted (Fig. 4.6(a)). The true coincidences between a fusion-evaporation charged particle and a γ ray in EXOGAM comprises a small fraction of the events signalled by DIAMANT (Fig. 4.6(c)). The PID matrix that corresponds to these events is shown in Fig. 4.6(d); the two cuts select the detected fusion-evaporation protons and alphas and their distribution is shown in Fig. 4.7.

Considering the condition of emitted γ rays in coincidence with at least one charged particle in DIAMANT, i.e. pure fusion-evaporation events, the spectrum in Fig. 4.4(c) is obtained. These events constitute only a small fraction $\sim 0.04\%$ of the total number of events recorded during the experiment (Figs. 4.4(a) and (b)). It is evident that by gating on the charged particles detected by DIAMANT, most of the background radioactivity in the γ-ray spectra disappears, as seen also in Fig. 4.8, where the Ge Constant Fraction Discriminator (CFD) time versus the γ-ray energy is plotted with and without any gates applied in DIAMANT. The background radioactivity peaks are evident in Fig. 4.8(a), while they are suppressed after a selective DIAMANT gate has been applied, as seen in Fig. 4.8(b).

The almost 2π solid angle coverage of DIAMANT reduces its absolute detection efficiency; however, this configuration was chosen to allow low-energy γ rays to be detected by EXOGAM, which covers backwards angles, without significant absorption. Unfortunately, this results in the "contamination" of the charged-particle gated γ-ray spectra from exit channels with a greater number of particles emitted than that required by the gate, i.e. γ rays from the 3p and 4p exit channels will be visible in the 2p gated spectrum, as seen in Fig. 4.9. Using such "contamination" peaks, the proton detection efficiency of DIAMANT has been calculated at $\varepsilon_p = 47(2)\%$ for this experiment, as described in the following section.

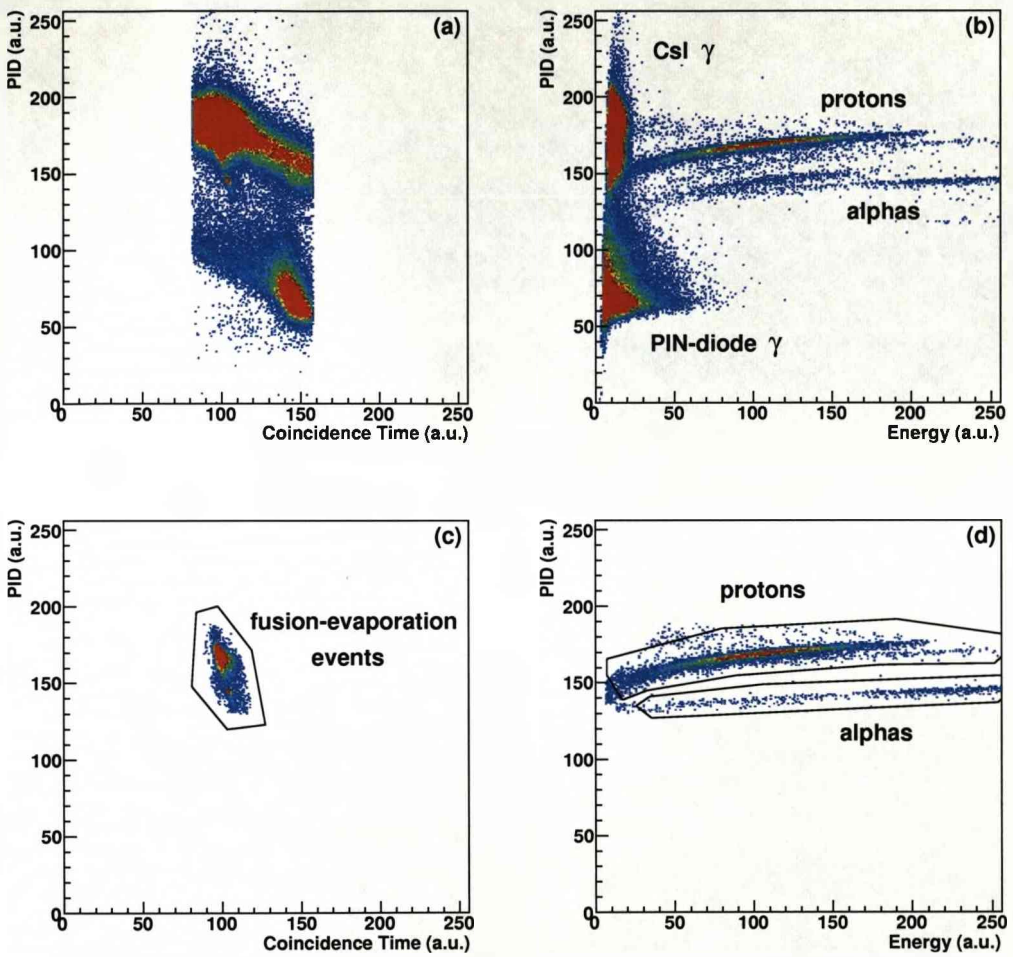

Figure 4.6: (a) Time of coincidence versus PID. (b) PID matrix. (c) Time of coincidence versus PID for the prompt γ-particle coincidences. (d) Particle identification matrix, gated by the fusion-events cut of plot (c). All the uncorrelated events plus the γ rays detected by the CsI and the PIN diodes are suppressed. The two distinct patterns correspond to the protons and the alphas of the fusion exit channels. The applied gates can be seen.

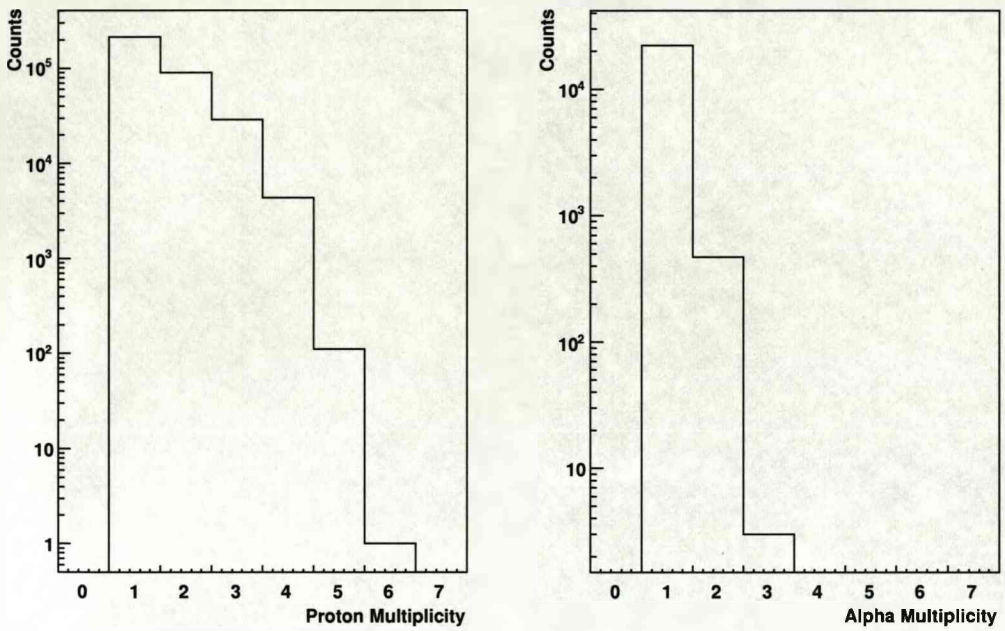

Figure 4.7: Proton and alpha-particle distribution in DIAMANT.

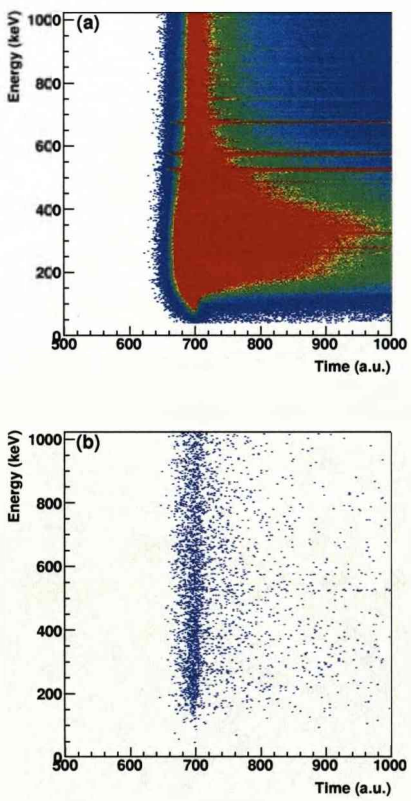

Figure 4.8: Characteristic spectrum of the Ge CFD (Constant Fraction Discriminator) time versus the γ-ray energy (a) without any gates on DIAMANT and (b) in coincidence with at least one proton emission. Almost all the background radioactivity is suppressed after the applied DIAMANT gates.

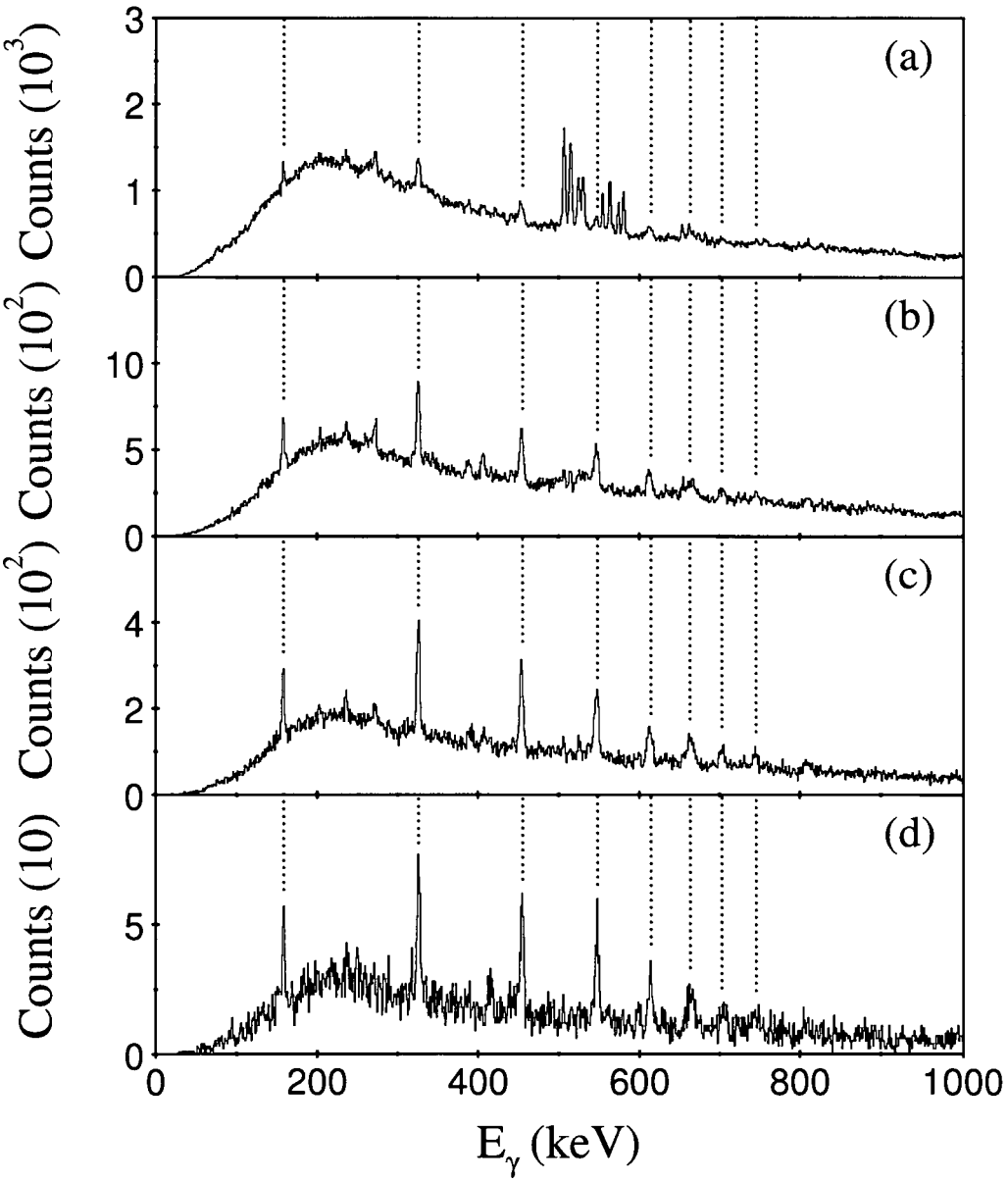

Figure 4.9: Doppler-corrected γ-ray spectra (1 keV/channel) in coincidence with (a) one-proton emission, (b) two-proton emission, (c) three-proton emission and (d) four-proton emission. The dotted lines indicate transitions in the strongest four-proton exit channel (^{130}Nd).

Detection Efficiency of DIAMANT

In the case of 100% detection efficiency in DIAMANT the γ rays that depopulate transitions in the 4p exit channel (^{130}Nd) should not be visible in the 1p, 2p and 3p gated spectra of Figs. 4.9(a), (b) and (c).

Let's assume that the proton detection efficiency of DIAMANT is ε. Following the different branches of the binary tree of Fig. 4.10, the probability of detecting zero, one, two, three and four protons are presented in Table 4.2. These probabilities should be reflected in the intensity of a γ-ray transition, i.e. the ratio of the intensity of a γ ray that corresponds to ^{130}Nd, the 4p exit channel, in the 4p gated spectrum and 3p gated spectrum should be equal to the ratio of the probability of detecting 4 and 3 protons for the 4p exit channel. Following this rule the ratios

$$R_{4p/3p} = \frac{I(^{130}\mathrm{Nd})_{4p}}{I(^{130}\mathrm{Nd})_{3p}} = \frac{1 \times \varepsilon^4}{4 \times \varepsilon^3(1-\varepsilon)} = \frac{1}{4}\frac{\varepsilon}{1-\varepsilon}, \tag{4.1}$$

$$R_{4p/2p} = \frac{I(^{130}\mathrm{Nd})_{4p}}{I(^{130}\mathrm{Nd})_{2p}} = \frac{1 \times \varepsilon^4}{6 \times \varepsilon^2(1-\varepsilon)^2} = \frac{1}{6}\frac{\varepsilon^2}{(1-\varepsilon)^2}, \tag{4.2}$$

$$R_{4p/1p} = \frac{I(^{130}\mathrm{Nd})_{4p}}{I(^{130}\mathrm{Nd})_{1p}} = \frac{1 \times \varepsilon^4}{4 \times \varepsilon(1-\varepsilon)^3} = \frac{1}{4}\frac{\varepsilon^3}{(1-\varepsilon)^3}, \tag{4.3}$$

are obtained and the general rule for the intensity of the γ rays is

$$R_{np/kp} = \frac{I(^{A}_{Z}\mathrm{X})_{np}}{I(^{A}_{Z}\mathrm{X})_{kp}} = \frac{1}{\binom{n}{k}}\frac{\varepsilon^{n-k}}{(1-\varepsilon)^{n-k}}, \tag{4.4}$$

where n and k are the number of particles of the exit channel and the corresponding detected number of particles, respectively, and $\binom{n}{k}$ the binomial coefficient $\binom{n}{k} = n!/(k!(n-k)!)$.

In order to calculate the proton detection efficiency of DIAMANT the strong 326 keV transition of the 4p exit channel ^{130}Nd is used. In Table 4.3 this proton detection efficiency has been calculated using three different ratios, giving an average of $\varepsilon = 47(2)\%$.

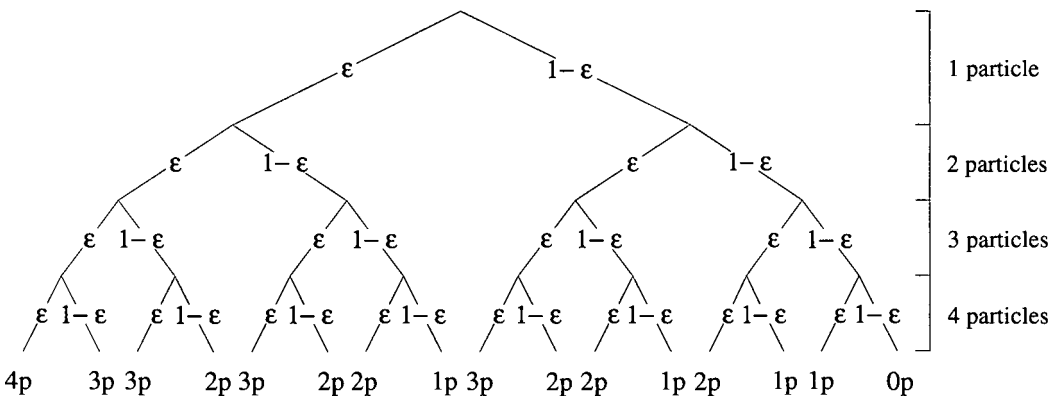

Figure 4.10: Binary tree showing the probability distribution of detecting one, two, three and four particles in the four-particle exit channel.

Table 4.2: Probability of detecting zero, one, two, three or four protons when there are four protons emitted from the compound system.

Number of detected protons	Probability of detection
0	$1 \times (1-\varepsilon)^4$
1	$4 \times \varepsilon(1-\varepsilon)^3$
2	$6 \times \varepsilon^2(1-\varepsilon)^2$
3	$4 \times \varepsilon^3(1-\varepsilon)$
4	$1 \times \varepsilon^4$

Table 4.3: Calculation of the proton efficiency of DIAMANT from the ratio of the intensity of the 326 keV transition of the 4p exit channel (^{130}Nd).

^{130}Nd, E_γ = 326 keV, 4p channel		
np/kp	R	ε
4p/3p	292(23)/1241(53) = 0.24(2)	0.49(5)
4p/2p	292(23)/2299(85) = 0.13(1)	0.47(2)
4p/1p	292(23)/1916(123) = 0.15(2)	0.46(2)

4.3.2 Suppression Shield

Events that deposit a fraction of their energy in the EXOGAM HPGe detector before scattering out can be suppressed in two ways. The first method, which is the most inefficient, uses the summed energy information from the suppression-shield elements of each Clover and vetoes those γ events that are in coincidence with an event in the shield. The major disadvantage of this method is that the elements of the shield surrounding each crystal are not handled separately. In this way an event can be vetoed in crystal A, for example, when the shield surrounding crystal B has fired. This results in a dramatic decrease of $\sim$ 90% in the statistics. In Figs. 4.11(a) and (b) γ-ray spectra without and with the use of the Compton shield described in this paragraph are presented, respectively. The dramatic decrease in the statistics is evident.

The second method of suppressing the Compton events is by using the "BGO pattern" of the so-called "quadrant suppression". This is a 12-bit word that corresponds to each element of the crystal and the shield, as shown in Table 4.4, and which is generated from the DAQ. By using this pattern, the Compton-suppression-shield information can be used separately for each crystal. The suppressed events involve a Ge bit for a specific crystal switched on (1) and the bits that correspond to the equivalent BGO and CsI switched off (0). In Fig. 4.12 the fusion-evaporation-event statistics for different combinations of Ge and shield elements firing are presented. From this figure one can see that the aforementioned suppressed events constitute only a small percentage of the total number of events that have fired the Ge crystal (histogram 9 versus histogram 3, respectively, which vary between 18% and 30%). The anti-Compton shield has fired for the majority of the events (Fig. 4.11(c)). However, it is not clear in what percentage this is due to the high background radioactivity induced by the beam and built up at and around the target position or to the malfunctioning of the "BGO pattern", evident from Fig. 4.13. For this reason the suppression shield could not be reliably used in the data analysis. The DIAMANT gates should be enough to clean the γ-ray spectrum from the background radioactivity of the beam.

Table 4.4: "BGO pattern" bit correspondence.

Signal	Bit	Signal	Bit	Signal	Bit
Ge(A)	1	BGO(A)	5	CsI(A)	9
Ge(B)	2	BGO(B)	6	CsI(B)	10
Ge(C)	3	BGO(C)	7	CsI(C)	11
Ge(D)	4	BGO(D)	8	CsI(D)	12

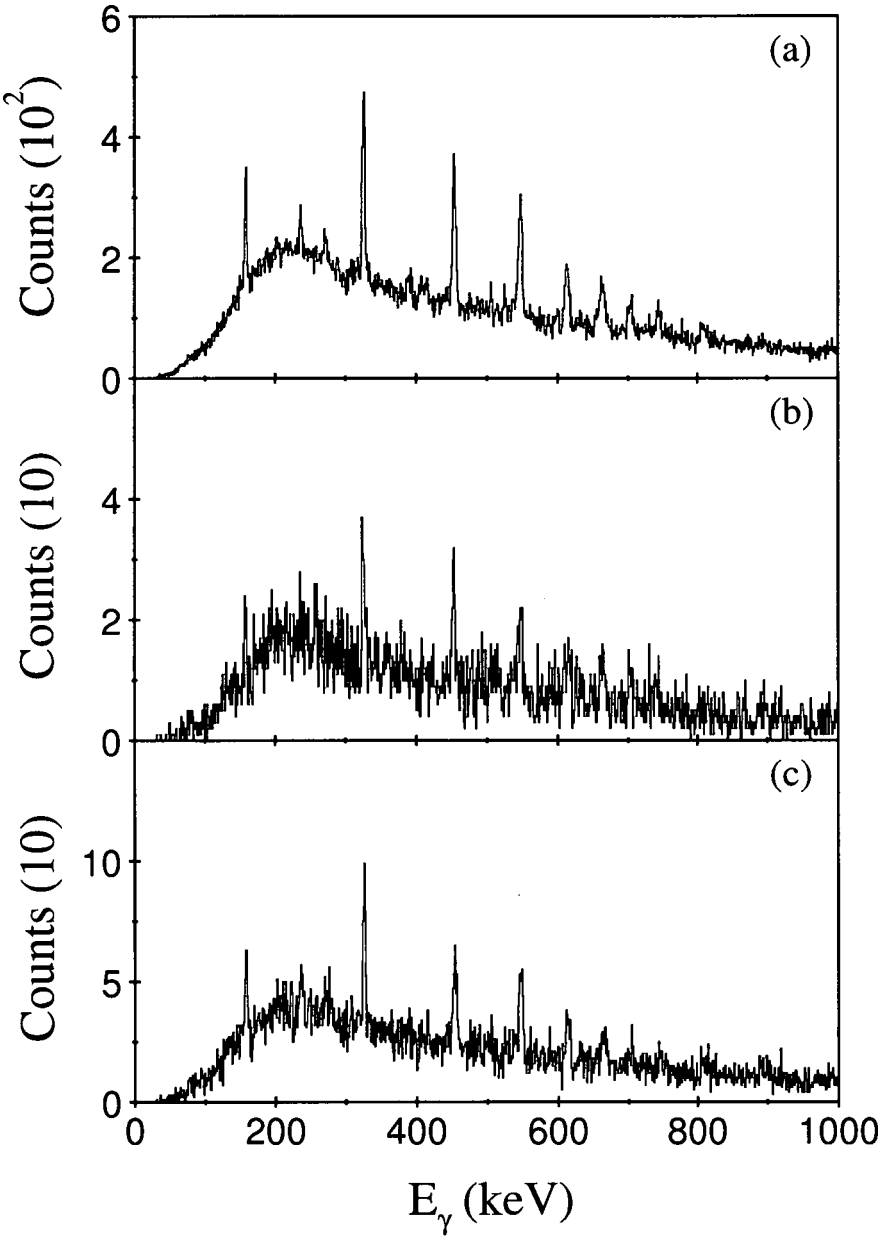

Figure 4.11: Gamma-ray spectra (1 keV/channel) in coincidence with at least three-proton emission (a) without Compton suppression, (b) with Compton suppression, using the summed energy information from the shield, (c) with Compton suppression, using the "BGO pattern". In (c) only events corresponding to "(9) Only Ge fires" of Fig. 4.12 are incremented.

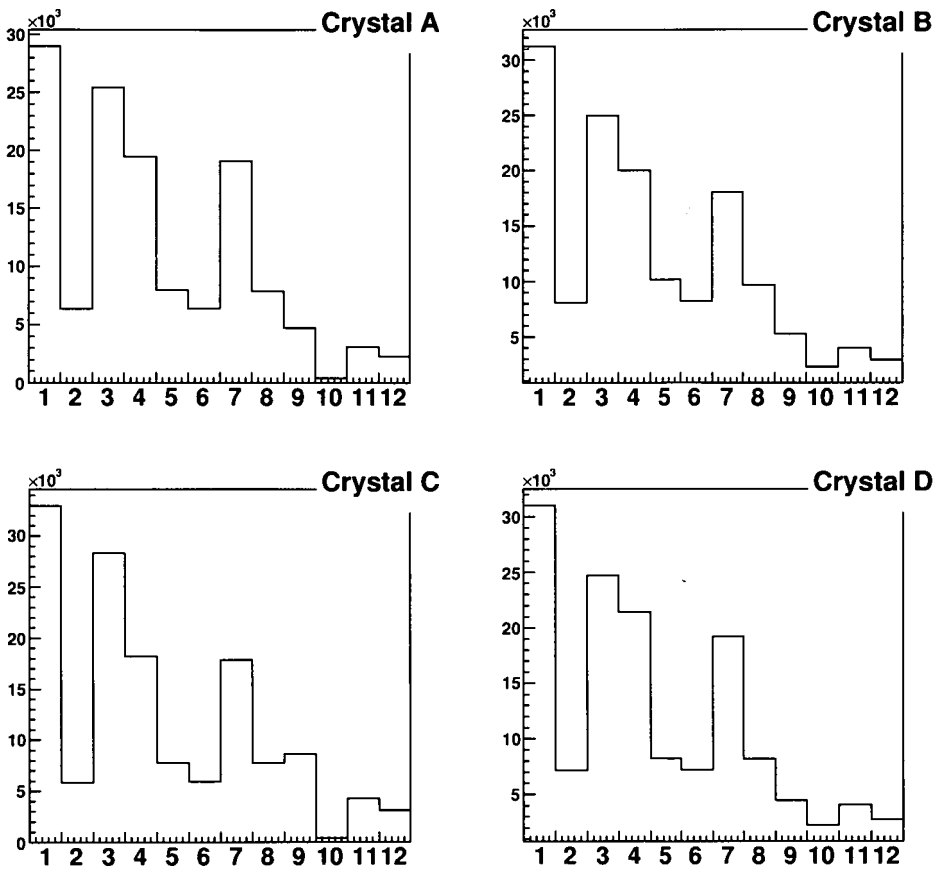

Figure 4.12: Statistics for events that are in coincidence with at least three-proton emission signalled by DIAMANT. (1) All events passing the gate. (2) Ge plus BGO plus CsI fire. (3) Ge fires (independently of BGO and CsI). (4) BGO fires (independently of Ge and CsI). (5) CsI fires (independently of Ge and BGO). (6) BGO and CsI fire (independently of Ge). (7) Ge and BGO fire (independently of CsI). (8) Ge and CsI fire (independently of BGO). (9) Only Ge fires. (10) Only shielding fires (BGO or CsI) (11) No signal from the Crystal. (12) "BGO pattern" does not work at all.

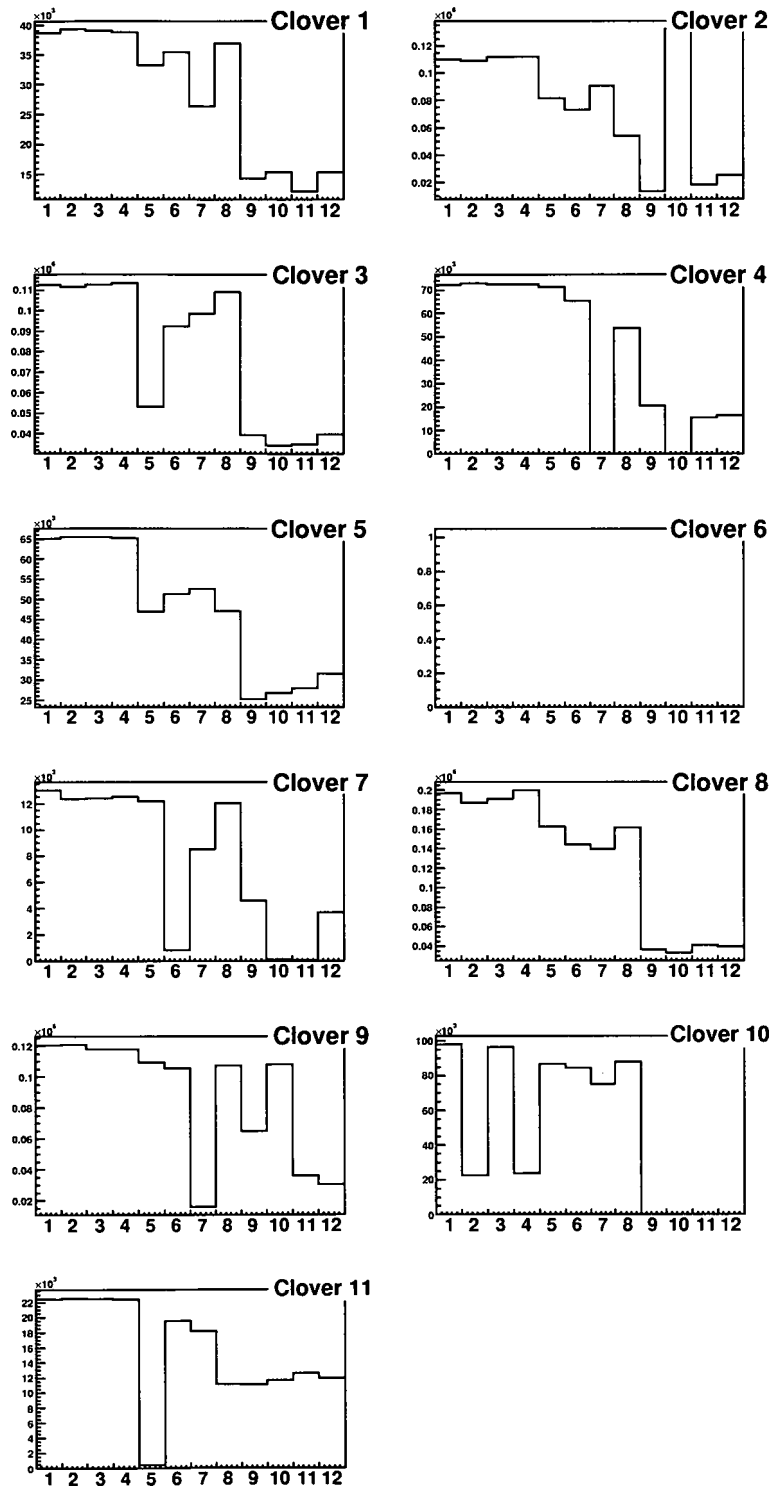

Figure 4.13: "BGO pattern" for all 11 Clovers of the experiment. The BGO pattern of Clover 6 does not work, while the rest do not present a 100% good function.

4.3.3 Crystal Addback

The crystal-addback technique involves the summation of all the γ events within a Clover, treating them as Compton-scattered events, increasing thus the photopeak efficiency of the array. The addback factor represents the increase in the photopeak efficiency, when the crystal addback has been applied. In Fig. 4.14 the simulated addback factor at 1.3 MeV as a function of the γ-ray multiplicity is shown for the full 16 Clover EXOGAM array and for the two different configurations A and B, while the straight line for addback factor equal to one represents the gain in efficiency if no addback has been used. The decrease of this factor for increasing γ multiplicity is due to pile up effects.

The γ-ray multiplicity in the present experiment for a highly selective DIAMANT gate, i.e. at least three-proton emission, is shown in Fig. 4.15. Although the addback technique would increase the detection efficiency and the peak-to-total ratio of the γ-ray spectra for high-energy γ rays, this is not the case for the present experiment, as the γ rays of interest are low-energy γ rays and no scattering between multiple crystals (three or four) is expected, as shown in Fig. 4.16. Most of the multiple-scattered events are either background or separate events. So, the addback technique has been applied only for a maximum of two crystals firing in the Clover. In Fig. 4.17(b) the resulting spectrum with the crystal addback is presented, where the events that fire one crystal have been Doppler corrected using the angle of the fired crystal and the events that scatter within two crystals have been corrected with the mean angle of the two crystals, i.e. $(\theta_1+\theta_2)/2$, while their energy is the sum of the energies of the two hits. The events that scatter within three and four crystals have been removed. From Fig. 4.17 it is obvious that there is not a difference between the two spectra apart from the slightly fewer statistics when applying the addback, since the three- and four-crystal events have been removed. This was expected as the low-energy γ rays of interest do not scatter within many crystals. The crystal-addback technique is very useful for higher-energy γ rays, but not appropriate for the present experiment.

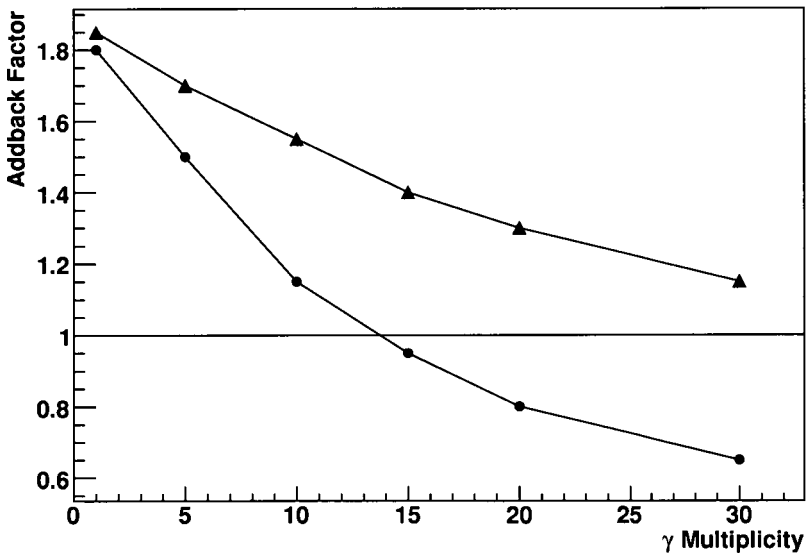

Figure 4.14: Simulated addback factor for 16 EXOGAM Clovers in configurations A (circles) and B (triangles) at 1.3 MeV as a function of the γ-ray multiplicity [46, 64]. The case where no addback has been applied is represented by the straight line for addback factor equal to one.

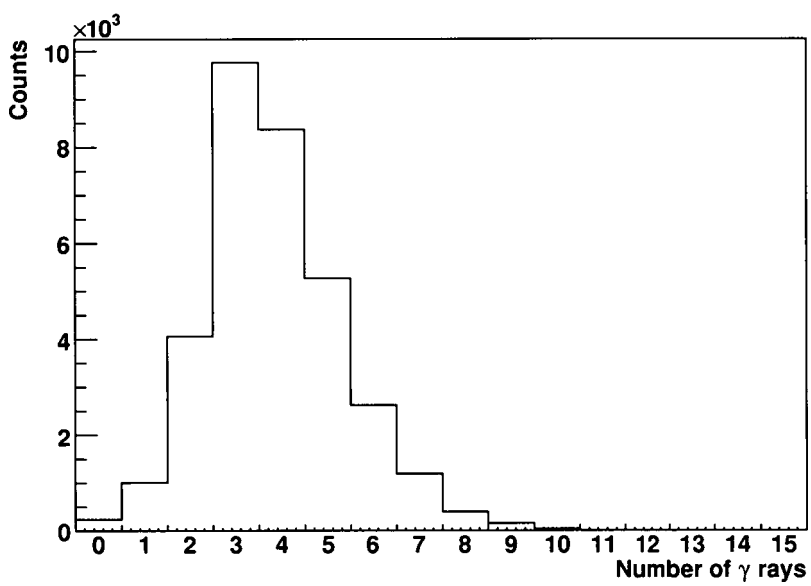

Figure 4.15: Gamma-ray multiplicity in coincidence with at least three protons signalled by DIAMANT. The mean value of this distribution is equal to 4.3.

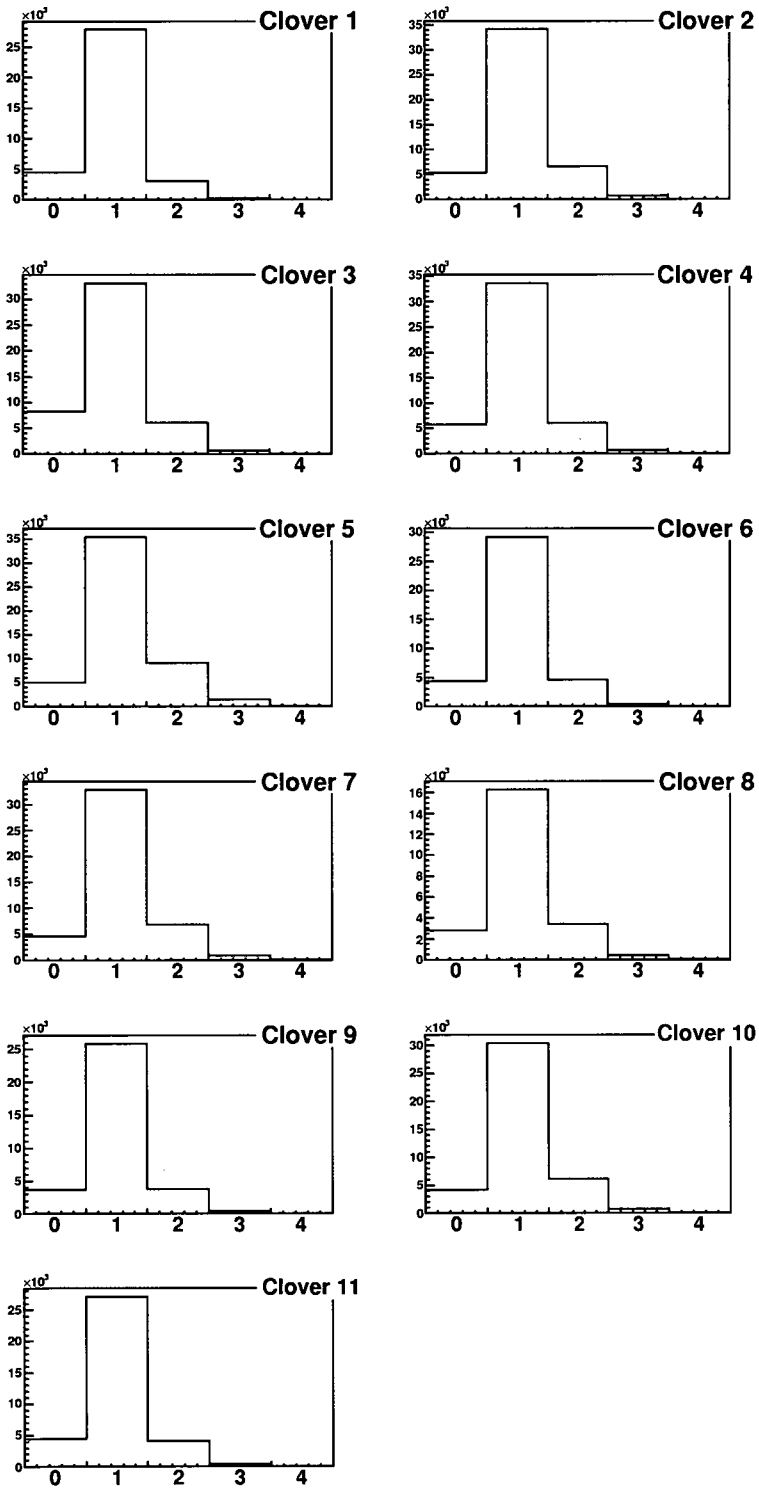

Figure 4.16: Number of HPGe crystals firing in each Clover (crystal multiplicity) for γ events that are in coincidence with at least two-proton emission signalled by DIAMANT when no addback has been applied.

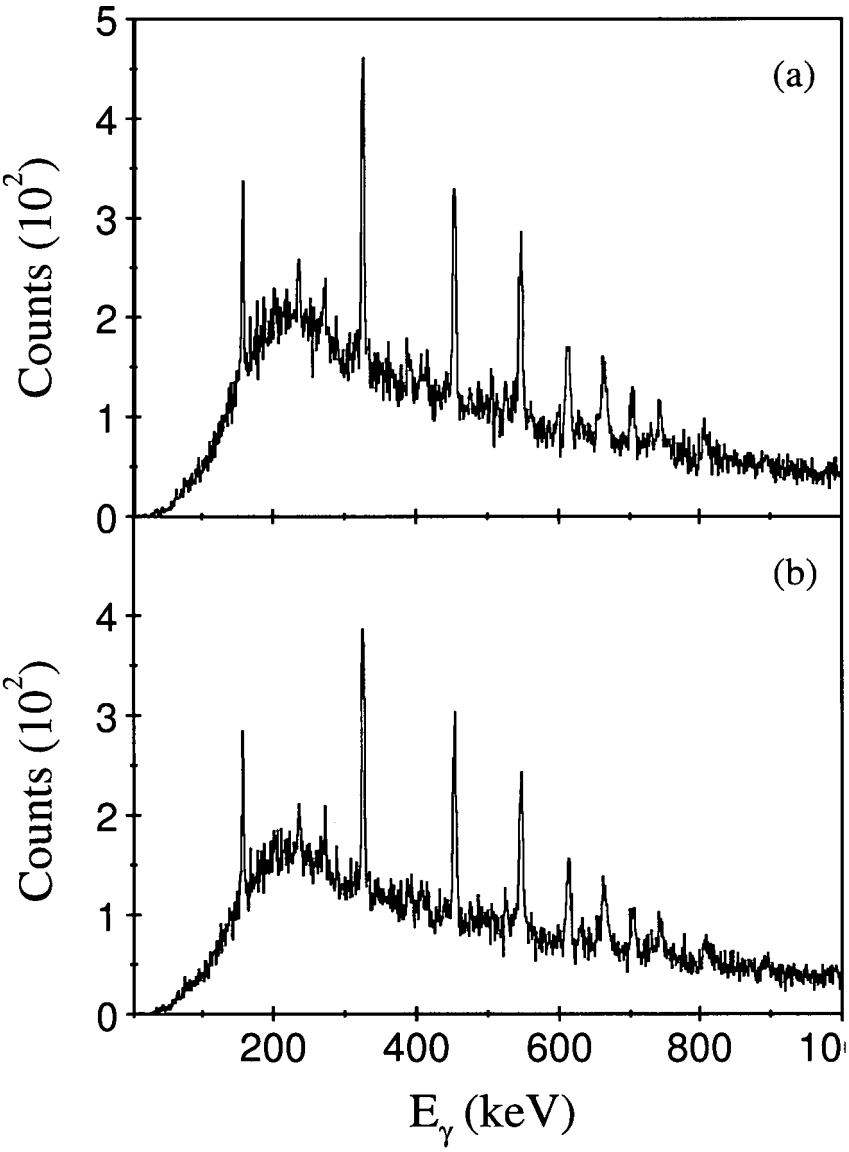

Figure 4.17: Gamma-ray spectra (1 keV/channel) in coincidence with at least three-proton emission (a) without and (b) with crystal addback.

4.3.4 Segment-Hit Pattern

The idea of the "segment-hit pattern" is to use the angle information from the hits recorded in the segments and apply this to the energy given by the centre contact for each crystal. In this experiment three scenarios are considered, constituting $\sim$ 70% of the fusion-evaporation γ events according to Fig. 4.18, and which are illustrated in Fig. 4.19.

1. Only one segment fires in the Clover. The energy from the centre contact, in which the fired segment corresponds, is corrected using the angle information from the fired segment. The corresponding γ-ray spectrum is shown in Fig. 4.20(a).

2. Two segments fire in the Clover. In this case one should further distinguish the following options:

   - Both segments come from the same crystal and the mean angle of the two segments, i.e. $(\theta_1 + \theta_2)/2$, is used to correct the energy centre-contact signal for the crystal. The γ-ray spectrum that matches these events is shown in Fig. 4.20(b).
   - The two fired segments correspond to different crystals and in addition they are not neighbours[2]. In this case each hit can be assumed as independent from the other, and thus the energy centre-contact signal can be used for each crystal separately correcting with the corresponding fired-segment angle. This γ-ray spectrum is shown in Fig. 4.20(d).

3. Three segments fire in the Clover. The simplest case of all three segments corresponding to the same crystal is taken into account and the angle of the crystal is used. Such a γ-ray spectrum is shown in Fig. 4.20(c).

In order to examine the improvement in the quality of γ-ray spectra when using the "segment-hit pattern", the peak-to-background (P/B) ratio, the peak-to-total (P/T) ratio and the resolution (FWHM) of the γ peaks have been calculated experimentally. The results are shown in Table 4.5. In this context, the P/B ratio of a γ peak is defined as the ratio of the count in the highest photopeak channel to the mean count of the background under this peak. Similarly, the P/T ratio is defined as the ratio of the peak area to the total area under the peak (peak plus peak background).

There is indeed a significant improvement in the γ-ray spectrum when using the "segment-hit pattern", as can be seen in Figs. 4.21, 4.22 and 4.23, with the P/B and P/T ratios improvement reaching values as high as $\sim$ 70% and $\sim$ 40%, respectively. This is due to the more accurate Doppler correction and the reduced opening angle of

[2]In between a hit in crystal A and a hit in B, C, or D as neighbours are characterised the following combinations of segments: 1-6, 1-7, 2-6, 2-7, 2-10, 2-13, 2-14, 3-13 and 3-14.

the detector because of the use of the segment information. Moreover, selecting events that do not exceed scattering into more than three segments reduces the background, as the energy range of the γ rays of interest do not support events that scatter within many segments.

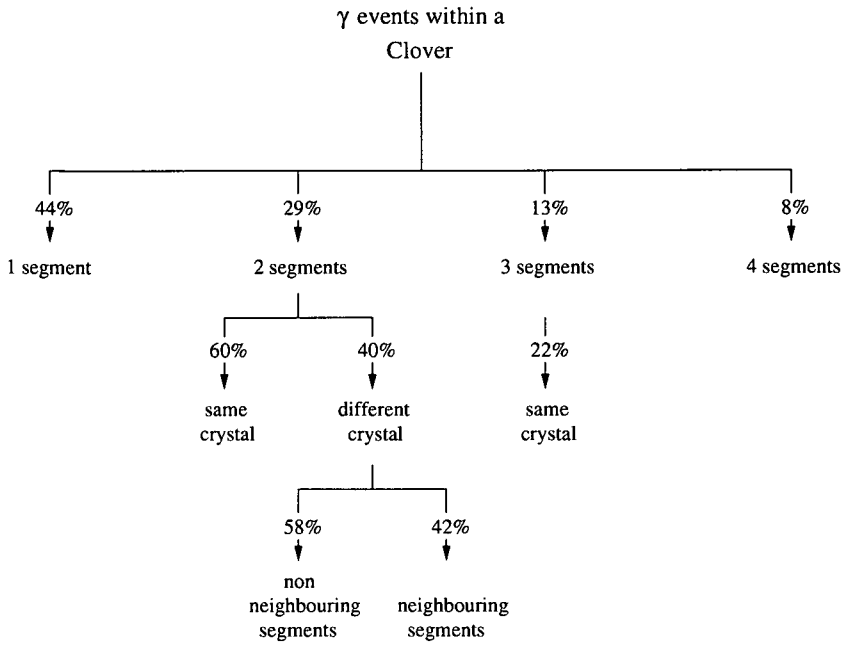

Figure 4.18: Experimentally calculated percentages of the number of segments that fire for a γ event in an EXOGAM Clover when a highly selective DIAMANT gate is satisfied. These percentages are independent of the fusion-evaporation exit channel, i.e. at least 2p, 3p or 4p emission.

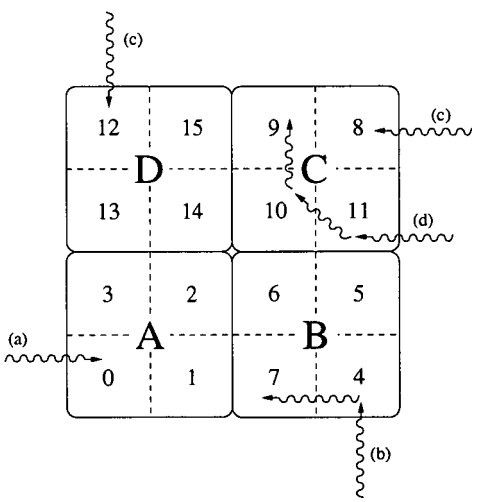

Figure 4.19: Segment configuration within an EXOGAM Clover detector. The following cases are illustrated: (a) only one segment fires (segment 0), (b) two segments fire within the same HPGe crystal due to Compton scattering (segments 4 and 7), (c) two segments fire (segment 12 and 8), but they are not neighbouring, thus they are treated as different events and (d) three segments fire within the same HPGe crystal (segments 11, 10 and 9).

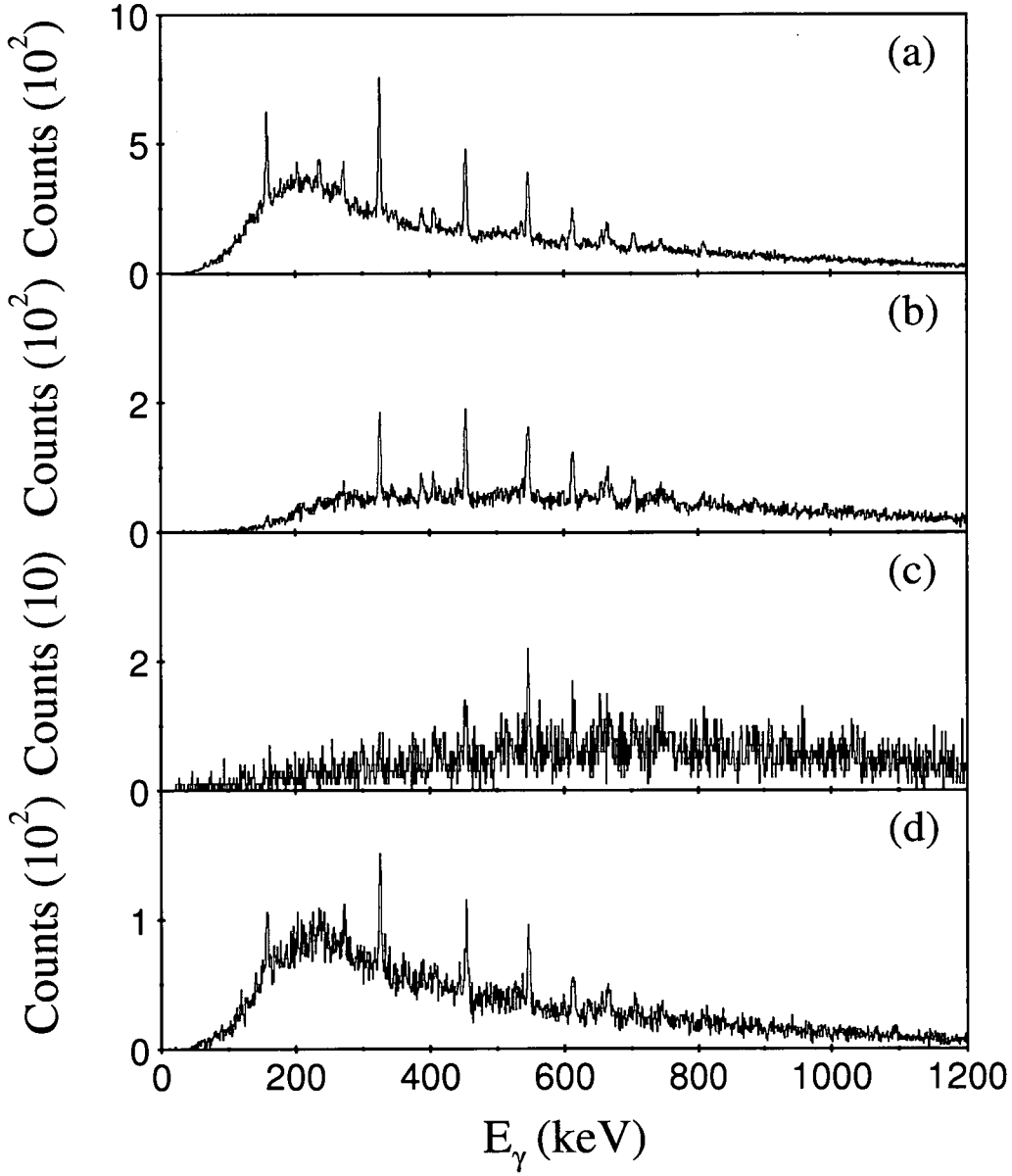

Figure 4.20: Gamma-ray spectra (1 kev/channel) in coincidence with at least two-proton emission when (a) one segment fires, (b) two segments fire within the same crystal, (c) three segments fire within the same crystal and (d) two non-neighbouring segments fire in two different crystals. In (a) there is still background at low energy. This can be understood from events that either hit one segment and escape or events that hit more than one segment, but only one fires due to the high energy threshold that some segments present. Spectrum (d) presents even more background at low energy which is consistent with the fact that in the case of two firing non-neighbouring segments in different crystals, there is a percentage of the events that correspond to scatterings of the γ rays, but have not been identified as such.

Table 4.5: The peak-to-background (P/B) ratio, the peak-to-total (P/T) ratio and the FWHM measured for three different energies and three exit channels with (ON) or without (OFF) the use of the "segment-hit pattern". The P/B values within parentheses represent a tentative calculation of the ratio due to limited statistics.

		158 keV		
Exit channel	"Hit Pattern"	P/B	P/T	FWHM (keV)
at least 2p	OFF	1.9	0.24	3.6(2)
	ON	2.3	0.28	3.6(2)
at least 3p	OFF	2.3	0.32	3.1(2)
	ON	2.9	0.33	3.2(3)
at least 4p	OFF	2.5	0.47	2.6(5)
	ON	(4.3)	0.51	2.3(4)
		326 keV		
Exit channel	"Hit Pattern"	P/B	P/T	FWHM (keV)
at least 2p	OFF	2.3	0.31	4.3(1)
	ON	3.2	0.39	3.5(1)
at least 3p	OFF	3.0	0.41	4.5(2)
	ON	4.3	0.50	3.4(1)
at least 4p	OFF	3.5	0.50	4.5(5)
	ON	(6.0)	0.58	3.8(4)
		704 keV		
Exit channel	"Hit Pattern"	P/B	P/T	FWHM (keV)
at least 2p	OFF	1.4	0.18	7.6(8)
	ON	1.7	0.25	5.8(5)
at least 3p	OFF	1.8	0.26	7.2(9)
	ON	2.1	0.35	5.3(6)
at least 4p	OFF	(3.0)	0.48	8.3(16)
	ON	(4.3)	0.58	6.7(12)

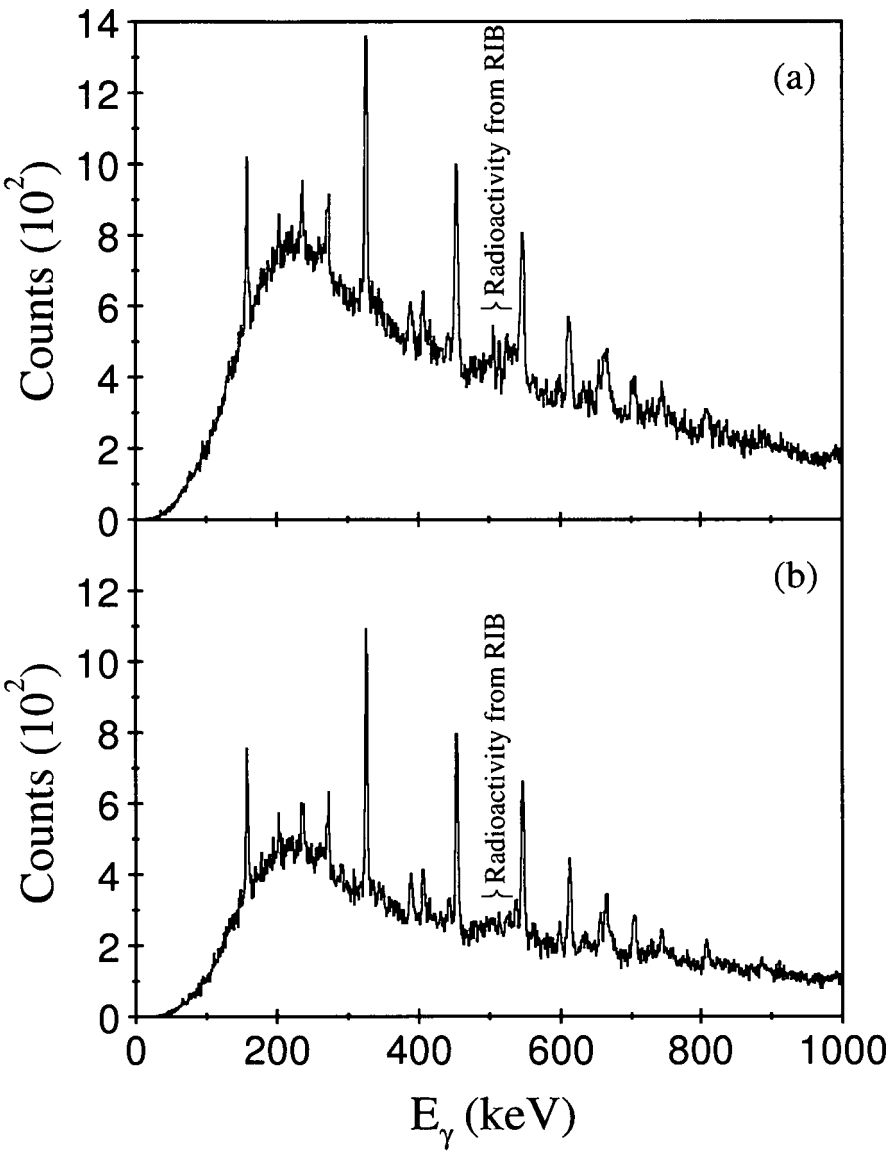

Figure 4.21: Gamma-ray spectra (1 keV/channel) in coincidence with at least two-proton emission (a) without the "segment-hit pattern" and (b) using the information from the segments. There is an improvement in the peak-to-background and peak-to-total ratios and in the resolution. Moreover, the background radioactivity peaks visible in (a) disappear in (b) due to the selectivity in the events that the "segment-hit pattern" demands.

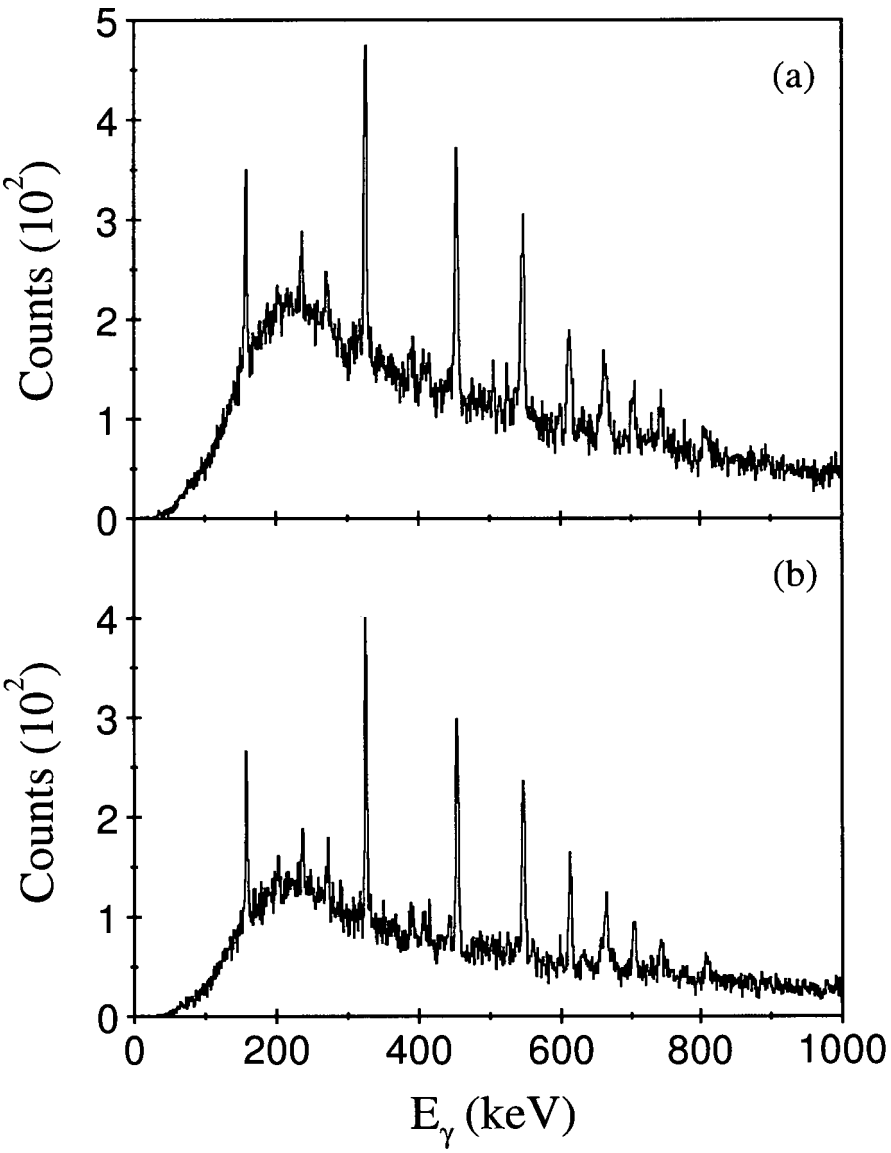

Figure 4.22: Gamma-ray spectra (1 keV/channel) in coincidence with at least three-proton emission (a) without the "segment-hit pattern" and (b) using the information from the segments.

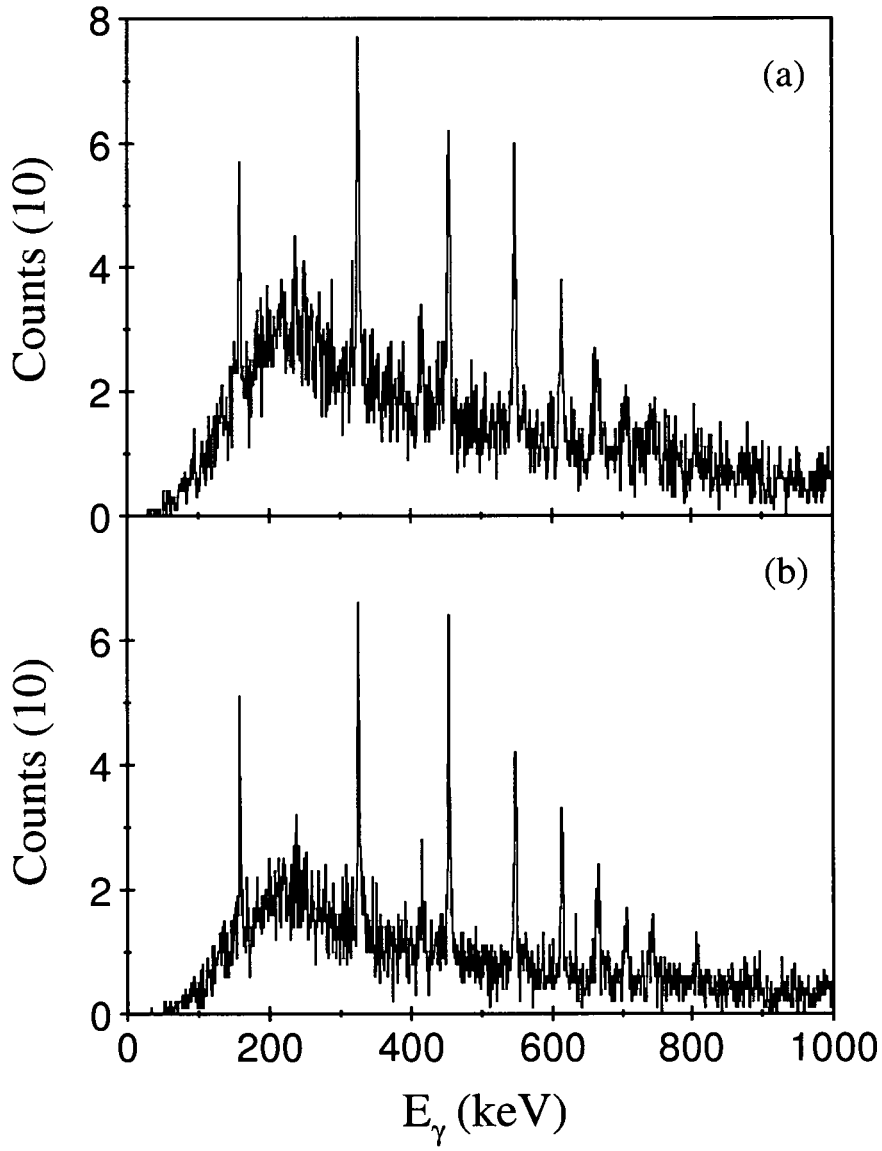

Figure 4.23: Gamma-ray spectra (1 keV/channel) in coincidence with at least four-proton emission (a) without the "segment-hit pattern" and (b) using the information from the segments.

4.3.5 Fusion-Evaporation Spectra

After improving the fusion-evaporation γ-ray spectra by applying all the gates and restrictions described in the previous sections, the γ rays observed in this experiment are presented. These γ rays correspond to the 3.4×10^5 fusion-evaporation events recorded during the experiment.

In Fig. 4.24 γ rays in coincidence with at least two protons detected by DIAMANT are shown. States in ^{130}Nd up to spin 22^+, ^{131}Pm up to spin $27/2^-$, ^{129}Pr up to spin $35/2^-$ and ^{127}Pr up to spin $27/2^-$ have been identified. In Fig. 4.25 γ rays in coincidence with at least one α particle detected by DIAMANT are shown. States in ^{128}Nd up to spin 16^+, ^{127}Pr up to spin $35/2^-$ and ^{126}Ce up to spin 6^+ have been identified. These γ rays are presented in more details in Tables 4.6 and 4.7.

Both spectra exhibit γ rays that have not been identified as transitions depopulating the aforementioned isotopes. These γ rays have been marked as unknown and since there is no recoil identification from VAMOS, they cannot be assigned to any nucleus.

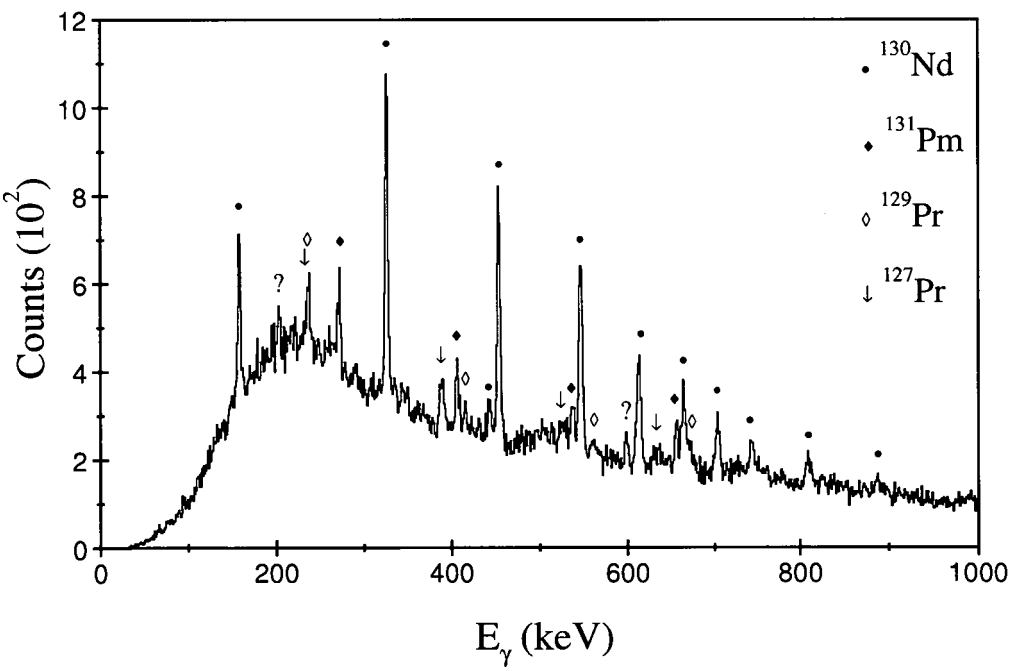

Figure 4.24: Gamma-ray spectrum (1 keV/channel) in coincidence with at least two-proton emission using the "segment-hit pattern". Known γ rays have been marked for four exit channels, while two γ rays do not correspond to any known transitions in the populated nuclei. These peaks are marked by a question mark (?).

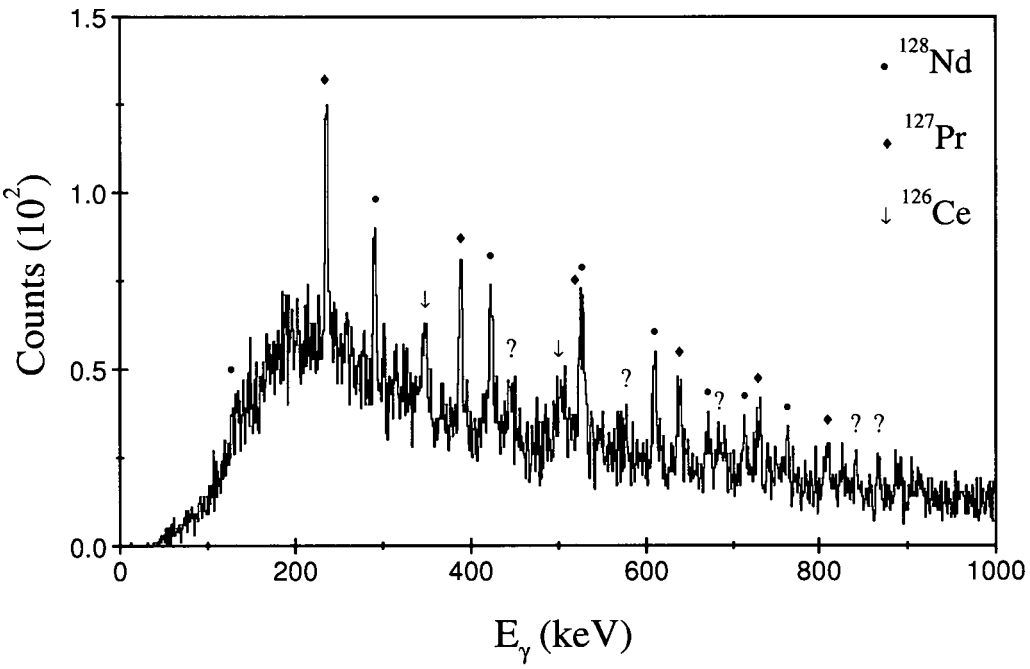

Figure 4.25: Gamma-ray spectrum (1 keV/channel) in coincidence with at least one α-particle emission using the "segment-hit pattern". Known γ rays have been marked for three exit channels, while γ rays that do not correspond to any known transitions in the populated nuclei have been marked by a question mark (?).

Table 4.6: Gamma-ray transitions observed in coincidence with at least two-proton emission in Fig. 4.24.

E_γ (keV)	Nucleus	Evaporated Particles	Transition
158.3(8)	^{130}Nd	4p	$2^+ \rightarrow 0^+$
326.2(5)	^{130}Nd	4p	$4^+ \rightarrow 2^+$
454.3(6)	^{130}Nd	4p	$6^+ \rightarrow 4^+$
547.1(8)	^{130}Nd	4p	$8^+ \rightarrow 6^+$
613.2(2)	^{130}Nd	4p	$10^+ \rightarrow 8^+$
664.5(3)	^{130}Nd	4p	$12^+ \rightarrow 10^+$
704.0(3)	^{130}Nd	4p	$14^+ \rightarrow 12^+$
744.6(3)	^{130}Nd	4p	$16^+ \rightarrow 14^+$
809.2(4)	^{130}Nd	4p	$18^+ \rightarrow 16^+$
896.7(10)	^{130}Nd	4p	$20^+ \rightarrow 18^+$
991.1(10)	^{130}Nd	4p	$22^+ \rightarrow 20^+$
886.8(8)	^{130}Nd	4p	$(5^-) \rightarrow 6^+$
443.5(3)	^{130}Nd	4p	$9^{(-)} \rightarrow 7^{(-)}$
546.0(10)	^{130}Nd	4p	$11^{(-)} \rightarrow 9^{(-)}$
630.5(6)	^{130}Nd	4p	$13^{(-)} \rightarrow 11^{(-)}$
272.4(2)	^{131}Pm	3p	$15/2^- \rightarrow 11/2^-$
406.9(2)	^{131}Pm	3p	$19/2^- \rightarrow 15/2^-$
537.7(3)	^{131}Pm	3p	$23/2^- \rightarrow 19/2^-$
656.2(4)	^{131}Pm	3p	$27/2^- \rightarrow 23/2^-$
237.1(3)	^{129}Pr	5p	$15/2^- \rightarrow 11/2^-$
415.4(7)	^{129}Pr	5p	$19/2^- \rightarrow 15/2^-$
560.3(8)	^{129}Pr	5p	$23/2^- \rightarrow 19/2^-$
672.1(5)	^{129}Pr	5p	$27/2^- \rightarrow 23/2^-$
(751(1))	^{129}Pr	5p	$(31/2^- \rightarrow 27/2^-)$
(810(1))	^{129}Pr	5p	$(35/2^- \rightarrow 31/2^-)$
236.0(10)	^{127}Pr	α3p	$15/2^- \rightarrow 11/2^-$
389.3(3)	^{127}Pr	α3p	$19/2^- \rightarrow 15/2^-$
526.1(6)	^{127}Pr	α3p	$23/2^- \rightarrow 19/2^-$
636.0(6)	^{127}Pr	α3p	$27/2^- \rightarrow 23/2^-$
203.4(4)	?		
599.0(5)	?		

Table 4.7: Gamma-ray transitions observed in coincidence with at least one α-particle emission in Fig. 4.25.

E_γ (keV)	Nucleus	Evaporated Particles	Transition
133.5(8)	^{128}Nd	α2p	$2^+ \rightarrow 0^+$
291.4(2)	^{128}Nd	α2p	$4^+ \rightarrow 2^+$
423.6(4)	^{128}Nd	α2p	$6^+ \rightarrow 4^+$
529.5(8)	^{128}Nd	α2p	$8^+ \rightarrow 6^+$
610.2(4)	^{128}Nd	α2p	$10^+ \rightarrow 8^+$
670.1(9)	^{128}Nd	α2p	$12^+ \rightarrow 10^+$
714.4(6)	^{128}Nd	α2p	$14^+ \rightarrow 12^+$
764.0(10)	^{128}Nd	α2p	$16^+ \rightarrow 14^+$
236.2(2)	^{127}Pr	α3p	$15/2^- \rightarrow 11/2^-$
389.1(2)	^{127}Pr	α3p	$19/2^- \rightarrow 15/2^-$
525.2(8)	^{127}Pr	α3p	$23/2^- \rightarrow 19/2^-$
638.4(6)	^{127}Pr	α3p	$27/2^- \rightarrow 23/2^-$
730.3(7)	^{127}Pr	α3p	$31/2^- \rightarrow 27/2^-$
808.9(7)	^{127}Pr	α3p	$35/2^- \rightarrow 31/2^-$
349.8(4)	^{126}Ce	α4p	$4^+ \rightarrow 2^+$
499.0(12)	^{126}Ce	α4p	$6^+ \rightarrow 4^+$
446.0(10)	?		
578.0(10)	?		
687.0(10)	?		
843.0(10)	?		
868.0(10)	?		

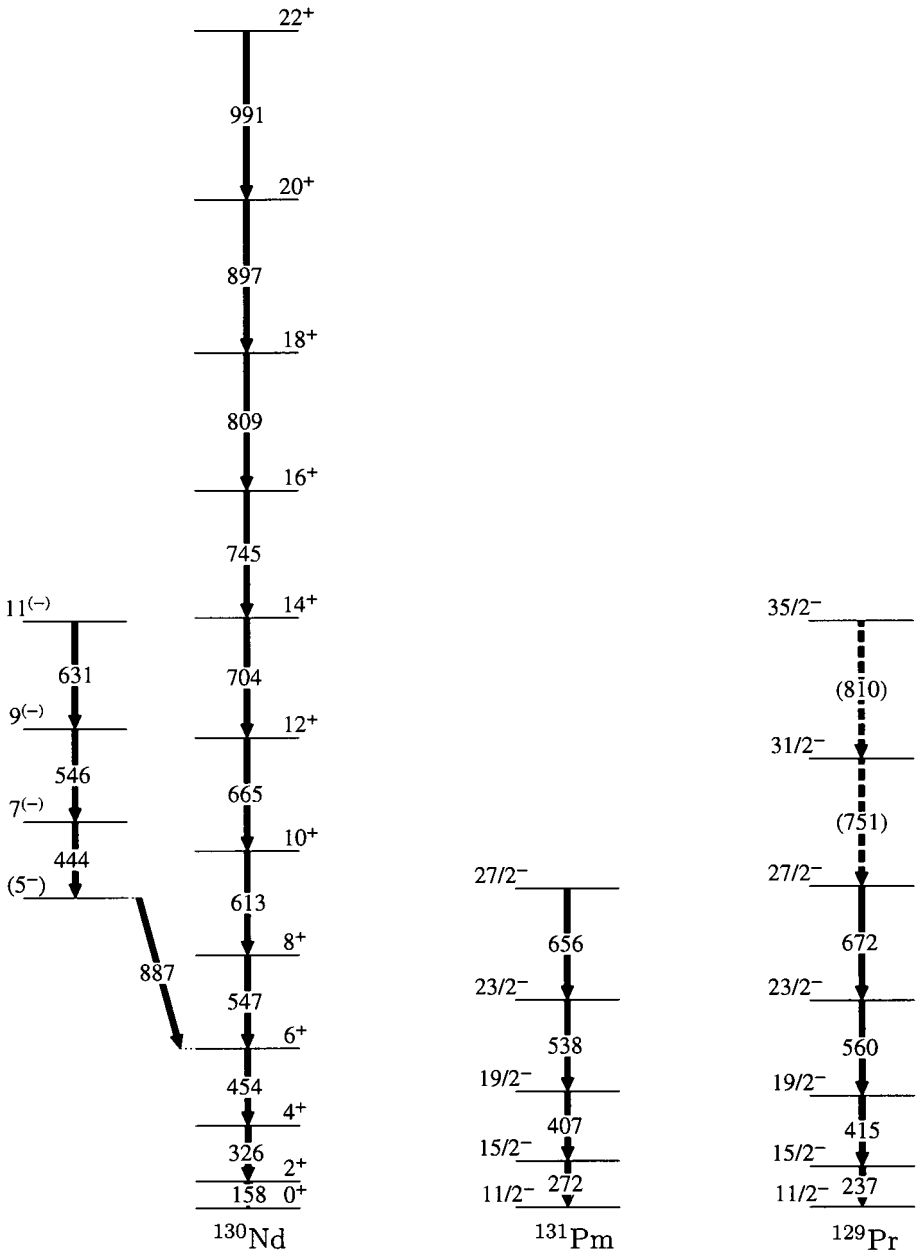

Figure 4.26: Reconstructed level schemes from γ-ray transitions observed in coincidence with at least two-proton emission in Fig. 4.24. These states in ^{130}Nd, ^{131}Pm and ^{129}Pr were already known.

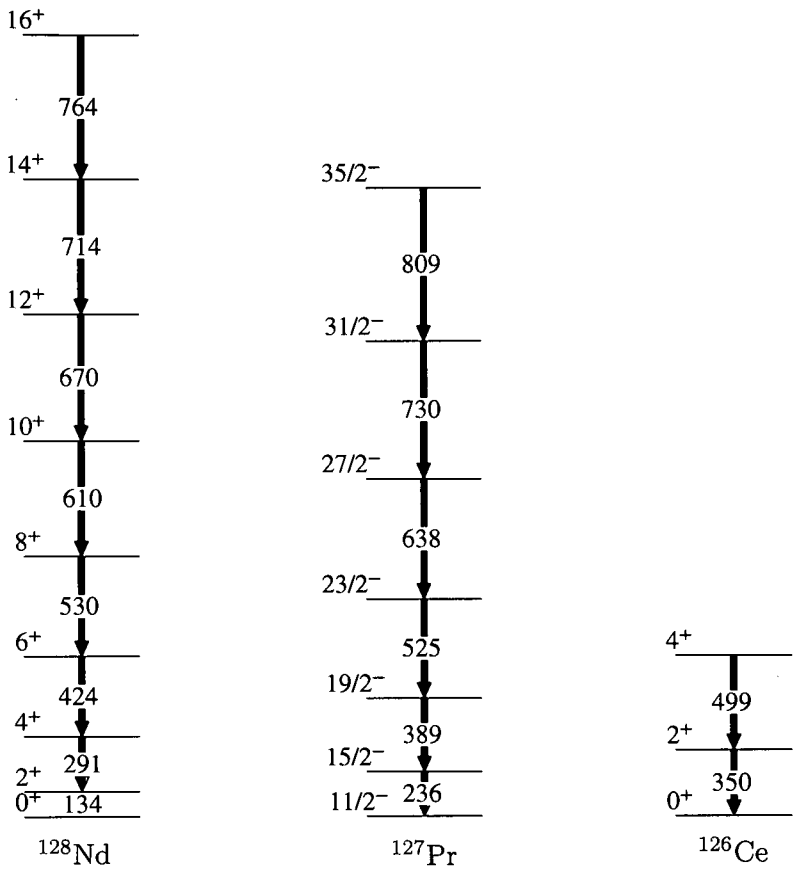

Figure 4.27: Reconstructed level schemes from γ-ray transitions observed in coincidence with at least one α-particle emission in Fig. 4.25. These states in ^{128}Nd, ^{127}Pr and ^{126}Ce were already known.

4.3.6 Cross-Section Sensitivity

Theoretical calculations using the ALICE code for the cross sections of the evaporation channels have allowed an estimation of the relative cross-section sensitivity of the present experimental setup according to the observed channels. This sensitivity is calculated by the theoretical cross section of the evaporated channels multiplied by the γ-ray intensity of their weakest transition that is observed in the γ-ray spectrum. The results are shown in Table 4.8, where a sensitivity of the order of 4 mb is estimated.

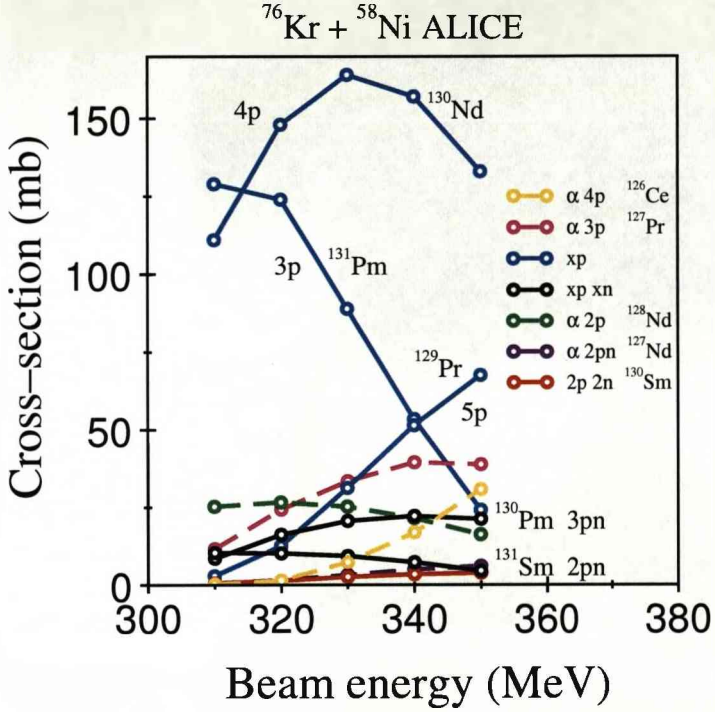

Figure 4.28: Predicted cross sections for residues of the ^{76}Kr + ^{58}Ni fusion-evaporation reaction using the ALICE code [67].

4.4 Discussion

Nuclear structure studies have received a boost in the last few years with the advent of RIBs. However, a lot of progress has yet to be made in terms of radioactive beam development. In the case of fusion-evaporation reactions, the state-of-the-art detection systems that have been developed can pick up the exit channels of interest, but the intensity of the beams and the available species has to grow.

In the case of the ^{76}Kr + ^{58}Ni fusion-evaporation reaction, the strong 4p exit channel (^{130}Nd) can be studied up to relatively high spin with the existing experimental setup. Moreover, transitions in the 3p, 5p and αxp exit channels were observed. However, this region of nuclei has been studied before.

Table 4.8: Relative cross-section (σ) sensitivity using the ALICE theoretical cross sections of the evaporated exit channels.

Observed Channels		Highest Spin	I_γ of highest observed transition	ALICE σ (mb)	Relative σ sensitivity (mb)
3p	$^{131}_{61}$Pm	$27/2^-$	-	89	-
4p	$^{130}_{60}$Nd	22^+	2.7% [68]	164	4
5p	$^{129}_{59}$Pr	$27/2^-$	-	31	-
α2p	$^{128}_{60}$Nd	16^+	32% [69]	25	8
α3p	$^{127}_{59}$Pr	$35/2^-$	-	33	-
α4p	$^{126}_{58}$Ce	6^+	92% [70]	7	6

If the strong exit channels of a certain combination of beam and target reaches a completely unknown region, new isotopes could be discovered and studied. For the Kr beams, if a lighter isotope was available at a reasonable intensity, i.e. ^{74}Kr or ^{72}Kr, a more exotic region would have been reached and many new nuclei could have been studied. A reaction that has been already proposed at TRIUMF [71], Canada, involves ^{76,75}Rb beams delivered from the new ISAC-II [72] facility. In the ^{75}Rb + ^{58}Ni fusion-evaporation reaction, the strong 3p and 4p exit channels will lead to ^{130}Sm and ^{129}Pm, respectively, and in the ^{76}Rb + ^{58}Ni reaction the strong 3p and 4p exit channels will lead to ^{131}Sm and ^{130}Pm.

Chapter 5

Nuclear Levels in Proton-Unbound ^{109}I: Relative Single-Particle Energies beyond the Proton Drip Line

Heavy nuclei with exotic values of neutron-proton ratios provide a fertile testing ground for nuclear models. For example, proton-rich nuclei in the A $\sim$ 110 region, illustrated in Fig. 5.1, close to the N = Z = 50 double shell closure, are of great interest since valuable information on single-particle energies and residual interactions with respect to the presumed doubly magic ^{100}Sn "core" can be extracted. In this regard, it is of paramount importance to follow single-particle energies systematically in nuclei ever closer to this doubly magic nucleus. As these nuclei approach the N = Z line, protons and neutrons near the Fermi surface occupy similar orbitals and proton-neutron pairing may be evident. Another intriguing feature of this mass region is predicted octupole collectivity in nuclei close to N = Z = 56 (^{112}Ba) [73]. For this particle number, a deformed octupole shell gap occurs and both proton and neutron orbitals that differ by $\Delta j = \Delta \ell = 3$, namely $h_{11/2}$ and $d_{5/2}$ states, are at the nuclear Fermi surface. Such orbitals are required for enhanced octupole collectivity [74].

Gamma-ray transitions in the proton-unbound ^{109}I nucleus were first proposed in Ref. [8]. However, in subsequent work [9] discrepancies of the γ-ray transitions assigned to ^{109}I were found. The present data, with a significant increase in the statistics over the previous experiments, has now allowed a resolution of the conflict and a new level scheme has been built for ^{109}I.

5.1 Proton Radioactivity

The proton drip line defines the limits of nuclear stability, confining nuclei that are energetically unstable to the emission of a proton from their ground states, i.e. nuclei lying beyond the proton drip line have a positive proton decay Q-value, $Q_p > 0$. Apart

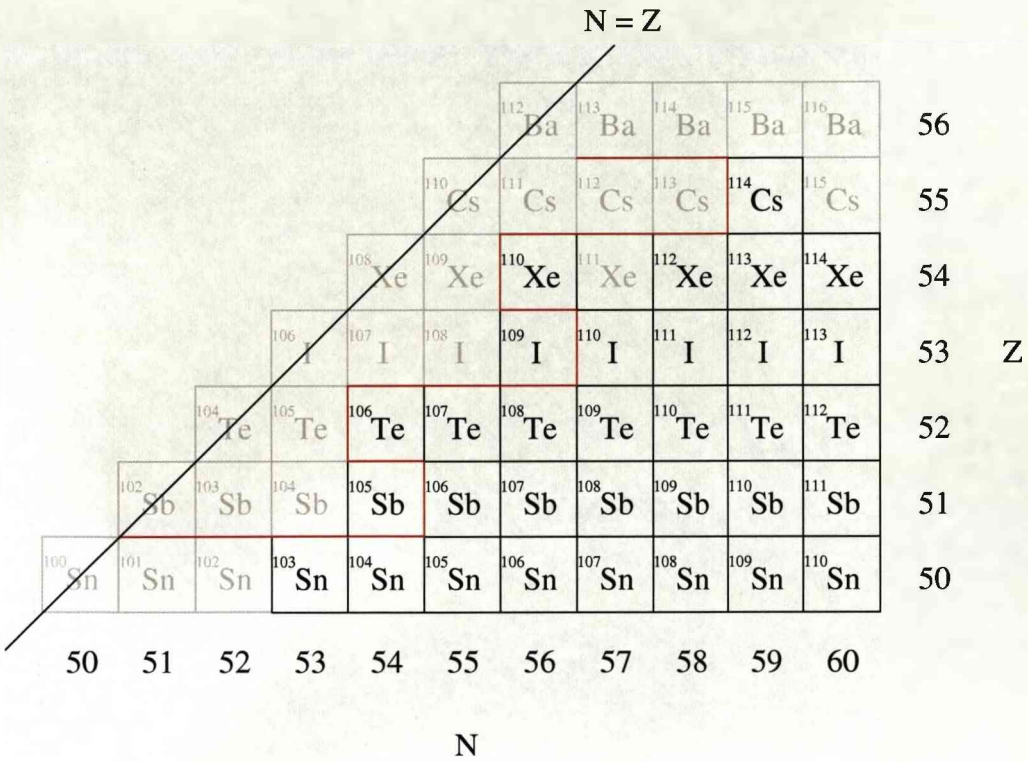

Figure 5.1: A $\sim$ 110 mass region. The highlighted-black isotopes correspond to nuclei with known excited states. The red line represents the experimental proton drip line.

from mapping the proton drip line, the so-called proton radioactivity is of great interest, since it constitutes a major spectroscopic tool for single-particle orbit identification of the emitted proton, as well as a testing ground for mass formulae models (from measurements of the separation energy of the proton).

Proton radioactivity is evident for high-Z nuclei, Z > 50, where the Coulomb barrier that the unbound proton has to penetrate, results in a measurable half-life for the decay. This half-life further depends on the orbital angular momentum ℓ of the emitted proton, since the centrifugal barrier affects the probability of the proton penetration. This is illustrated in Fig. 5.2, where the differences in the half-life depending on the suggested ℓ value of the proton are evident.

5.1.1 ^{109}I Proton Decay

The ground-state proton decay of ^{109}I was first observed by T. Faestermann *et al.* in 1984 [76] and then further studied by P. J. Sellin *et al.* in 1993 [77]. Its proton energy is deduced at $E_p = 813 \pm 4$ keV, its half-life at $T_{1/2} = 100 \pm 5$ μs and its branching ratio is $\approx$ 100%. In order to study the structure of ^{109}I by performing in-beam γ-ray spectroscopy, its excited states can be identified using its well-known ground-state proton decay as a tag in a recoil-decay-tagging experiment.

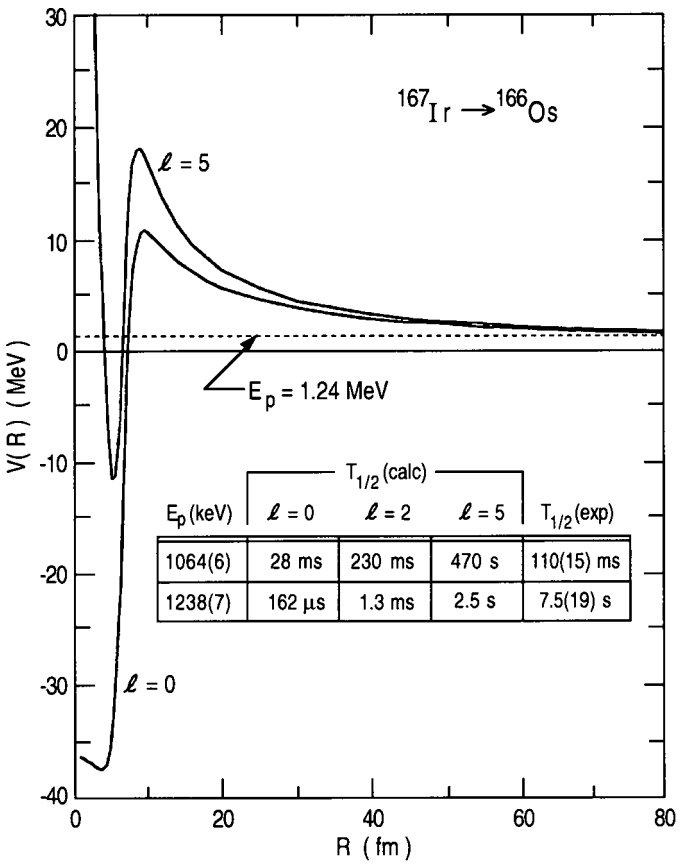

Figure 5.2: Potential between the proton and the daughter nucleus calculated for the proton decay of ^{167}Ir. The calculated half-lives come from the WKB approximation. The figure is taken from Ref. [75].

5.2 The Recoil-Decay-Tagging Technique

In order to perform in-beam γ-ray spectroscopy on a nucleus produced via a heavy-ion induced fusion-evaporation reaction, one should employ a method for high selectivity on the exit channel of interest, since the prompt γ-ray spectrum is dominated by background γ rays; i.e. γ rays from reaction products (fission, transfer) and Coulomb excitation. One method to select the channel of interest involves the identification of the evaporated particles emitted from the compound-system. Another way is to identify and separate the fusion products. In heavy-ion fusion-evaporation reactions one can take advantage of the reaction kinematics. The evaporation residues fly into a small cone in the forward direction and they can be distinguished from the beam-like particles using for instance a recoil separator. The prompt γ rays that correspond to pure fusion-evaporation channels can be identified by tagging on the recoils. This method is called the recoil-gating method.

The fusion-evaporation exit channels usually consist of more than one and if the

nucleus of interest is not strongly populated, then the recoil-gating technique is not sensitive enough. A very powerful method to probe very weakly populated channels is based on the characteristic decay (proton or α radioactivity) of the nucleus of interest and is called the recoil-decay-tagging (RDT) method [8, 78]. This technique combines the aforementioned recoil-gating method with the characteristic decay of the nucleus of interest.

5.2.1 The RDT Technique in JYFL

The recoil-decay-tagging technique, as it has been implemented in JYFL, is schematically shown in Fig. 5.3. Prompt γ rays are detected by the JUROGAM γ-ray spectrometer. The reaction products and the unreacted beam then fly through RITU, where the beam is dumped in the dipole chamber. The recoils are finally implanted into the DSSD of the GREAT focal plane. Their subsequent decays are then detected and the implanted recoil can be uniquely identified. Prompt γ rays are correlated with the identified recoils and assigned as transitions depopulating their excited states. In order to minimise the random correlations, the implantation of a recoil and its subsequent decay within a certain time window must take place within the same pixel of the DSSD.

In Fig. 5.4 the experimental setup used in JYFL for the RDT experiments is illustrated, while in Figs. 5.5 and 5.6 photographs of the JUROGAM array and the GREAT spectrometer are shown, respectively.

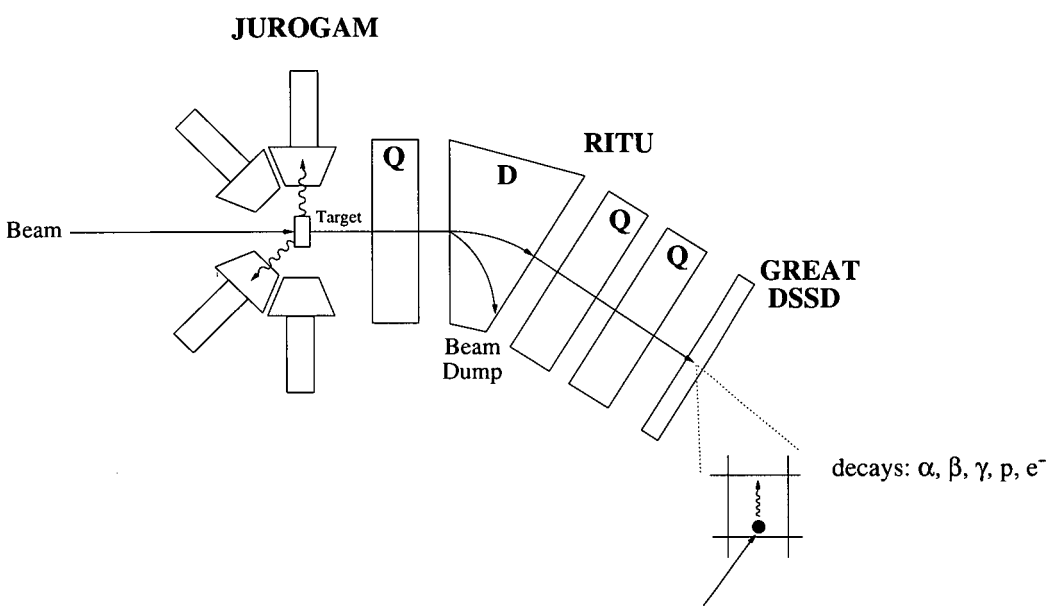

Figure 5.3: Schematic representation of the RDT technique as it is implemented in JYFL. Subsequent decays of the implanted recoils must occur within the same pixel of the DSSD, in order to minimise the random correlations.

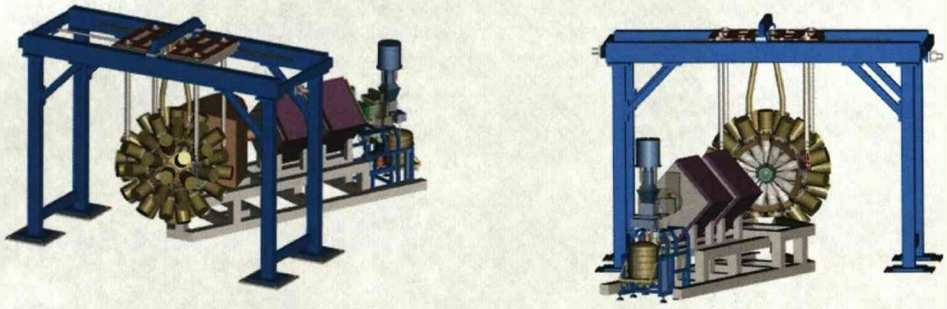

Figure 5.4: Visualisation of the experimental setup used in JYFL for the RDT experiments: JUROGAM in conjunction with the RITU gas-filled separator and the GREAT focal plane. The pictures are taken from Ref. [79].

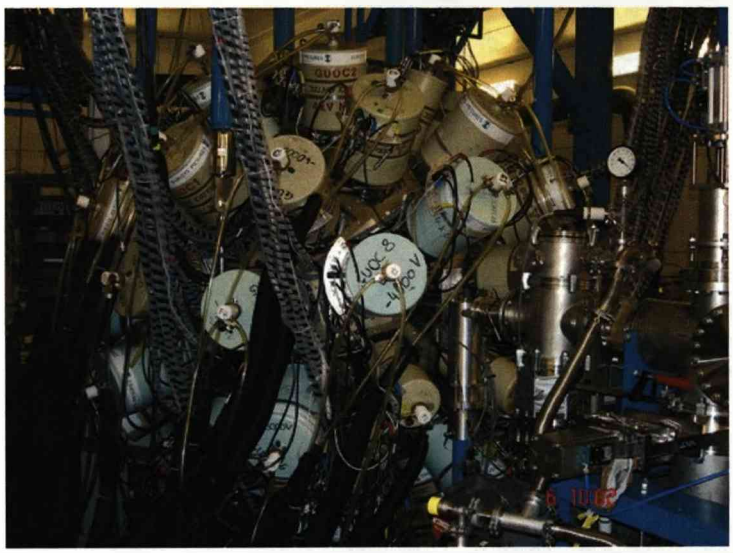

Figure 5.5: The JUROGAM array.

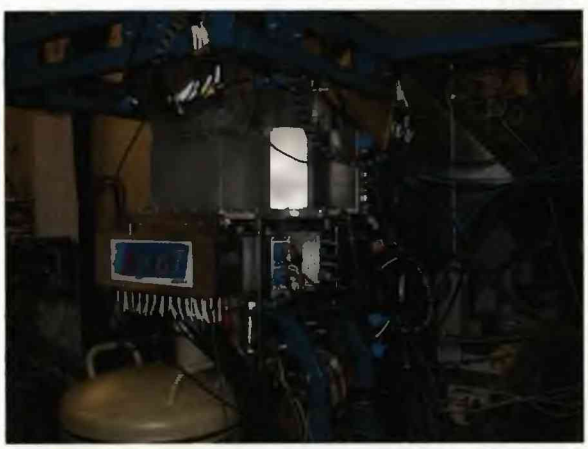

Figure 5.6: The GREAT focal plane.

5.3 Experimental Details

The experiment was performed at the Accelerator Laboratory of the University of Jyväskylä (JYFL), Finland. A $^{54}Fe^{10+}$ beam, delivered by the K130 Cyclotron of the laboratory at a near barrier energy of 195 MeV, was used to bombard a $\sim$ 1 mg/cm^2 self-supporting foil of isotopically enriched (99.8%) ^{58}Ni. A $\sim$ 50 μg/cm^2 carbon charge reset foil was mounted directly downstream of the target.

States in ^{109}I were populated using the ^{58}Ni(^{54}Fe, p2nγ) fusion-evaporation reaction. The irradiation time was around five days and the beam intensity of the order of 5 pnA. In beam γ-ray spectroscopy employing the Recoil-proton-Decay-Tagging method was performed to study the nucleus of interest. The experimental setup consisted of the JUROGAM γ-ray spectrometer coupled together with the RITU in-flight recoil separator and the GREAT focal-plane spectrometer combined with the Total Data Readout (TDR) acquisition system.

This experiment used an almost-symmetric reaction, which in the past had caused problems for beam/recoil discrimination in the RITU spectrometer. However, several improvements recently implemented in RITU, i.e. redesign of the dipole chamber and beam dump of the separator for better suppression of the beam particles, in conjunction with energy loss and time-of-flight information from the GREAT MWPC and DSSD, resulted in the first observation of γ rays in ^{106,107}Te [80, 81]. These nuclei were produced in the exactly symmetric ^{54}Fe + ^{54}Fe and nearly symmetric ^{52}Cr + ^{58}Ni reactions, respectively, with production cross sections as low as 25 nb for ^{106}Te.

5.3.1 Energy Calibration of JUROGAM Ge Detectors

In order to gain match and calibrate the 43 Ge detectors of the JUROGAM array a EuBa source (^{152}Eu and ^{133}Ba source) is used. The ADC of the Ge crystals has a non-linear response for low energies[1] and that imposes the need for an additional correction. Hence, the gain-matched/calibrated energy for each crystal is given by the following equation

$$E = A_1 + A_2x + A_3x^2 - A_4e^{-A_5x}\sin(A_6x + A_7), \tag{5.1}$$

where x is the channel number. The coefficients A_1, A_2, A_3 are obtained by fitting a quadratic function for higher energies, where the ADC responds linearly, and the coefficients A_4, A_5, A_6 and A_7 are obtained from a damped sine function that compensates for the non-linearity of the ADC.

In order to check the stability of the amplifiers of JUROGAM's Ge crystals, and thus the stability of the calibration, a matrix of the energy spectrum versus the events

[1]The JUROGAM array was set to 3 MeV full range. For a 16k spectrum (16384 channels) the first $\sim$ 1500 respond non-linearly, i.e. up until $\sim$ 274 keV.

is created for each crystal. For all the cases where the Ge crystals present drift during the experiment (Fig. 5.8) there are two solutions, either change the calibration of the crystal for specific parts of the experiment, given that the gain is changed but presents a stability, or remove the detector from the off-line analysis where appropriate. In order to change the gain-match coefficients of a detector when there is a shift during the experiment, the in-beam γ-ray spectrum is used instead of the source spectrum, given that there has not been any Doppler correction and that the spectrum that is used as a reference for the calibration of the shifted crystal comes from the same ring (same θ angle).

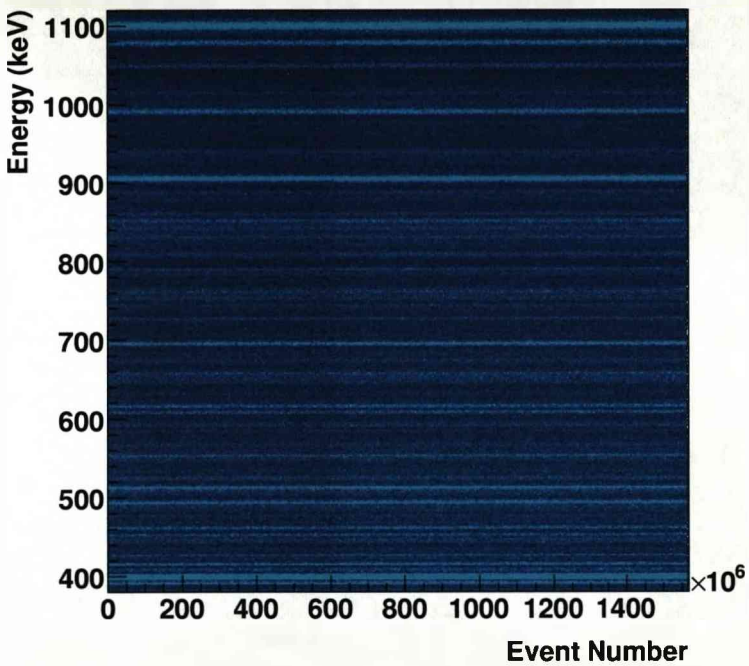

Figure 5.7: Specific γ-ray energy peaks versus the event number during the experiment. Any deviation from a straight line suggests drifts in the germanium crystals. This matrix shows a stable Ge detector throughout the experiment.

5.3.2 Energy Calibration of Si Strip Detectors

In order to gain match the Si strips an α source is used, which consists of three different α emitters, ^{239}Pu, ^{241}Am and ^{244}Cm, giving α particles with an energy range between 5 and 6 MeV. Because of the energy loss that the α particles suffer in the dead layers of the detector, the 3-α source provides an accurate gain matching for all the Si strips, but does not calibrate them energywise. In order to have an energy calibration for the Si strips, one needs to use peaks from activities produced in the irradiation and thus perform an internal calibration. Four possible peaks that could be used for internal calibration in this experiment correspond to the α decays of ^{109}Te (3107 keV), ^{108}Te

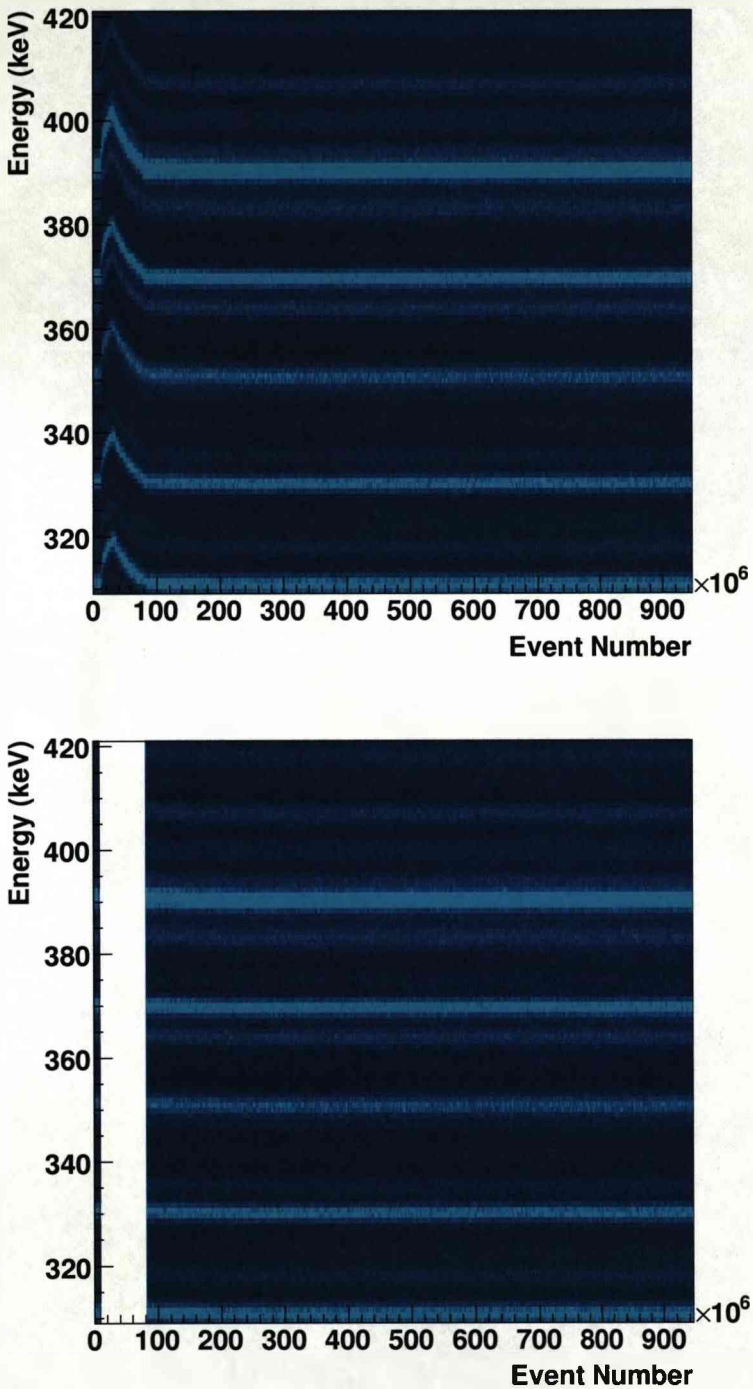

Figure 5.8: Energy spectrum of a particular Ge detector of JUROGAM versus the event number. A shift in the energy is observed which is compensated by turning the detector off in the off-line analysis for the events where the shift occurs.

(3317 keV), ^{110}I (3444 keV) and ^{107}Te (3863 keV).

However, the completion of the internal calibration suffered from the low production cross section of these isotopes, introducing large errors to the procedure due to the low statistics within the peaks. Moreover, the fact that the energy of these α decays is more than 2-3 MeV higher than the proton-decay energy of ^{109}I suggests that even if the internal calibration provides a precise calibration for all the α decays in that energy region, that does not guarantee a good energy calibration for lower energies. Finally, the low energy of the proton decay ($\sim$ 800 keV) falls very close to the non-linear part of the ADC, which induces yet more uncertainty to the calibration procedure.

Since the proton energy is needed only for tagging, in combination with the fact that the α spectrum presents almost no background within the decay time of ^{109}I (there is not another decay in the energy region of ^{109}I within its time window), one can adjust the gain coefficient manually so that the proton energy is 813 keV. This fine tuning makes tagging easier.

5.3.3 Recoil Identification

As mentioned in Section 3.16, the stored data from the TDR acquisition system have satisfied a software trigger, but they still need to be correlated off-line. In order to achieve this the data must satisfy another software trigger that will create the events to be analysed. The software Event Builder in this experiment used the "OR(DSSD)" trigger, which sets the event time to zero when there is any signal from the DSSD at the focal plane, as shown in Fig. 5.9.

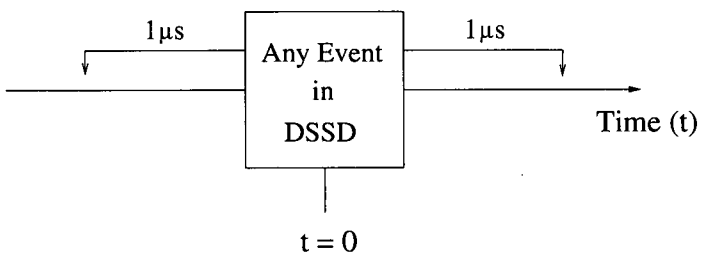

Figure 5.9: Event reconstruction from stored data using the TDR acquisition system and the "OR(DSSD)" trigger. For this experiment an event is triggered from any DSSD signal (t = 0) and consists of everything stored within 1 μs before and after it.

In the DSSD both scattered and unreacted beam, as well as the recoils are implanted. Moreover, the subsequent decays from the recoils also trigger the Si strip detectors. In order to distinguish between all these events the MWPC and the time-of-flight between the MWPC and the DSSD will be employed.

The events in anti-coincidence with the MWPC signal are characterised as de-

cays. In order to distinguish between the recoils and the beam-like particles, a two-dimensional (2D) plot of the energy loss in the MWPC versus the time-of-flight between the MWPC and the DSSD is created and a 2D gate is set where the recoils are expected, as illustrated in Fig. 5.10. By identifying the recoils and correlating them with prompt γ rays detected by JUROGAM, one obtains a γ-ray spectrum that includes transitions de-exciting all the populated fusion-evaporation channels from the reaction (Fig. 5.18(a) of Section 5.4, see later).

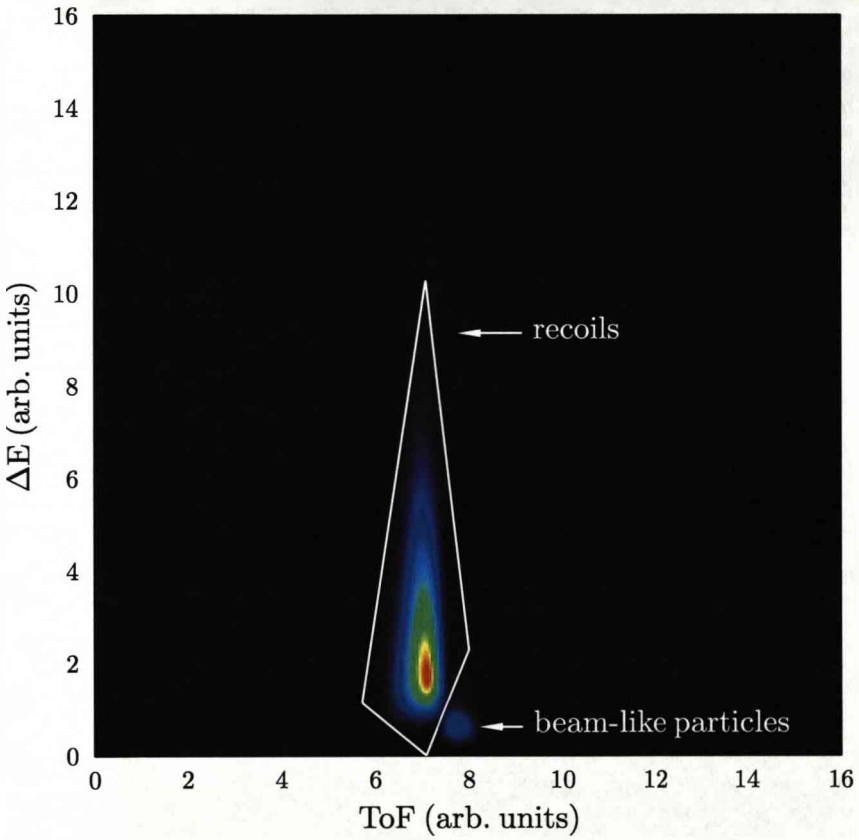

Figure 5.10: Two-dimensional (2D) plot of the energy loss in the MWPC and the time-of-flight between the MWPC and the DSSD. There is a good separation between the recoils and the beam-like particles and the 2D gate set on the recoils can be seen.

5.3.4 Proton Tagging

In order to select the nucleus of interest, its characteristic decay will be used. Searching for subsequent decays (events in anti-coincidence with the MWPC) of the recoils within the same pixel of the DSSD and within a time window that corresponds to $\approx 3 \times T_{1/2}$ of the decay, one can pick up the channel of interest.

In the case of ^{109}I, with known proton-decay half-life of $T_{1/2} \sim 100$ μs and energy of $E_p = 813$ keV, the search time window between a recoil implantation and its subsequent decay within the same pixel was set to 300 μs, while the energy window for these events was set to less than 1 MeV. The energy spectrum of the DSSD after satisfying the above mentioned conditions can be seen in Fig. 5.18(c) of Section 5.4.

In order to verify that the peak lying at ~ 815 keV corresponds to the ^{109}I proton decay, its half-life has been measured at $T_{1/2} = 92 \pm 1$ μs (Fig. 5.11), validating that the proton decay corresponds to the ground-state proton decay of ^{109}I and giving a more accurate value over the previous measurements.

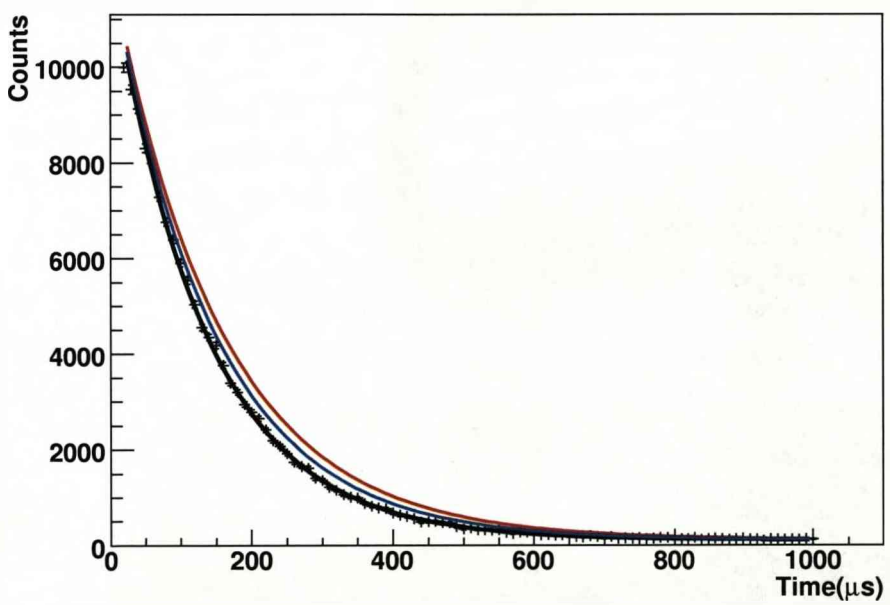

Figure 5.11: Exponential fit assuming constant background. In red and blue the previous half-lives of 107 and 100 μs have been drawn respectively, assuming same constants from the fit. The $T_{1/2} = 92 \pm 1$ μs curve in black fits the data best.

The ^{109}I proton-decay peak has been now fully identified, while the big bump at lower energies correspond to the β particles produced from the β decay of the other exit channels. By tagging on the identified ^{109}I proton decay, the prompt γ rays correlated with its recoil implantation correspond to transitions depopulating ^{109}I (Figs. 5.18(b) and 5.19 of Section 5.4).

5.3.5 Doppler Correction

The γ rays of interest, detected by the JUROGAM array, have been emitted by the recoiling nuclei and are thus Doppler shifted. In order to compensate for this shift the recoiling velocity $\beta = v/c$ has to be found and the Doppler correction formula (Eq. 3.9) has to be applied. The reaction kinematics of the fusion-evaporation channels permit the use of the angle of each detector with respect to the beam axis as the θ angle of Eq. 3.9. The β value was deduced experimentally by using the six different rings of detectors of the JUROGAM array (Table 3.2). Before any Doppler correction has been applied, the measured γ-ray energy (E_{det}) of a specific peak is different for each ring of JUROGAM (Fig. 5.12) depending on the angle θ of the ring as follows

$$E_\gamma = E_{det}\gamma(1 - \beta\cos\theta) \Rightarrow E_{det} = \frac{E_\gamma}{\gamma(1 - \beta\cos\theta)}. \tag{5.2}$$

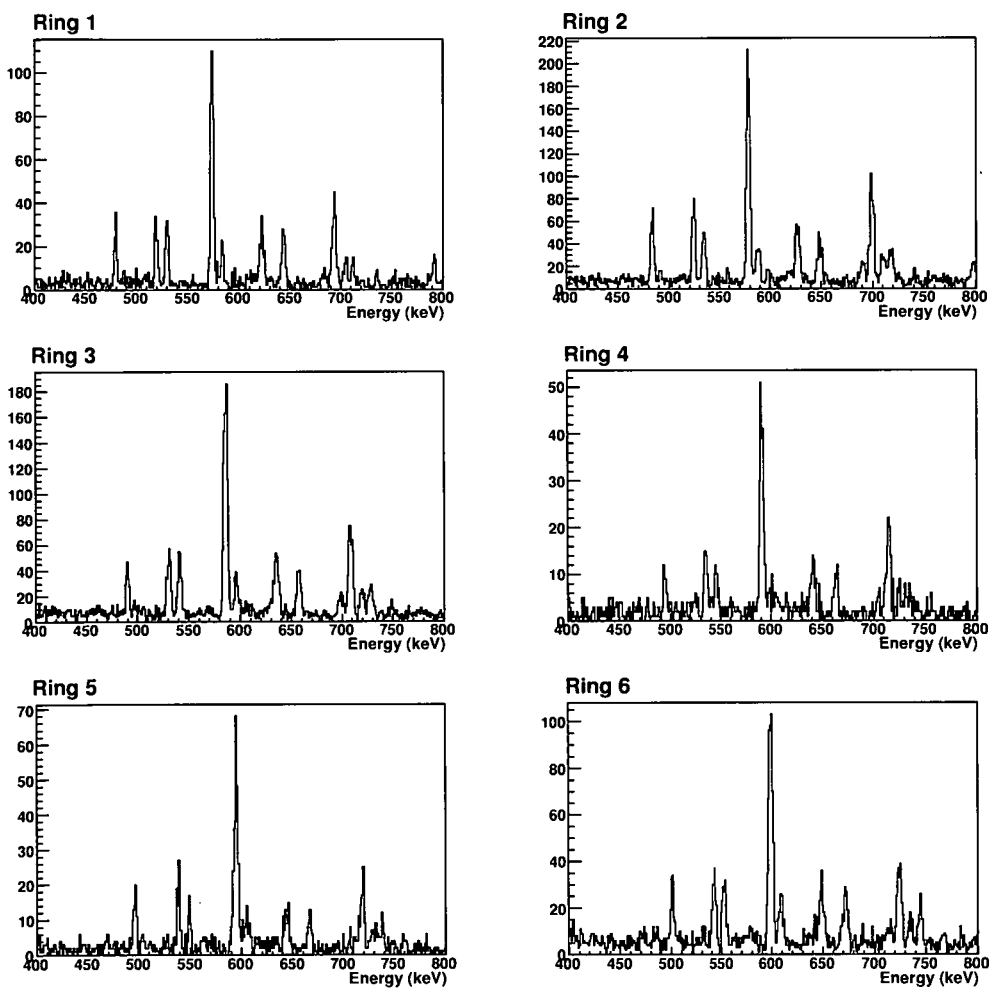

Figure 5.12: Singles γ-ray spectrum tagged on ^{109}I proton decay for each ring (constant θ) in the JUROGAM array.

According to Eq. 5.2, if one plots the measured γ-ray energy of, preferably, the strong 594 keV in each ring versus the $\cos\theta$ of the ring, the β value can be obtained by fitting to these points the function

$$y = \frac{E_\gamma}{\gamma(1-\beta x)}. \tag{5.3}$$

Following the aforementioned procedure, the β value of the ^{109}I recoils has been determined as $\beta = 0.036$ from the fit of Fig. 5.13.

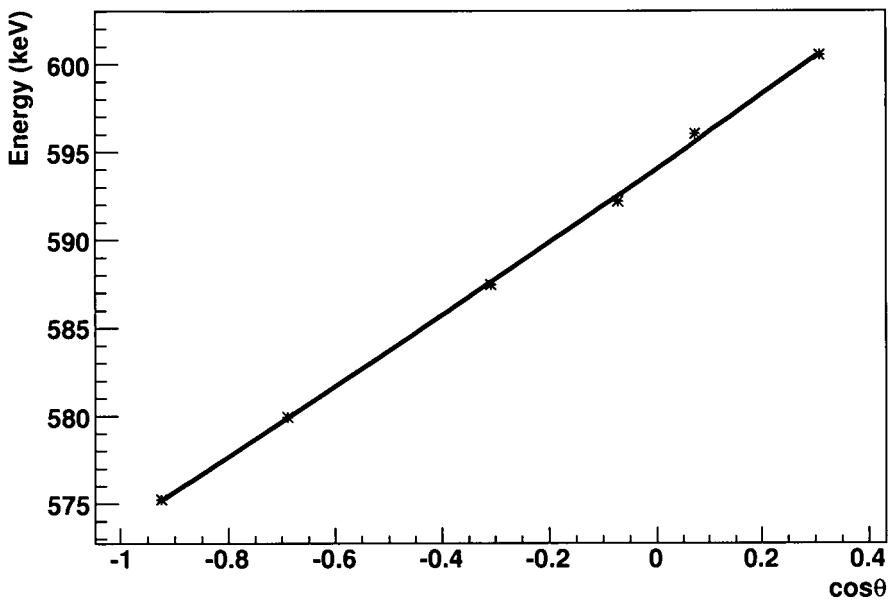

Figure 5.13: Fit to obtain the β value of the ^{109}I recoils, by plotting the energy of a γ ray versus the cosine of the angle of the detectors with respect to the beam axis.

5.3.6 JUROGAM Time Gates

The prompt γ rays that are correlated with a recoil implantation are separated from the background radiation at the target position by restricting the Ge time. Plotting the Ge response as a function of time (Fig. 5.14), the dominant peak at ≈ -500 ns corresponds to γ rays from nuclear reactions. The time difference between this peak and the recoil implantation, which sets the time to zero according to the "(OR)DSSD" gate, corresponds to the time-of-flight of the recoils through RITU.

Due to the different time response of each Ge detector (Fig. 5.15), separate gates of the order of 140 ns have been used for each crystal. In order to further suppress any background from the subsequent γ-ray analysis, a constraint in the $\gamma - \gamma$ coincidence time has been set (Fig. 5.16) at 80 ns. The $\gamma - \gamma$ coincidence time of Fig. 5.16 has already met the time gates mentioned above.

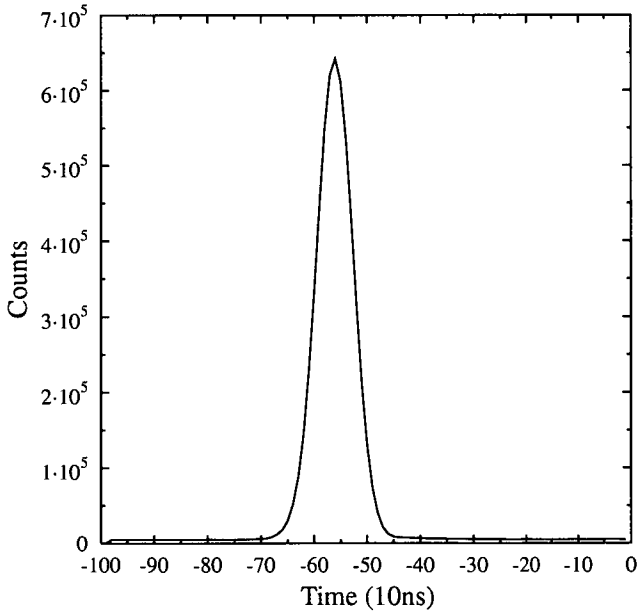

Figure 5.14: Time response of the Ge crystals of JUROGAM. The negative values of the time-axis is due to the fact that prompt γ rays are detected earlier in time due to the trigger condition "(OR)DSSD", which sets the time of a DSSD signal to zero.

In order to verify the stability of the time gates, a matrix of the time spectrum of each JUROGAM detector versus the event number throughout the experiment has been plotted, as illustrated in Fig. 5.17. A small change in the time-of-flight of the recoils through RITU has been identified from this plot and an adjustment to the time gates has been made accordingly. The change in the time-of-flight is due to a small change of the He gas pressure.

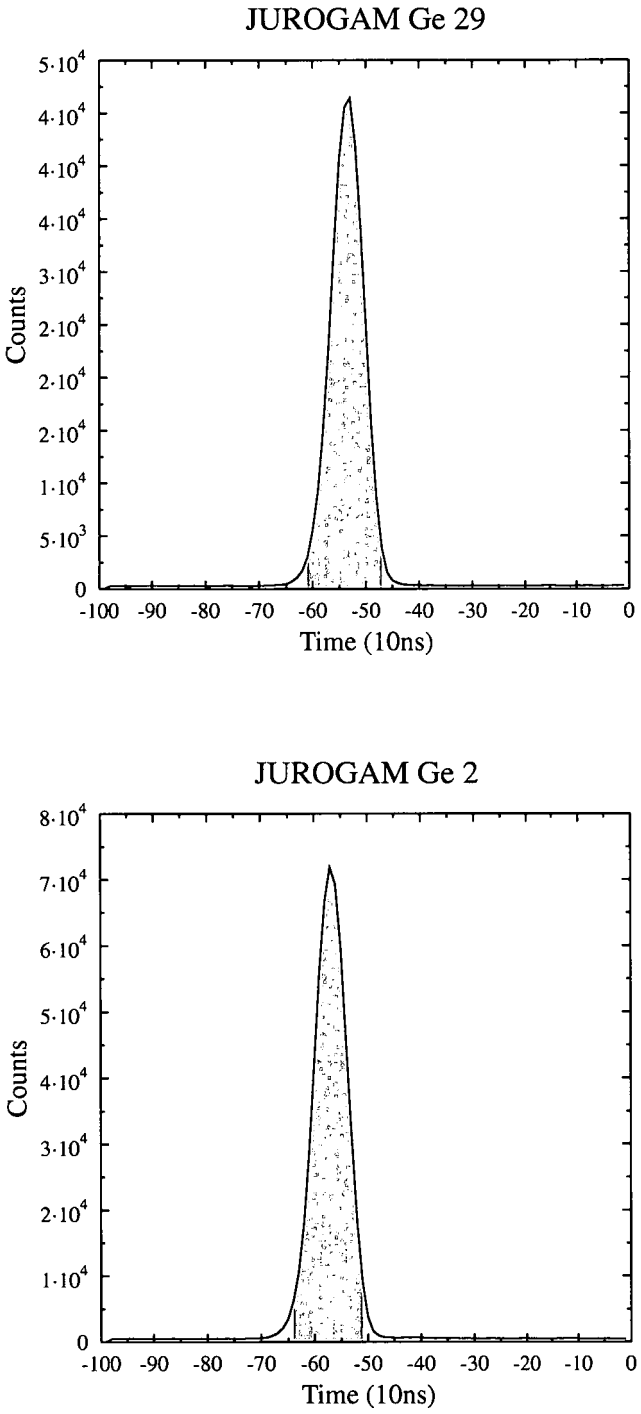

Figure 5.15: Two representative spectra pointing out the fine difference in the time response of the Ge crystals of JUROGAM. The shaded area defines the applied gates of $\sim$ 140 ns.

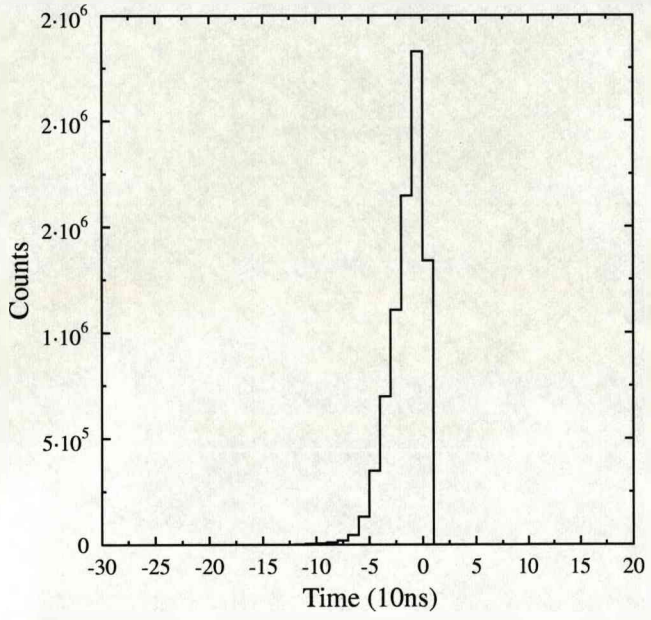

Figure 5.16: Time difference between Ge crystals in $\gamma - \gamma$ coincidence events. An additional time constraint has been applied for further background subtraction to a $\gamma - \gamma$ coincidence of 80 ns.

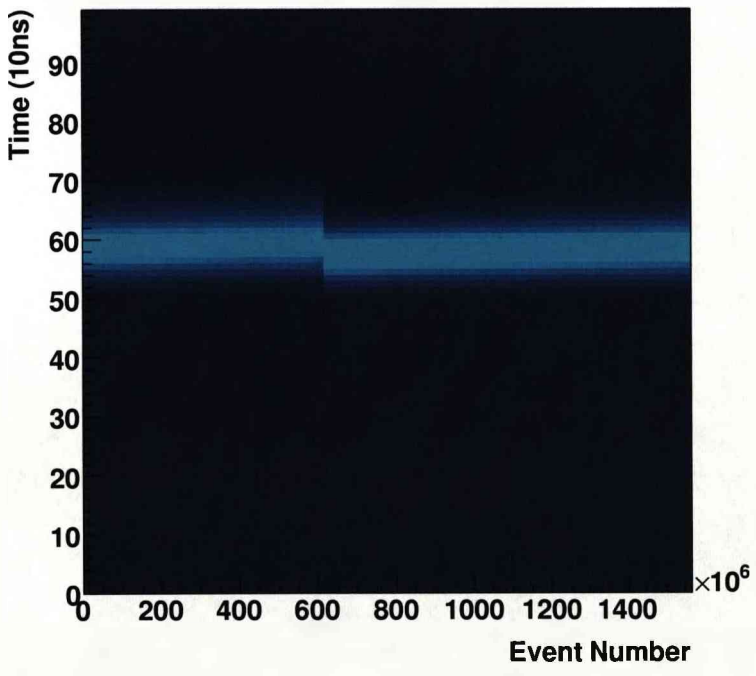

Figure 5.17: Time response of a JUROGAM Ge detector versus the event number. A fine shift downwards is observed corresponding to the refilling of the He gas in RITU. A slight change in the He pressure results in the different time-of-flight through RITU of the order of 20 ns.

5.4 Results

From a total of approximately 1.4×10^5 protons assigned to the ground-state decay of ^{109}I, only 5×10^4 were correlated with a JUROGAM event. Gamma rays from the proton-correlated events are shown in Figs. 5.18(b) and 5.19.

The production cross section for ^{109}I is estimated experimentally to be ~ 10 μb. Theoretically using the ALICE code a cross section of ~ 40 μb was expected, as shown in Fig. 5.20. Although the value of the production cross section of ^{109}I is not precisely reproduced, this calculation gives a good estimate of the strength of this exit channel compared to the other exit channels.

Prompt coincident γ rays correlated with the ^{109}I proton radioactivity were sorted into a symmetric $\gamma - \gamma$ matrix in order to build a level scheme. The level scheme for ^{109}I, deduced from $\gamma - \gamma$ coincidence relationships and $\gamma - \gamma$ coincident intensities [82, 83], is shown in Fig. 5.21, where three band structures are labelled. Gamma rays in coincidence with the strong 594 keV transition (see Figs. 5.18(b) and 5.19) are shown in Fig. 5.22(a), while γ rays in coincidence with the 548 keV and 1056 keV transitions are shown in Figs. 5.22(b) and (c), respectively.

Properties of the γ-ray transitions assigned to ^{109}I are listed in Table 5.1, including several which have not been placed in the level scheme of Fig. 5.21. Excess intensity in the singles over the $\gamma - \gamma$ coincidences of the 538 and 644 keV transitions may suggest that they are doublet transitions. Their nature, however, cannot be ascertained due to limited $\gamma - \gamma$ statistics, i.e. are these transitions self-coincident doublets?

It was possible to produce 1-dimensional proton-correlated γ-ray spectra corresponding to rings of JUROGAM detectors at constant angle θ with respect to the beam axis. Relative intensities of transitions in these spectra allowed discrimination between quadrupole and dipole character. An angular-intensity ratio, R, defined as

$$R = \frac{I_\gamma(\theta = 157.6°, 133.6°)}{I_\gamma(\theta = 94.2°, 85.8°)}$$

has been extracted for the stronger transitions placed in the level scheme of ^{109}I, as listed in Table 5.1. The results have been normalised to $R \equiv 1.0$ for the strong 594 keV transition. Assuming that this transition is of stretched quadrupole ($E2$) character, γ rays of pure stretched dipole character are then predicted [84] to have $R \approx 0.65$, such as the 1056 keV transition linking Band 3 to Band 1. However, values of $R \approx 1.0$ are also expected for pure non-stretched $\Delta I = 0$ ($E1$) transitions; such an assignment is made to the 548 keV transition linking Band 2 to Band 1, in analogy to similar results found for the ^{111}I isotope [85, 86].

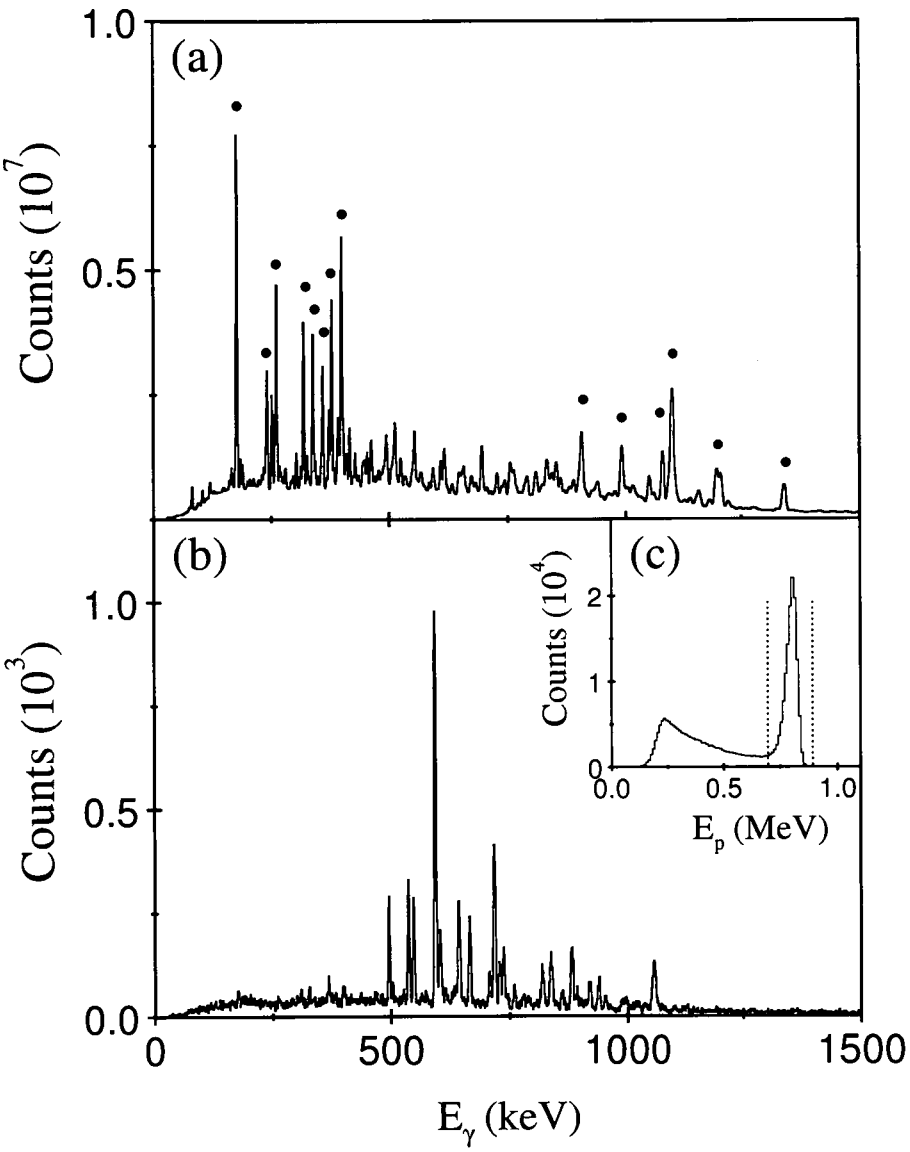

Figure 5.18: (a) Prompt γ-ray spectrum (1 keV/channel) correlated with any recoil detected at the focal plane of RITU. Peaks marked with filled circles are strong transitions in the dominant exit channel, ^{109}Sb. (b) Prompt γ-ray spectrum (1 keV/channel) correlated with the ground-state proton decay of ^{109}I. (c) The decay-energy spectrum recorded by the DSSD for a 300 μs correlation time between a recoil implantation and its subsequent decay. The strong peak in the decay spectrum corresponds to the 813 keV ground-state proton decay of ^{109}I, while the tail on the left consists of escaped protons and β particles. The dotted lines define the energy gate in the time correlated decay spectrum for which the prompt γ rays in JUROGAM have been assigned as transitions in ^{109}I.

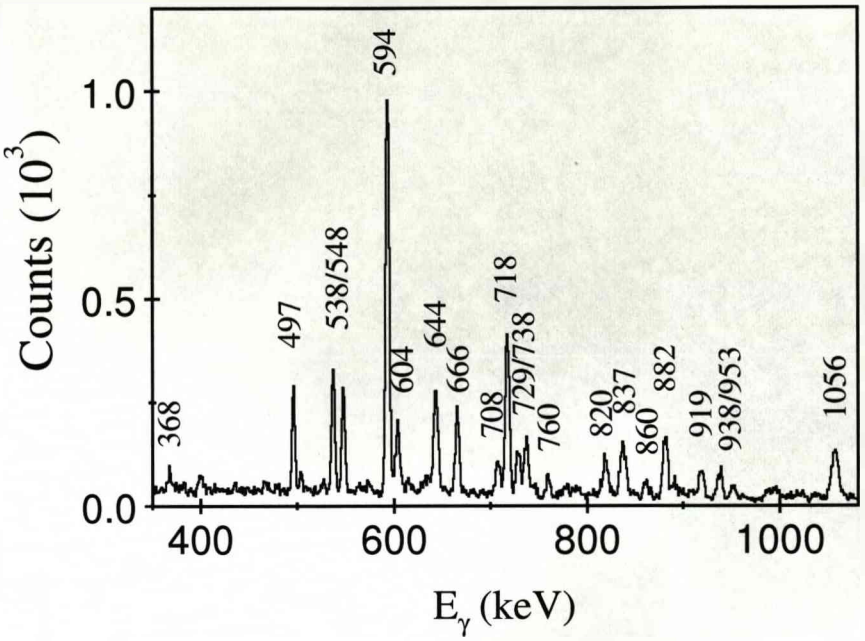

Figure 5.19: Same as Fig. 5.18(b) but with an expanded energy axis and with the assigned ^{109}I transitions labelled by their energies.

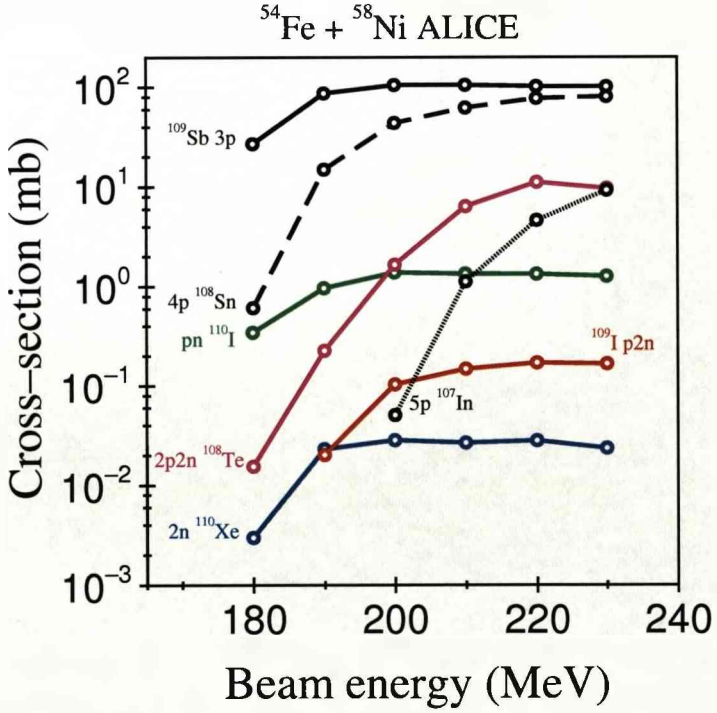

Figure 5.20: Predicted cross sections for residues of the ^{54}Fe + ^{58}Ni fusion-evaporation reaction using the ALICE code [67].

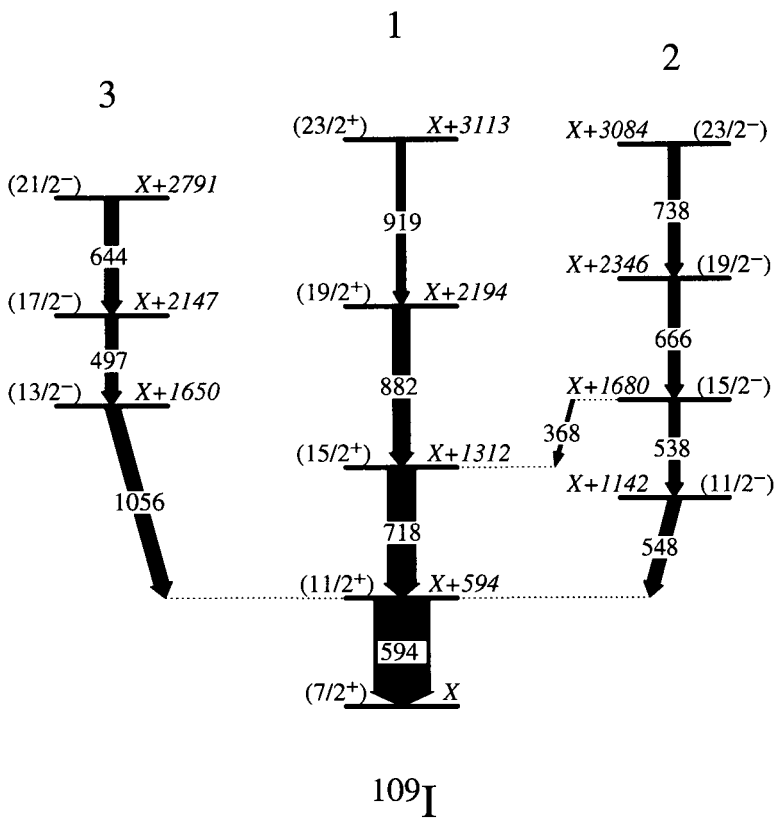

Figure 5.21: Level scheme deduced for ^{109}I. Level and transition energies are labelled in keV, while the widths of the arrows are proportional to the relative $\gamma - \gamma$ coincident transition intensities. The level energies are given relative to the lowest $(7/2^+)$ state, which is probably not the ground state. The tentative spin-parity assignments are discussed in the text.

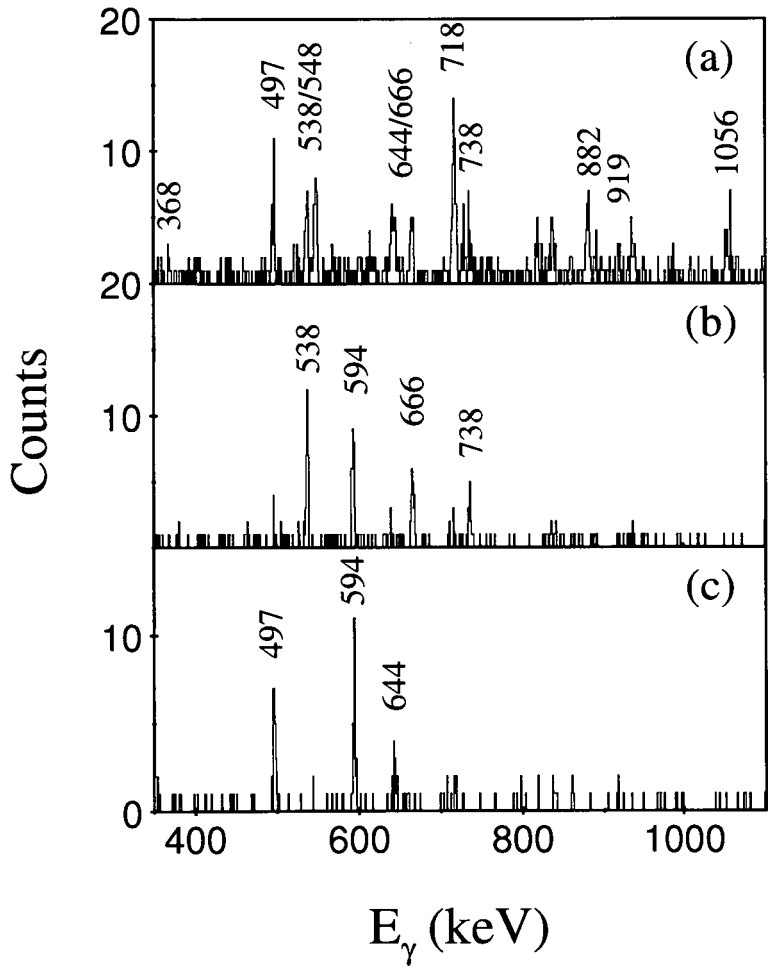

Figure 5.22: Gamma-ray spectra (1 keV/channel) without background subtraction showing transitions in coincidence with (a) the 594 keV transition, (b) the 548 keV transition, and (c) the 1056 keV transition of ^{109}I. The transitions labelled with their energies are shown in the level scheme.

Table 5.1: Properties of γ-ray transitions assigned to ^{109}I. Not all transitions could be placed in the level scheme of Fig. 5.21. The relative intensities and angular-intensity ratio R were extracted from proton-correlated singles spectra. The marked transitions by a star are possible doublets.

E_γ (keV)	I_γ (%)	R	Multipolarity	Assignment	Band
368.1(3)	< 5			$(15/2^- \rightarrow 15/2^+)$	$2 \rightarrow 1$
496.6(2)	20(1)	1.2(2)	$E2$	$(17/2^- \rightarrow 13/2^-)$	3
537.8(2)*	27(1)	1.0(1)	$E2$	$(15/2^- \rightarrow 11/2^-)$	2
548.2(2)	23(1)	1.0(1)	$E1$, $\Delta I = 0$	$(11/2^- \rightarrow 11/2^+)$	$2 \rightarrow 1$
593.9(2)	$\equiv 100(3)$	$\equiv 1.0(1)$	$E2$	$(11/2^+ \rightarrow 7/2^+)$	1
603.8(2)	17(1)				
643.7(2)*	33(2)	1.2(2)	$E2$	$(21/2^- \rightarrow 17/2^-)$	3
666.1(2)	23(1)	1.1(1)	$E2$	$(19/2^- \rightarrow 15/2^-)$	2
708.2(3)	10(1)				
718.1(2)	49(2)	1.1(1)	$E2$	$(15/2^+ \rightarrow 11/2^+)$	1
729.2(3)	13(2)				
737.7(3)	17(1)	1.2(2)	$E2$	$(23/2^- \rightarrow 19/2^-)$	2
760.0(4)	7(1)				
819.5(4)	15(1)				
837.4(3)	23(1)				
860.2(5)	6(1)				
881.7(3)	23(1)	1.2(2)	$E2$	$(19/2^+ \rightarrow 15/2^+)$	1
918.9(4)	10(1)				1
938.4(4)	11(1)				
952.8(5)	6(1)				
1056.4(4)	29(2)	0.7(1)	$E1$	$(13/2^- \rightarrow 11/2^+)$	$3 \rightarrow 1$

5.5 Discussion

In order to interpret the band structures in ^{109}I and justify the present spin/parity assignments, the present level scheme is compared to those of other odd-A iodine isotopes. In addition, cranking calculations are used to strengthen the proposed band structures.

5.5.1 Systematics of Odd-A Iodine Isotopes

Energy systematics of the $\pi h_{11/2}$ bands in odd-A iodine isotopes [6] are shown in Fig. 5.23, including the proposed ^{109}I levels, where it is assumed that Band 2 of Fig. 5.21 represents the corresponding $\pi h_{11/2}$ band. Also shown in the lower part are the relative energies of low-lying $7/2^+$ and $5/2^+$ states. The $5/2^+$ states are derived predominantly from the odd proton occupying the $2\pi d_{5/2}$ orbital and form the ground state of odd-A iodine isotopes with $111 \leq A \leq 127$. However, for $A \geq 129$ the ground state is based on a $7/2^+$ state derived predominantly from the $1\pi g_{7/2}$ orbital. Maximum quadrupole deformation is achieved in the odd-A iodine isotopes for N = 64, 66, namely ^{117,119}I, which lie midway between the N = 50 and N = 82 shell closures. Low-lying $11/2^-$ states, derived from the first $\pi h_{11/2}$ intruder orbital, are found in these isotopes. Moving away from the mid-shell, the relative energy of the $\pi h_{11/2}$ orbital is seen to increase, reflecting a decrease in quadrupole deformation. In addition, the relative energy of the $5/2^+$ ($\pi d_{5/2}$) and $7/2^+$ ($\pi g_{7/2}$) states decreases for isotopes moving away from the mid-shell. Indeed for the heavy odd-A iodine isotopes above ^{127}I ($N \geq 76$), the $7/2^+$ state becomes the ground state. The relative energy of the $5/2^+$ and $7/2^+$ states again decreases as neutrons are removed, and the systematics of Fig. 5.23 suggest that the $5/2^+$ and $7/2^+$ states in ^{109}I must lie very close in energy, and could even be inverted such that the $7/2^+$ state becomes the ground state, analogous to ^{129}I.

It is proposed that Band 1 in ^{109}I is associated with a $\pi g_{7/2}$ orbital weakly coupled to the core (supported by cranking calculations discussed in Section 5.5.2 below), while Band 2 is based on a similar structure involving a $\pi h_{11/2}$ intruder orbital. Indeed, the excitation energy of the bandhead of Band 2 fits well into the systematics (see Fig. 5.23). Moreover, the ratio of the energies of the second and first excited states of Band 2 fits well into the systematics of nuclei in this neutron-deficient region. Such systematics are shown in Fig. 5.24 for the ratio $(E_2 - E_0)/(E_1 - E_0)$ in $_{52}$Te, $_{53}$I, $_{54}$Xe, and $_{55}$Cs isotopes; the data are taken from Ref. [6]. For the even-even isotopes of tellurium and xenon, E_0 corresponds to the energy of the 0^+ ground state ($\equiv 0$), E_1 to the energy of the first excited state (2^+), and E_2 to the second excited state (4^+). For the odd-A iodine and caesium isotopes, the analogous energies E_0, E_1, and E_2 correspond to the energies of the $11/2^-$, $15/2^-$, and $19/2^-$ states, respectively, of bands built on a decoupled $\pi h_{11/2}$ proton orbital. The ratio obtained for the N = 56

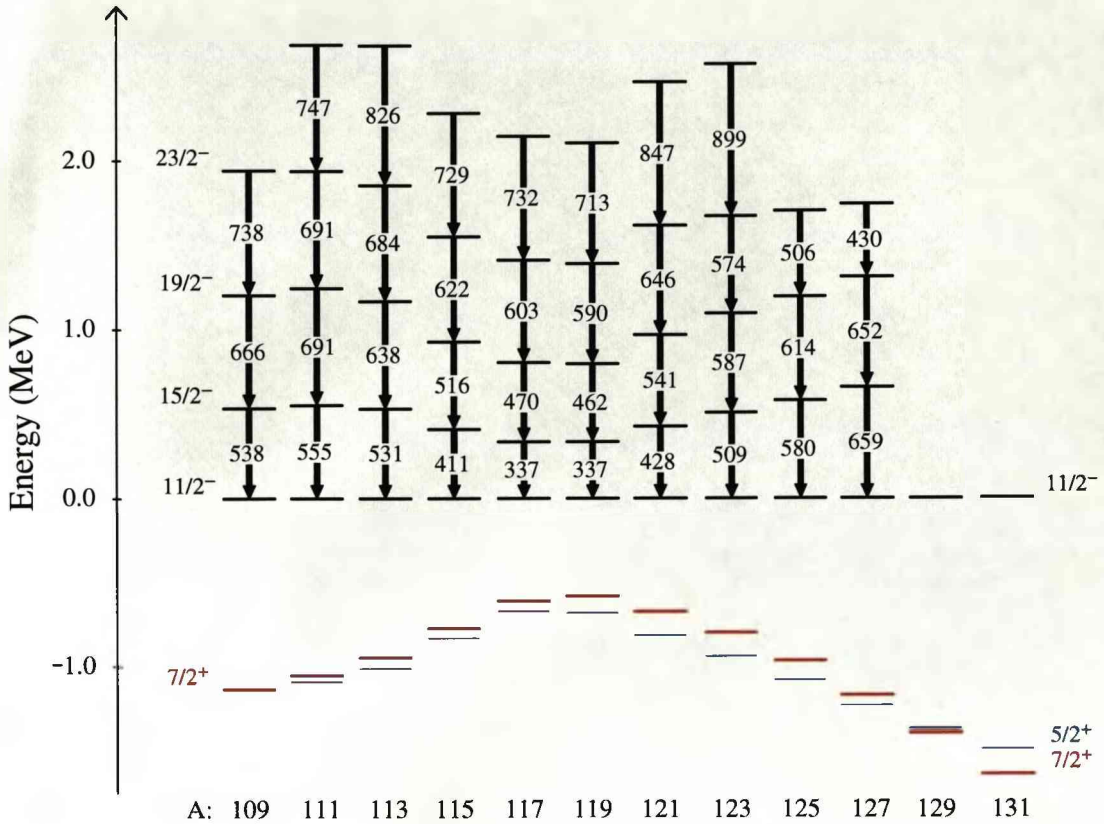

Figure 5.23: Systematics of bands built on the $\pi h_{11/2}$ orbital in odd-A iodine isotopes. The energies of low-lying $5/2^+$ (thin blue line) and $7/2^+$ (thick red line) states relative to the $11/2^-$ states are also shown. The $5/2^+$ state forms the ground state for odd-A iodine isotopes with $111 \leq A \leq 127$, while the $7/2^+$ state becomes the ground state for $A \geq 129$.

Te, I, and Xe isotones is systematically lower than the ratio obtained for the N = 58 isotones.

Another interesting fact is that the $15/2^- \rightarrow 11/2^-$ and $19/2^- \rightarrow 15/2^-$ transitions in ^{109}I are *lower* in energy than the corresponding transitions in ^{111}I (see Fig. 5.23). This may suggest that ^{109}I possesses a larger quadrupole deformation than expected when approaching the N = 50 shell closure. Indeed similar conclusions have been drawn for the ^{110}Xe [7] and ^{112}Xe [87] isotopes.

The lowest state of Fig. 5.21 is assigned $7/2^+$ ($\pi g_{7/2}$). It is not clear whether this represents the ground state of ^{109}I or not, given the expected closeness of $5/2^+$ and $7/2^+$ levels from systematics. The nature of the ground state of ^{109}I can, however, be inferred from the properties of the proton radioactivity, namely the Q-value and mean lifetime of the decay; both are sensitive to the ℓ value (orbital angular momentum) of the decaying state, i.e. is the ground state of ^{109}I based on an $\ell = 2$ ($d_{5/2}$) or $\ell = 4$ ($g_{7/2}$) orbital? Recent theoretical work [88, 89, 90, 91] on (axial) deformed proton emitters supports $\ell = 2$ for the level from which the proton escapes, and hence $5/2^+$

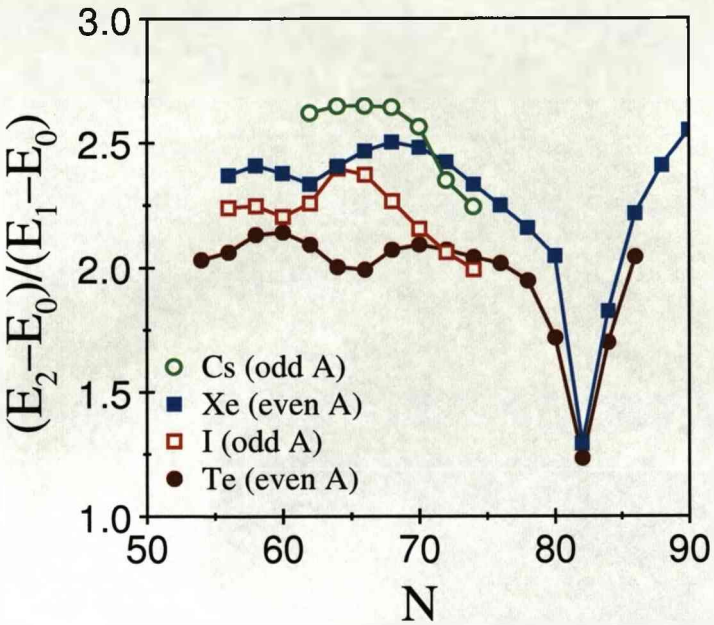

Figure 5.24: Energy-ratio systematics of the first three states in the ground-state bands of even-A Te and Xe isotopes, and the $\pi h_{11/2}$ bands of odd-A I and Cs isotopes.

for the ground state of ^{109}I. It was not possible to observe any γ ray decaying from the $7/2^+$ state of Fig. 5.21 into the presumed $5/2^+$ ground state, which is consistent with the expected closeness of these two levels. Furthermore, no band structure associated with the $5/2^+$ state could be identified due to limited $\gamma - \gamma$ statistics.

5.5.2 Woods-Saxon Cranking Calculations for ^{109}I

Deformation self-consistent cranking calculations based on the total-Routhian surface (TRS) formalism [27, 74, 92], employing a triaxial Woods-Saxon single-particle potential [93, 94], have been performed for various (multi)-quasiparticle configurations in ^{109}I; some results are shown in Fig. 5.25. Single-quasiparticle levels have also been calculated as a function of rotational frequency ω. In all of these calculations, the pairing strength has been calculated at zero frequency and is modelled to decrease with increasing rotational frequency, such that it has fallen by 50% of its initial value at ω = 0.70 MeV/$\hbar$, as detailed in Ref. [27]. The labelling of orbitals adopted in this thesis is shown in Table 5.2.

Average deformations, calculated at a rotational frequency 0.325 MeV/$\hbar$, are listed in Table 5.3 for the lowest 1- and 3-quasiparticle configurations. Moderate quadrupole deformation, $\beta_2 = 0.143 - 0.183$, with some degree of triaxiality $\gamma = 9° - 21°$, is found. It is also evident that the occupation of proton and/or neutron $h_{11/2}$ intruder orbitals tends to increase the quadrupole deformation β_2.

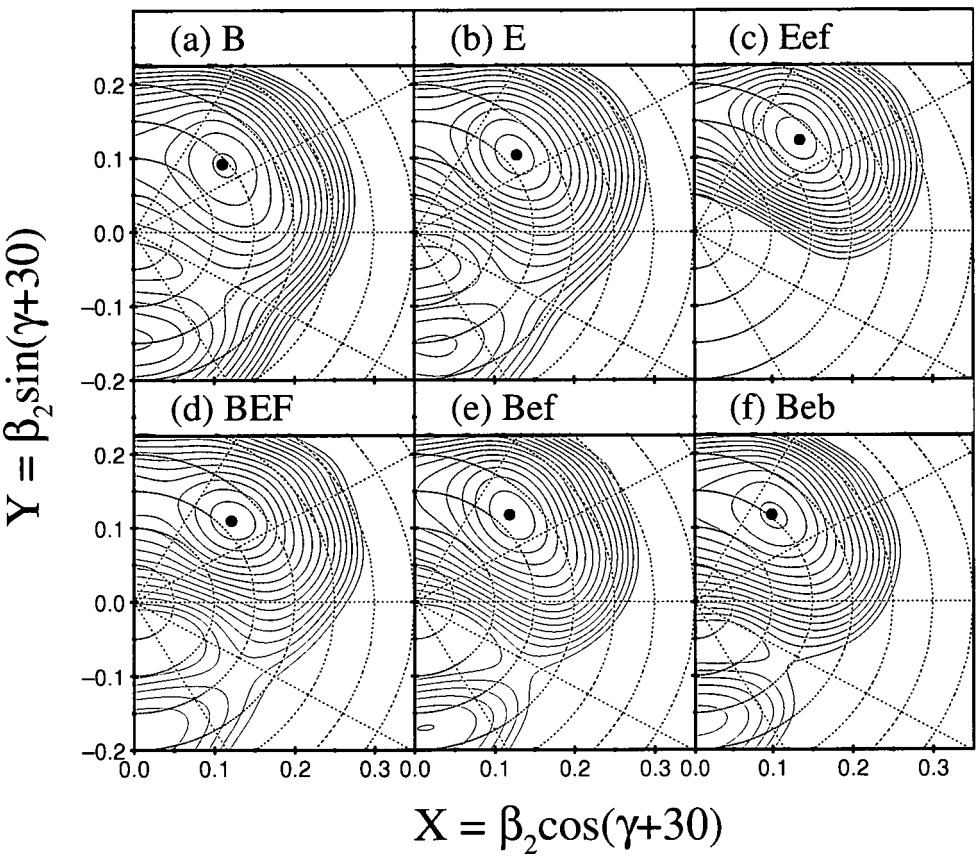

Figure 5.25: TRS surfaces calculated for various 1- and 3-quasiparticle configurations in ^{109}I at a rotational frequency of 0.325 MeV/$\hbar$. The energy contours are separated by 250 keV.

Bands 1 and 2

Single-quasiparticle levels for both protons and neutrons are plotted in Fig. 5.26 as a function of rotational frequency, using the average TRS deformation and pairing parameters appropriate for the B proton configuration (predominantly $\pi g_{7/2}$) of Table 5.3. It can be seen that the B orbital, with signature $\alpha = -1/2$, lies lowest in energy up to $\omega \approx 0.35$ MeV/$\hbar$; hence this orbital is associated with Band 1 of Fig. 5.21. Band 2 is then formed by a quasiparticle excitation from the B orbital into the E ($\pi h_{11/2}$) intruder orbital.

In order to corroborate these assignments, experimental alignments, i_x, and routhians, e', [23] are shown in Fig. 5.27 as a function of rotational frequency. These quantities were extracted using a variable moment-of-inertia reference with Harris parameters [26] $\mathcal{J}_0 = 2.7\ \hbar^2\text{MeV}^{-1}$ and $\mathcal{J}_1 = 70\ \hbar^4\text{MeV}^{-3}$ extracted from Band 1. Clearly ^{109}I is not a good rotor, which is to be expected given the low predicted quadrupole deformation parameters of Table 5.3. Nevertheless, the average experimental alignments of Band 1 ($i_x \sim 2.5\hbar$) and Band 2 ($i_x \sim 5.5\hbar$) are consistent with those expected for the theo-

Table 5.2: Labelling of single-quasiparticle orbitals adopted in this thesis.

	Protons		Neutrons	
(Parity, Signature)	Label	Dominant shell-model state	Label	Dominant shell-model state
(+, +1/2)	A	$g_{7/2}$	a	$g_{7/2}$
(+, −1/2)	B	$g_{7/2}$	b	$g_{7/2}$
(−, −1/2)	E	$h_{11/2}$	e	$h_{11/2}$
(−, +1/2)	F	$h_{11/2}$	f	$h_{11/2}$

Table 5.3: Average TRS deformations calculated for various configurations in ^{109}I.

Configuration	(Parity, Signature)	β_2	β_4	γ
B	(+, −1/2)	0.143	0.040	10°
E	(−, −1/2)	0.165	0.042	9°
Eef	(−, −1/2)	0.183	0.042	12°
BEF	(+, −1/2)	0.162	0.042	12°
Bef	(+, −1/2)	0.165	0.042	15°
Beb	(−, +1/2)	0.154	0.042	20°
Eeb	(+, +1/2)	0.165	0.042	21°

retical B ($\pi g_{7/2}$) and E ($\pi h_{11/2}$) orbitals of Fig. 5.26(a), as shown in Fig. 5.27(a); the theoretical alignment is simply related to the slope of the quasiparticle trajectories, i.e. $i_x = -de'/d\omega$.

It can be seen in Fig. 5.26(a) that two positive-parity proton orbitals are near-degenerate at $\omega = 0$. These orbitals are derived from predominantly $\pi g_{7/2}$ and $\pi d_{5/2}$ states, respectively. The present Woods-Saxon calculations predict that, at zero frequency, these states lie very close in energy, of the order of only a few 10 keV apart. The lower-lying $5/2^+$ state has appreciable $\ell = 2$ components, while the $7/2^+$ state is dominated by $\ell = 4$ components. Slight changes in quadrupole deformation, especially triaxiality, can, however, invert the ordering of the $5/2^+$ and $7/2^+$ states in ^{109}I. Since the characteristics of the proton radioactivity of ^{109}I favour emission from an $\ell = 2$ state, a $5/2^+$ assignment is expected for the ^{109}I ground state. However, this ground state must lie very close to the $7/2^+$ state of Fig. 5.21.

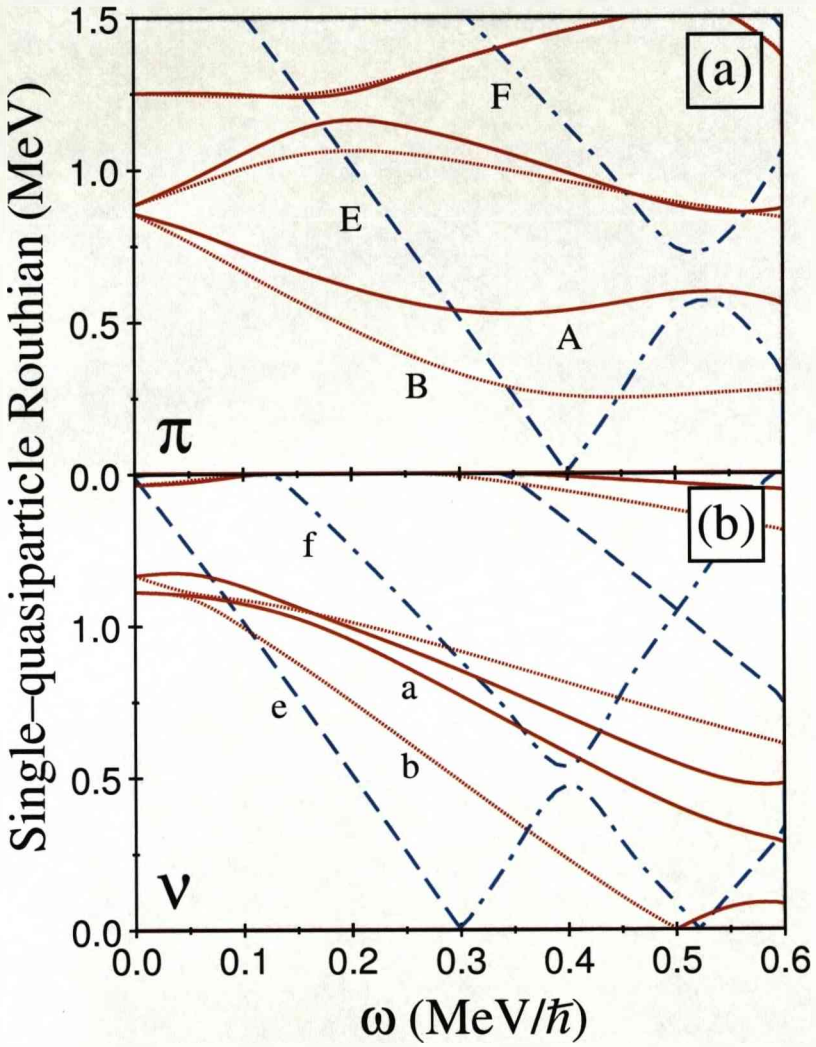

Figure 5.26: Representative single-quasiparticle positive-parity (red) and negative-parity (blue) proton (a) and neutron (b) levels calculated with a cranked Woods-Saxon potential with deformation parameters $\beta_2 = 0.143$, $\beta_4 = 0.040$, $\gamma = 10°$, and pairing parameters $\Delta_\pi = 0.68$ MeV, $\Delta_\nu = 1.10$ MeV. The parity and signature (π, α) of the levels are: (+, +1/2) – solid lines; (+, –1/2) – dotted lines; (–, –1/2) – dashed lines; (–, +1/2) – dot-dashed lines.

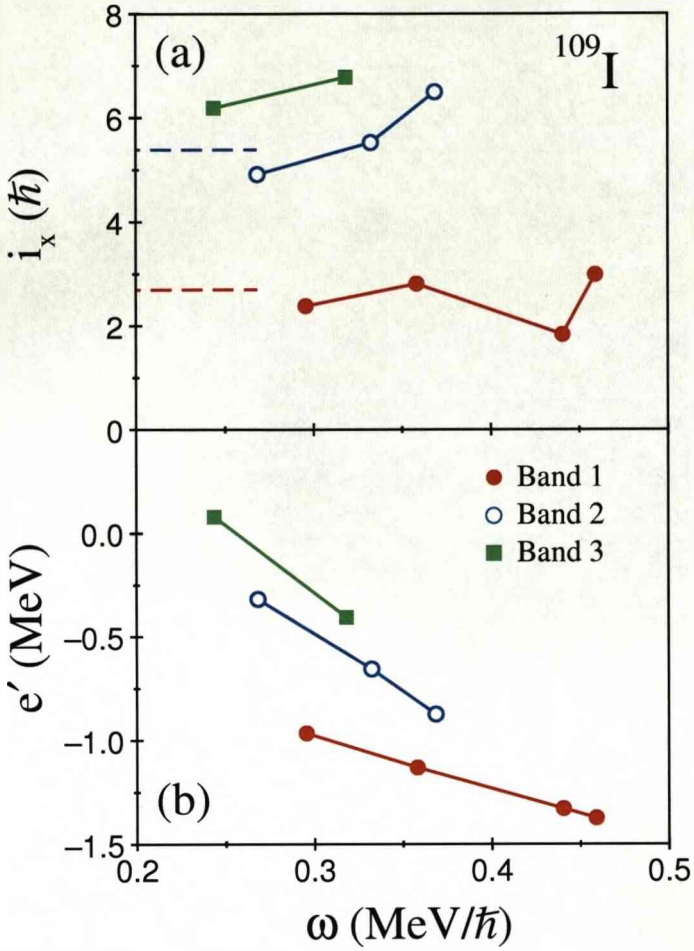

Figure 5.27: Experimental alignments (a) and routhians (b) of the bands in ^{109}I. The dashed lines show the theoretically deduced alignment of Bands 1 and 2 from the slope of their related quasiparticle trajectory.

Band 3

The experimental alignment of Band 3 in Fig. 5.27(a) is seen to be $\sim 1\hbar$ higher than Band 2 and is consequently too high to correspond to a pure single-quasiparticle configuration. The TRS calculations of Fig. 5.25 suggest that 3-quasiparticle configurations become important for frequencies $\omega \approx 0.325$ MeV/$\hbar$. In particular, the Beb configuration, of predominantly $\pi g_{7/2} \otimes \nu(h_{11/2}g_{7/2})$ character, is predicted to be the lowest 3-quasiparticle configuration in energy. Hence this negative-parity structure could be a candidate for Band 3 and indeed has the appropriate $\alpha = +1/2$ signature required for the $I^{\pi}=(13/2^{-})$ bandhead assignment. However, the theoretical alignment of this 3-quasiparticle configuration, obtained from the slopes of the B, e, and b orbitals of Fig. 5.26, is much higher ($i_x \sim 9.5\hbar$) than the experimental value of Fig. 5.27(a)

($i_x \sim 6.5\hbar$). In addition, the experimental routhian (excitation energy in the rotating frame) of Band 3 in Fig. 5.27(b) is too low for a 3-quasiparticle structure. Furthermore, no 3-quasiparticle configurations have been identified in any odd-A iodine isotopes at such low spin and excitation energy.

An alternative interpretation is therefore warranted for Band 3. The core nuclei (even Te isotopes) of the odd-A iodine isotopes are well known to exhibit quadrupole vibrational collectivity [80], i.e. a 2^+ phonon. Furthermore, nuclei of this mass region close to N = Z = 56 exhibit octupole collectivity (3^- phonon). Indeed, octupole collectivity has been discussed in ^{108}Te [95], the core of ^{109}I, in addition to several other light $_{52}$Te and $_{54}$Xe isotopes; see [96] and references therein. Coupling of single-particle states to vibrational phonons, both quadrupole and octupole, has also been discussed in the case of odd-A $_{53}$I isotopes [97]. Octupole collectivity has also been recently discussed in ^{111}I [86].

In the even Te isotopes, the 4_1^+ state occurs at approximately twice the energy of the 2_1^+ state, i.e. these nuclei appear vibrational and the 2_1^+ and 4_1^+ states correspond to one and two quadrupole-vibrational phonons, respectively. The neutron-deficient even Te isotopes also exhibit low-lying negative-parity sidebands that decay to the ground-state bands via strong $E1$ transitions. This has been taken as evidence for octupole collectivity in these nuclei, whereby an octupole-vibrational phonon (3^-) mixes with negative-parity 2-quasiparticle configurations. The pure 1-phonon 3^- state is difficult to observe, especially in the very light even Te isotopes due to the difficulty in producing these exotic nuclei. However, the corresponding 3^- state has recently been identified in ^{114}Xe using the exceptional sensitivity of the EUROBALL spectrometer including the observation of an $E3$ transition decaying directly to the ground state [98]. A 3^- state has also been proposed in ^{112}Xe [87]. Systematics suggest that the 1-phonon 3^- state should exist at an excitation energy $\sim$ 1.6 MeV. In odd-A nuclei, it is possible to couple the odd particle to the collectivity of the core. In regard to octupole collectivity, such features are well established in the heavy Rn-Ra-Th (mass 220) region [99, 100].

An intriguing possibility is that Band 3 in ^{109}I represents a similar coupling of the odd proton, residing in a $\pi g_{7/2}$ orbital, to a collective octupole-vibrational phonon of the ^{108}Te core. With the odd proton in this orbital, both proton and neutron $h_{11/2}$ and $d_{5/2}$ orbitals, with $\Delta j = \Delta \ell = 3$, are available to induce the octupole collectivity. The coupling of a 3^- octupole-vibrational phonon to a $\pi g_{7/2}$ orbital yields spin and parity $I^\pi = 13/2^-$, consistent with the present bandhead assignment of Band 3. The relative excitation energy of Bands 1 and 3 of 1.65 MeV represents the excitation energy of the phonon and this value is consistent with the excitation energy expected from systematics. The octupole-vibrational phonon should generate an alignment of $3\hbar$ [99]. The alignment plot of Fig. 5.27(a) indeed shows that the alignment of Band 3 ($\pi g_{7/2} \otimes 3^-$) is $3 - 4\hbar$ higher than Band 1 ($\pi g_{7/2}$).

5.6 Conclusion

A new level scheme has been constructed for the proton-unbound nucleus ^{109}I following a recoil-decay-tagging experiment using the JUROGAM and GREAT spectrometers. It has been possible to extend relative proton single-particle energies, namely $\pi g_{7/2}$ and $\pi h_{11/2}$ states, to the extremes of isospin close to the N = Z = 50 nucleus ^{100}Sn.

The previously proposed level schemes [8, 9] for ^{109}I and that deduced from the present experiment are illustrated in Fig. 5.28. The γ-ray energies assigned as transitions depopulating ^{109}I from the present experiment (see Table 5.1) are in agreement with the γ-ray transitions deduced in Ref. [9]. However, the level ordering is different and more γ rays have been assigned to this proton-unbound nucleus. Moreover, a more extensive, though still tentative, spin assignment has been attempted in the present experiment.

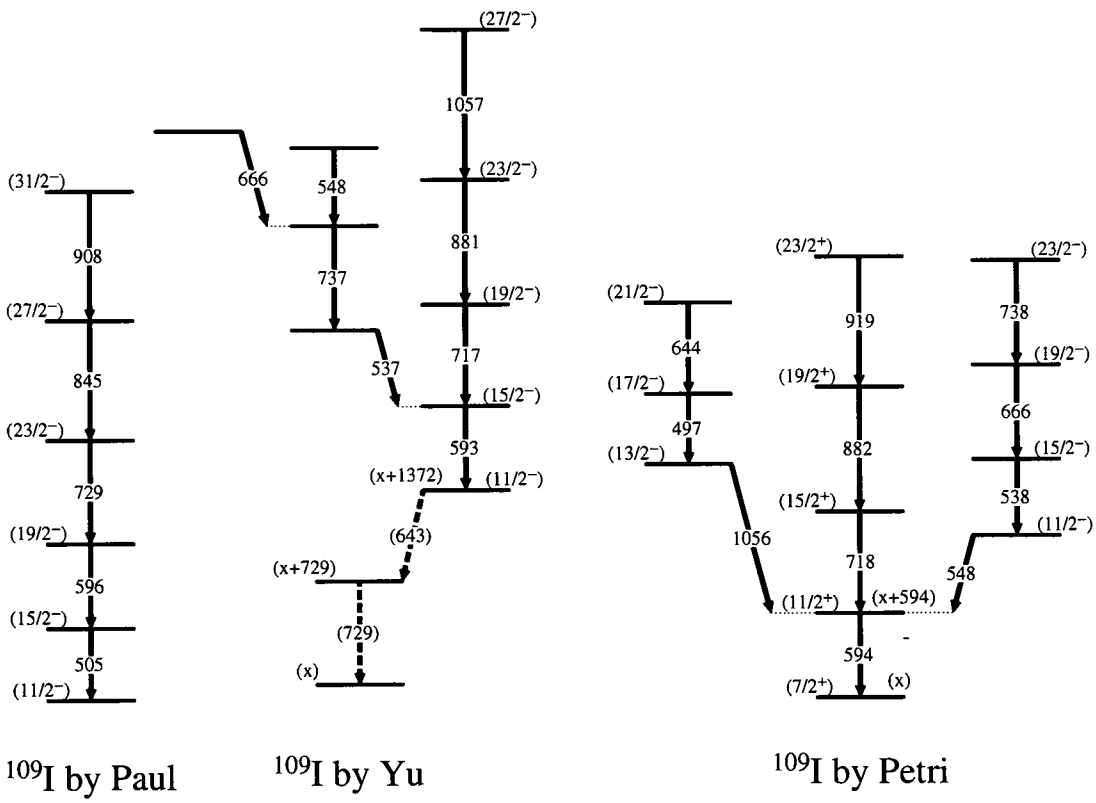

Figure 5.28: The previously proposed level schemes for ^{109}I (by Paul and Yu) and its level scheme deduced from the present experiment (by Petri).

Chapter 6

Conclusions

Results from two fusion-evaporation reaction experiments have been documented in this thesis. The aim of both experiments was the γ-ray spectroscopic investigation of very proton-rich nuclei in the A $\sim$ 130 and A $\sim$ 110 mass regions; however, a completely different approach was used in each region. The A $\sim$ 130 mass region was studied with a radioactive-ion beam, while for the A $\sim$ 110 mass region a stable-ion beam was used.

The radioactive-ion beam experiment had the goal to investigate the A $\sim$ 130 mass region around the drip-line nucleus ^{130}Sm, where large quadrupole ground-state deformations are expected. In order to reach such an exotic region in the nuclear chart, a ^{76}Kr RIB from the SPIRAL facility at GANIL was used to bombard a ^{58}Ni target, while the experimental setup consisted of the EXOGAM γ-ray spectrometer coupled for the first time with both the DIAMANT charged-particle array and the VAMOS spectrometer. High-spin states in the ^{130}Nd (22^+), ^{129}Pr ($27/2^-$), ^{127}Pr ($35/2^-$), ^{128}Nd (16^+), ^{131}Pm ($27/2^-$) and ^{126}Ce (6^+) nuclides have been observed.

The use of RIBs opens a whole new area of exotic nuclei which has not been studied yet. However, the induced background of the beam in combination with its low intensity imposes many experimental challenges. As manifest in this thesis, the EXOGAM γ-ray spectrometer in conjunction with ancillary detectors is a state-of-the-art tool for probing very exotic nuclei that are populated with RIBs. For the ^{76}Kr + ^{58}Ni fusion-evaporation reaction, the strong 4p exit channel, ^{130}Nd, can be studied with the present experimental setup up to relatively high spin. According to Table 4.8 of Section 4.3.6, it is expected that spectroscopy down to a level of 4 mb can be performed, given that there is a valid trigger to select the fusion-evaporation events, i.e. a charged-particle detector such as DIAMANT to select the evaporated particles, and by improving the γ-ray spectrum with techniques such as the "segment-hit pattern", as described in Section 4.3.4.

Further development of RIBs, namely higher intensity and bigger variety of species, will allow completely unknown mass regions to be reached, where the strong exit channels could lead to the discovery and study of completely unknown nuclei. The SPIRAL

II [101] project at GANIL, currently under development, aims at delivering very exotic beams at much higher intensities. Moreover, the advances in γ-ray spectrometers can provide a breakthrough in γ-ray spectroscopic studies, as weaker channels with low cross sections will be observed due to the higher photopeak efficiency of the array. The forthcoming AGATA γ-ray spectrometer [102] constitutes such a powerful array, which in combination with the SPIRAL II project can revolutionise nuclear structure investigations at GANIL.

The stable-ion beam experiment involved recoil-decay-tagging γ-ray spectroscopy of the light ^{110}Xe and ^{109}I nuclides using the ^{54}Fe + ^{58}Ni fusion-evaporation reaction. The experimental setup consisted of the JUROGAM array in conjunction with the RITU spectrometer and the GREAT focal plane at JYFL, Finland. This thesis has focused on the results from ^{109}I, which in the past yielded conflicting level schemes from two previous experiments. Gamma rays depopulating excited states in ^{109}I have been identified and a new level scheme has been constructed. The three band structures observed in ^{109}I have been interpreted in the framework of the Cranked Shell Model as being built on $\pi g_{7/2}$ and $\pi h_{11/2}$ states in a weakly deformed, triaxial nucleus, as well as on a $\pi g_{7/2}$ orbital coupled to an octupole-vibrational phonon of the ^{108}Te core.

Systematic investigations of nuclei approaching the doubly-magic ^{100}Sn nuclide are of great importance. Their production cross section, however, drops dramatically as one approaches the proton drip line. The highly selective recoil-decay-tagging technique is proved to be an excellent tool for probing such weakly populated nuclides, i.e. ^{106}Te [80], with a 25 nb production cross section via the ^{54}Fe + ^{54}Fe fusion-evaporation reaction, has been studied successfully at JYFL in the past. The limits of this technique, however, necessitates the advent of new methods to investigate ever more exotic nuclei. The answer to this quest comes with the use of more selective devices of higher efficiency and/or with the use of RIBs.

Publications

The material of this thesis resulted in the preparation and submission of the following papers:

1. **Probing the Maximally Deformed Light Rare-Earth Region Around the Drip-Line Nucleus ^{130}Sm**
   M. Petri, E. S. Paul, P. J. Nolan, A. J. Boston, R. J. Cooper, M. R. Dimmock, S. Gros, B. M. McGuirk, H. C. Scraggs, G. Turk, B. Rossé, M. Meyer, N. Redon, Ch. Schmitt, O. Stézowski, D. Guinet, Ph. Lautesse, G. De France, S. Bhattachasyya, G. Mukherjee, F. Rejmund, M. Rejmund, H. Savajols, J. N. Scheurer, A. Astier, I. Deloncle, A. Prévost, B. M. Nyakó, J. Gál, J. Molnár, J. Timár, L. Zolnai, K. Juhász, V. F. E. Pucknell, R. Wadsworth, P. Joshi, G. La Rana, R. Moro, M. Trotta, E. Vardaci, G. Hackman and G. Ball
   Physica Scripta **T125**, 214 (2006)

2. **The use of EXOGAM for In-Beam Spectroscopy of Proton Drip-Line Nuclei using Radioactive Ion Beams**
   M. Petri *et al.*
   In preparation

3. **Nuclear levels in proton-unbound ^{109}I: Relative single-particle energies beyond the proton drip line**
   M. Petri, E. S. Paul, B. Cederwall, I. G. Darby, M. R. Dimmock, S. Eeckhaudt, E. Ganioğlu, T. Grahn, P. T. Greenlees, B. Hadinia, P. Jones, D. T. Joss, R. Julin, S. Juutinen, S. Ketelhut, A. Khaplanov, M. Leino, L. Nelson, M. Nyman, R. D. Page, P. Rahkila, M. Sandzelius, J. Sarén, C. Scholey, J. Sorri, J. Uusitalo, and R. Wadsworth
   Physical Review C **76**, 054301 (2007)

The first paper is a peer-reviewed conference proceeding, while the second paper is in preparation; both papers are relevant to the work described in Chapter 4. The Regular Article in Physical Review C presents the work carried out for ^{109}I of Chapter 5.

Bibliography

[1] Stoitsov, M. V., Dobaczewski, J., Nazarewicz, W., Pittel, S., and Dean, D. J. Systematic study of deformed nuclei at the drip lines and beyond. *Phys. Rev. C* **68**, 054312 (2003).

[2] Möller, P., Nix, J. R., Myers, W. D., and Swiatecki, W. J. Nuclear ground-state masses and deformations. *At. Data Nucl. Data Tables* **59**, 185 (1995).

[3] Grodzins, L. The uniform behaviour of electric quadrupole transition probabilities from first 2^+ states in even-even nuclei. *Phys. Lett.* **2**, 88 (1962).

[4] Stephens, F. S., Diamond, R. M., Leigh, J. R., Kammuri, T., and Nakai, K. Decoupled yrast states in odd-mass nuclei. *Phys. Rev. Lett.* **29**, 438 (1972).

[5] Sonzongi, A. A. *et al.* Fine structure in the decay of the highly deformed proton emitter ^{131}Eu. *Phys. Rev. Lett.* **83**, 1116 (1999).

[6] http://www.nndc.bnl.gov/ensdf. Brookhaven national nuclear data cente.

[7] Sandzelius, M. *et al.* Identification of excited states in the $T_z = 1$ nucleus ^{110}Xe: Evidence for enhanced collectivity near the N = Z = 50 double shell closure. *Phys. Rev. Lett.* **99**, 022501 (2007).

[8] Paul, E. S. *et al.* In-beam γ-ray spectroscopy above ^{100}Sn using the new technique of recoil decay tagging. *Phys. Rev. C* **51**, 78 (1995).

[9] Yu, C.-H. *et al.* Spectroscopy of the proton emitter ^{109}I. *Phys. Rev. C* **59**, R1834 (1999).

[10] Bohr, N. and Wheeler, J. A. The mechanism of nuclear fission. *Phys. Rev.* **56**, 426 (1939).

[11] Ring, P. and Schuck, P. *The Nuclear Many-Body Problem.* Springer, (2004).

[12] Brown, B. A. *Lecture Notes in Nuclear Structure Physics.* November (2005).

[13] Mayer, M. G. On closed shells in nuclei. II. *Phys. Rev.* **75**, 1969 (1949).

[14] Haxel, O., Jensen, J. H. D., and Suess, H. E. On the "magic numbers" in nuclear structure. *Phys. Rev.* **75**, 1766 (1949).

[15] Rose, M. E. *Elementary Theory of Angular Momentum.* John Wiley and Sons, (1966).

[16] Andersson, G. *et al.* Nuclear shell structure at very high angular momentum. *Nucl. Phys. A* **268**, 205 (1976).

[17] Nilsson, S. G. Binding states of individual nucleons in strongly deformed nuclei. *Mat. Fys. Medd. Dan. Vid. Selsk.* **29**, 10 (1955).

[18] Nilsson, S. G. *et al.* On the nuclear structure and stability of heavy and superheavy elements. *Nucl. Phys. A* **131**, 1 (1969).

[19] Nilsson, D. G. and Ragnarsson, I. *Shapes and Shells in Nuclear Structure.* Cambridge University Press, (1995).

[20] Bohr, A. and Mottelson, B. R. *Nuclear Structure*, volume 2. World Scientific Publishing, (1998).

[21] Zhang, J.-Y., Xu, N., Fossan, D. B., Liang, Y., Ma, R., and Paul, E. S. Nilsson parameter set in the A $\approx 120 - 140$ region. *Phys. Rev. C* **39**, 714 (1989).

[22] Inglis, D. R. Particle derivation of nuclear rotation properties associated with a surface wave. *Phys. Rev.* **96**, 1059 (1954).

[23] Bengtsson, R. and Frauendorf, S. Quasiparticle spectra near the yrast line. *Nucl. Phys. A* **327**, 139 (1979).

[24] Afanasjev, A. V., Fossan, D. B., Lane, G. J., and Ragnarsson, I. Termination of rotational bands: Disappearance of quantum many-body collectivity. *Phys. Rep.* **322**, 1 (1999).

[25] de Voigt, M. J. A., Dudek, J., and Szymański, Z. High-spin phenomena in atomic nuclei. *Rev. Mod. Phys.* **55**, 949 (1983).

[26] Harris, S. M. Higher order corrections to the Cranking Model. *Phys. Rev.* **138**, B509 (1965).

[27] Wyss, R., Nyberg, J., Johnson, A., Bengtsson, R., and Nazarewicz, W. Highly deformed intruder bands in the A $\simeq$ 130 mass region. *Phys. Lett. B* **215**, 211 (1988).

[28] Strutisnky, V. M. Shell effects in nuclear masses and deformation energies. *Nucl. Phys. A* **95**, 420 (1967).

[29] Strutisnky, V. M. "Shells" in deformed nuclei. *Nucl. Phys. A* **122**, 1 (1968).

[30] Krane, K. S. *Introductory Nuclear Physics.* John Wiley and Sons, (1987).

[31] http://www.ganil.fr.

[32] http://www.ganil.fr/spiral.

[33] Villari, A. C. C. The accelerated ISOL technique and the SPIRAL project. *Nucl. Phys. A* **693**, 465 (2001).

[34] http://www.ganil.fr/spiral/cime.html.

[35] http://www.ganil.fr/spiral/graphs.html.

[36] http://www.ganil.fr/user/areas/index.html.

[37] Bass, R. *Nuclear Reactions with Heavy Ions.* Springer-Verlag, (1980).

[38] Leo, W. R. *Techniques for Nuclear and Particle Physics Experiments.* Springer-Verlag, 2nd edition, (1994).

[39] Knoll, G. F. *Radiation Detection and Measurement.* John Wiley & Sons, Inc., 3rd edition, (2000).

[40] Ghiorso, A. *et al.* Sassy, a gas-filled magnetic separator for the study of fusion reaction products. *Nucl. Instrum. Methods Phys. Res. A* **269**, 192 (1988).

[41] Bohr, N. Velocity-range relation for fission fragments. *Phys. Rev.* **59**, 270 (1941).

[42] Beck, F. A. EUROBALL: Large gamma ray spectrometers through European collaborations. *Prog. Part. Nucl. Phys.* **28**, 443 (1992).

[43] Duchêne, G. *et al.* The Clover: a new generation of composite Ge detectors. *Nucl. Instrum. Methods Phys. Res. A* **432**, 90 (1999).

[44] Shepherd, S. L. *et al.* Measurements on a prototype segmented Clover detector. *Nucl. Instrum. Methods Phys. Res. A* **434**, 373 (1999).

[45] Azaiez, F. EXOGAM: a γ-ray spectrometer for radioactive beams. *Nucl. Phys. A* **654**, 1003c (1999).

[46] Simpson, J. *et al.* The EXOGAM array: A radioactive beam gamma-ray spectrometer. *Heavy Ion Phys.* **11**, 159 (2000).

[47] Gros, S. A. A. *Characterisation of an EXOGAM Clover germanium detector.* PhD thesis, University of Liverpool, (2005).

[48] http://nnsa.dl.ac.uk/MIDAS.

[49] Gál, J. *et al.* The VXI electronics of the DIAMANT particle detector array. *Nucl. Instrum. Methods Phys. Res. A* **516**, 502 (2004).

[50] Savajols, H. VAMOS: A variable mode high acceptance spectrometer for identifying reaction products induced by SPIRAL beams. *Nucl. Instrum. Methods Phys. Res. B* **204**, 146 (2003).

[51] Rossi Alvarez, C. The GASP array. *Nucl. Phys. News* **3**, 3 (1993).

[52] Simpson, J. The Euroball spectrometer. *Z. Phys. A* **358**, 139 (1997).

[53] Nolan, P. J., Beck, F. A., and Fossan, D. B. Large arrays of escape-suppressed gamma-ray detectors. *Annu. Rev. Nucl. Part. Sci.* **44**, 561 (1994).

[54] Pakarinen, J. *Probing non-yrast structures of* ^{186}Pb *in a RDT measurement employing the JUROGAM array.* PhD thesis, University of Jyväskylä, (2005).

[55] Leino, M. *et al.* Gas-filled recoil separator for studies of heavy elements. *Nucl. Instrum. Methods Phys. Res. B* **99**, 653 (1995).

[56] Leino, M. In-flight separation with gas-filled systems. *Nucl. Instrum. Methods Phys. Res. B* **126**, 320 (1997).

[57] http://www.jyu.fi/science/laitokset/fysiikka/en/research/accelerator/nucspec/ritu/RITU.

[58] Cormier, T. M., Stwertka, P. M., Herman, M., and Nicolis, N. G. Internal conversion and the evolution of nuclear structure at very high spin: $^{154-158}$Er. *Phys. Rev. C* **30**, 1953 (1984).

[59] Page, R. D. The GREAT spectrometer. *Nucl. Instrum. Methods Phys. Res. B* **204**, 634 (2003).

[60] Andreyev, A. N. *et al.* GEANT monte carlo simulations for the GREAT spectrometer. *Nucl. Instrum. Methods Phys. Res. A* **533**, 422 (2004).

[61] Lazarus, I. H. *et al.* The GREAT triggerless Total Data Readout method. *IEEE Transaction on Nuclear Science* **48**, 3 (2001).

[62] Rahkila, P. Grain - a Java analysis framework for Total Data Readout. *Nucl. Instrum. Methods Phys. Res. A* . in press.

[63] Girod, M. private communication, Bruyère-le-Châtel, CEA/DAM.

[64] http://www.ganil.fr/exogam.

[65] Singh, B. Nuclear data sheets update for A = 76. *Nucl. Data Sheets* **74**, 63 (1995).

[66] http://nnsa.dl.ac.uk/documents/edoc421/edoc421.pdf.

[67] Blann, M. Report OVERLAID ALICE COO 3494-29, (1977). Unpublished.

[68] Hartley, D. J. *et al.* Yrast spectroscopy of ^{130}Nd and evidence of a highly deformed band. *Phys. Rev. C* **63**, 024316 (2001).

[69] Zeidan, O. *et al.* Yrast spectroscopy of $^{128}_{60}Nd_{68}$ and systematics of the $\nu h_{11/2}$ crossing in A $\sim$ 130 nuclei. *Phys. Rev. C* **66**, 044311 (2001).

[70] Petrache, C. M. *et al.* Spectroscopy of the deformed ^{126}Ce nucleus. *Eur. Phys. J. A* **16**, 337 (2003).

[71] http://www.triumf.ca.

[72] http://www.triumf.ca/isac/isac_home.html.

[73] Skalski, J. Octupolly deformed nuclei near ^{112}Ba. *Phys. Lett. B* **238**, 6 (1990).

[74] Nazarewicz, W., Leander, G. A., and Dudek, J. Octupole shapes and shape changes at high spins in Ra and Th nuclei. *Nucl. Phys. A* **467**, 437 (1987).

[75] Davids, C. N. *et al.* Proton radioactivity - spherical and deformed. *Act. Phys. Pol. B* **30**, 555 (1999).

[76] Faestermann, T., Gillitzer, A., Hartel, K., Kienle, P., and Nolte, E. Evidence for proton radioactivity of ^{113}Cs and ^{109}I. *Phys. Lett. B* **137**, 23 (1984).

[77] Sellin, P. J. *et al.* Proton spectroscopy beyond the drip line near A = 150. *Phys. Rev. C* **47**, 1933 (1993).

[78] Simon, R. S. *et al.* Evidence for nuclear shape coexistence in ^{180}Hg. *Z. Phys. A* **325**, 197 (1986).

[79] http://www.jyu.fi/science/laitokset/fysiikka/en/research/accelerator/nucspec/gamma/jurogam/photos/drawings.

[80] Hadinia, B. *et al.* First identification of excited states in ^{106}Te and evidence for isoscalar-enhanced vibrational collectivity. *Phys. Rev. C* **72**, 041303(R) (2005).

[81] Hadinia, B. *et al.* First identification of γ-ray transitions in ^{107}Te. *Phys. Rev. C* **70**, 064314 (2004).

[82] Radford, D. C. ESCL8R and LEVIT8R: Software for interactive graphical analysis of HPGe coincidence data sets. *Nucl. Instrum. Methods Phys. Res. A* **361**, 297 (1995).

[83] Radford, D. C. Background subtraction from in-beam HPGe coincidence data sets. *Nucl. Instrum. Methods Phys. Res. A* **361**, 306 (1995).

[84] Yamazaki, T. Tables of coefficients for angular distribution of gamma rays from aligned nuclei. *Nucl. Data Sheets Section A* **3**, 1 (1967).

[85] Paul, E. S. *et al.* High-spin study of ^{111}I. *Phys. Rev. C* **61**, 064320 (2000).

[86] Spolaore, P. *et al.* Identification and study of the very neutron deficient nuclide ^{111}I: search for octupole correlations in the region of N $\simeq$ Z $\simeq$ 56. *Nucl. Phys. A* **682**, 387c (2001).

[87] Smith, J. F. *et al.* Excited states and deformation of ^{112}Xe. *Phys. Lett. B* **523**, 13 (2001).

[88] Maglione, E., Ferreira, L. S., and Liotta, R. J. Nucleon decay from deformed nuclei. *Phys. Rev. Lett.* **81**, 538 (1998).

[89] Maglione, E., Ferreira, L. S., and Liotta, R. J. Proton emission from deformed nuclei. *Phys. Rev. C* **59**, R589 (1999).

[90] Delion, D. S., Liotta, R. J., and Wyss, R. Systematics of proton emission. *Phys. Rev. Lett.* **96**, 072501 (2006).

[91] Delion, D. S., Liotta, R. J., and Wyss, R. Theories of proton emission. *Phys. Rep.* **424**, 113 (2006).

[92] Nazarewicz, W., Wyss, R., and Johnson, A. Structure of superdeformed bands in the A $\approx$ 150 mass region. *Nucl. Phys. A* **503**, 285 (1989).

[93] Nazarewicz, W., Dudek, J., Bengtsson, R., Bengtsson, T., and Ragnarsson, I. Microscopic study of the high-spin behaviour in selected A $\simeq$ 80 nuclei. *Nucl. Phys. A* **435**, 397 (1985).

[94] Cwiok, S., Dudek, J., Nazarewicz, W., Skalski, J., and Werner, T. Single-particle energies, wave functions, quadrupole moments and g-factors in an axially deformed Woods-Saxon potential with applications to the two-centre-type nuclear problems. *Comp. Phys. Comm.* **46**, 379 (1987).

[95] Lane, G. J. *et al.* Octupole correlations at low spin in $^{108}_{52}\mathrm{Te}_{56}$. *Phys. Rev. C* **57**, R1022 (1998).

[96] Paul, E. S. *et al.* γ-ray spectroscopy of neutron-deficient ^{110}Te. II. high-spin smooth-terminating structures. *Phys. Rev. C* **76**, 034323 (2007).

[97] Jackson, S. V., Walters, W. B., and Meyer, R. A. Radioactive decay of 30-h $^{131}\mathrm{Te}^m$ and 25-min $^{131}\mathrm{Te}^g$ to levels of ^{131}I. *Phys. Rev. C* **11**, 1323 (1975).

[98] de Angelis, G. *et al.* Coherent proton - neutron contribution to octupole correlations in the neutron-deficient ^{114}Xe nucleus. *Phys. Lett. B* **535**, 93 (2002).

[99] Cocks, J. F. C. *et al.* Observation of octupole structures in radon and radium isotopes and their contrasting behavior at high spin. *Phys. Rev. Lett.* **78**, 2920 (1997).

[100] Cocks, J. F. C. *et al.* Spectroscopy of Rn, Ra and Th isotopes using multi-nucleon transfer reactions. *Nucl. Phys. A* **645**, 61 (1999).

[101] http://www.ganil.fr/research/developments/spiral2.

[102] http://www-win.gsi.de/agata.